UC Davis
UC Davis Electronic Theses and Dissertations

Title

Coupling Effect in Doppler Radar System Used for Remote Sensing

Permalink

https://escholarship.org/uc/item/6tx89435

Author

Jiang, Xiaonan

Publication Date

2022

Peer reviewed|Thesis/dissertation

eScholarship.org Powered by the California Digital Library
University of California

Coupling Effect in Doppler Radar System Used for Remote Sensing

By

XIAONAN JIANG
DISSERTATION

Submitted in partial satisfaction of the requirements for the degree of

DOCTOR OF PHILOSOPHY

in

Electrical and Computer Engineering

in the

OFFICE OF GRADUATE STUDIES

of the

UNIVERSITY OF CALIFORNIA

DAVIS

Approved:

Q. Jane Gu, Chair

J. Sebastian Gomez-Diaz

Xiaoguang Liu

Committee in Charge

2022

To my beloved family

whose encouragement and support have made this possible

Contents

List of Figures vii

List of Tables xiii

Abstract xiv

Acknowledgments xvi

1 Introduction **1**

1.1 Overview of Doppler Radar System Architectures for Vital Sign Detection 3

1.1.1 FOM Metrics Design for Detection Sensitivity Comparison 7

1.1.2 System Performance Trend 10

1.1.3 Spatial Resolution Review 13

1.2 Overview of Remote Displacement Sensing Using Doppler Radar 14

1.3 Overview of Coupling Effect in Doppler Radar System 15

1.4 Summary of Dissertation 17

2 IF System Development for Improved System Compactness and Spatial Resolution **21**

2.1 Introduction 21

2.2 Architecture of Digital Low-IF Dual-PLL Doppler Radar System 22

2.3 Validation of Phase Coherence 24

2.4 Single-Channel Prototype System Development 25

2.5 MIMO System Development 28

2.5.1 Compact Dual-PLL Module Design 28

2.5.2 6x6 MIMO System Design 29

2.5.3 System Calibration 30

2.5.4 Experiments 31

2.6 Summary 35

3 Coupling Effect to SNR in Dual-PLL IF System **40**

3.1 Introduction 40

3.2 Noise Analysis . . . 41
  3.2.1 Amplitude Noise . . . 41
  3.2.2 Residual Phase Noise . . . 42
  3.2.3 Interference from TX-RX Leakage . . . 45
  3.2.4 A Numerical Example . . . 48
  3.2.5 System SNR Analysis Method Comparison . . . 53
3.3 Phase Noise Validation . . . 54
3.4 Measurements using Test Bench Setup . . . 56
  3.4.1 Coupling/Leakage Effect . . . 56
  3.4.2 System Gain Effect . . . 59
  3.4.3 Antenna Parameters on System SNR . . . 61
  3.4.4 RF Cancellation Effect . . . 62
3.5 RF Cancellation on Improving Vital Sign Detection . . . 64
3.6 Summary . . . 65

4 Automatic Coupling Cancellation Development for IF System 66
4.1 Hardware Implementation . . . 66
4.2 Automatic RF Cancellation Algorithm . . . 67
  4.2.1 Accommodation for Wide-range Scenarios . . . 68
  4.2.2 Trade-off Due to Components Parasitic . . . 68
  4.2.3 Optimum RF Cancellation Algorithm . . . 69
  4.2.4 Comparison Between RF Cancellation Algorithms . . . 70
4.3 Low TX Power Vital Sign Detection . . . 72
  4.3.1 Experiment Setup . . . 72
  4.3.2 Result Analysis . . . 73
4.4 Through Wall Vital Sign Detection . . . 75
  4.4.1 Test-bench Setup Measurement . . . 76
  4.4.2 Through-Wall Vital Sign Detection Using RF Cancellation . . . 77
4.5 Summary . . . 79

5 Coupling Effect to AM and PM inside Doppler Radar System 80
5.1 Introduction 80
5.2 Modulation Analysis in Doppler Radar System 80
    5.2.1 Analysis without Coupling Effect 81
    5.2.2 Coupling Signal Representation 82
    5.2.3 Amplitude Modulation with Coupling 83
    5.2.4 Interpretation of AM and PM in IQ Plot 87
5.3 Range Correlation Effect in AM 89
5.4 AM PM Verification Using Low-IF Doppler Radar System 92
5.5 Null-point Issue Involved in IF System Architecture under Saturation . . 95
5.6 Summary 97

6 Proposed Novel ENVSIL Radar for Remote Displacement Sensing 98
6.1 ENVSIL Radar Architecture 98
    6.1.1 Design Challenges for ENVSIL Radar 99
6.2 ENVSIL Radar Prototype 102
    6.2.1 VCO Module Design 103
    6.2.2 PLL Module Design 103
    6.2.3 Other Module Design 104
6.3 Coordinate Reconstruction 104
    6.3.1 Data-based Analytical Approach 104
    6.3.2 Optimization Approach using Genetic Algorithm 105
6.4 Displacement Sensing Using ENVSIL Radar 107
    6.4.1 Large Motion Linearity Test 107
    6.4.2 Small Motion Accuracy Test 109
6.5 Discussion 110
6.6 Summary 114

7 Conclusion and Future Work 115
7.1 Conclusion 115

7.2 Future Work 116

List of Figures

1.1 System diagrams proposed in the reviewed papers (a) Conventional single-channel Doppler radar system (b) Conventional IQ Doppler radar system (c) Double-sideband system (d) Low-IF Doppler radar system (e) Self-injection locked system (f) Envelope detection six-port network system. . 7

1.2 Spectrum diagram of the transmitted and received RF waveform of a CW Doppler radar system. 8

1.3 Measured RCS of a test subject from 1 GHz to 10 GHz at two scenarios when the test subject completely inhales and and exhales reported from [42] 9

1.4 Comparison among Doppler radar systems in perspectives of (a) FOM versus year of publication (b) FOM versus operating frequency (c) Operating frequency versus year of publication (d) EIRP versus detection distance. 12

1.5 Received power at radar front-end with a transmitting power of 1.5 dBm: theoretical versus measured [58]. 16

1.6 Measurement setup and measured output voltages of the PSIL radar with and without nearby clutter [10]. 17

2.1 Block diagram of the Dual-PLL Doppler radar system. 22

2.2 Block diagram of the digital signal processing algorithm 23

2.3 (a) Experimental setup for phase coherence validation. (b) Comparison between the measured and theoretical results of the normalized output power. 25

2.4 (a) Top view of the system setup for remote vital sign sensing. (b) Side view of the measurement setup. 26

2.5 15-second time domain signals for baseband I channel (BB_I), baseband Q channel (BB_Q) and the measured motion signal $x(t)$. 27

2.6 Normalized frequency spectrum of the detected motion signal $x(t)$ and the recorded reference signal from pulse oximeter sensor. 27

2.7 Photo of the compact Dual-PLL system module (a) TX board (b) RX board. 28

2.8 System diagram for the proposed dual-PLL based MIMO radar 29
2.9 System setup for proposed dual-PLL based MIMO radar 30
2.10 System calibration setup for the proposed dual-PLL based MIMO radar . 31
2.11 MIMO radar beam forming detection angle accuracy test 32
2.12 Vital-sign measurement setup for two subjects sitting next to each other 34
2.13 Vital-sign measurement setup for two subjects lying down with opposite direction next to each other 36
2.14 Measurement Results for two subjects sitting next to each other (a) Spatial power distribution plot with steering beam across the 2-D plane (b) Time-domain signal result processed for subject A (c) Frequency domain result between 0 and 2 Hz for subject A (d) Frequency domain result between 0.8 Hz and 2.5 Hz for subject A (e) Time-domain signal result processed for subject B (f) Frequency domain result between 0 and 2 Hz for subject B (g) Frequency domain result between 0.8 Hz and 2.5 Hz for subject B. . 38
2.15 Measurement Results for two subjects lying on the bed next to each other (a) Spatial power distribution plot with steering beam across the 2-D plane (b) Time-domain signal result processed for subject A (c) Frequency domain result between 0 and 2 Hz for subject A (d) Frequency domain result between 0.8 Hz and 2.5 Hz for subject A (e) Time-domain signal result processed for subject B (f) Frequency domain result between 0 and 2 Hz for subject B (g) Frequency domain result between 0.8 Hz and 2.5 Hz for subject B. 39

3.1 Noise modeling at the interface between IF amplifier and ADC. (a) Friis' equation to calculate P_{RFN} with a reference of a matched load connecting at the IF output. (b) An open node exists between IF amplifier and ADC due to the high input impedance of ADC. 42
3.2 Simulation data consisting all sources of phase noise levels for PLL ADF4351 and the total phase noise level of PLL LMX2594. 49

3.3 Caculated $\mathcal{S}_{\mathrm{corr}}(f_m)$ and $\mathcal{S}_{\mathrm{uncorr}}(f_m)$ with respect to different detection range d/λ. 49
3.4 Calculated noise and SNR results without coupling. (a) Motion signal and noise power density with respect to TX power. (b) SNR with respect to TX power. 51
3.5 Calculated noise and SNR results with a −40-dB TX-RX leakage. (a) Motion signal and noise power density with respect to TX power. (b) SNR with respect to TX power. 52
3.6 Phase noise measurement with changing PLL IC and delay between LO and RX signal. (a) Measurement diagram. (b) Measured power density for IF signal. 55
3.7 Coupling effect assessment with varying introduced power level of coupling (a) System diagram. (b) System setup. (c) Front view of the experiment setup. 57
3.8 (a) The measured IF spectrum with different levels of introduced coupling power. (b) Motion signal and Noise floor magnitudes for different coupling power levels. 59
3.9 System diagram for varying TX power level using array antennas. 60
3.10 Motion signal amplitude and measured noise floor amplitude measured in IF domain with varying TX power levels. 60
3.11 System diagram for RF cancellation using patch antennas. 62
3.12 System Setup for RF Cancellation 63
3.13 Motion signal amplitude and measured noise floor amplitude measured in IF domain with varying RF cancellation depth with using patch antennas. 64
3.14 Vital sign measurement setup with RF cancellation technique 64
3.15 RF cancellation technique during Vital sign detection result 65

4.1 Automatic RF cancellation implementation diagram. 67
4.2 Part of two-dimensional sweep done by the RF cancellation board with full range of attenuation and phase shift settings. 69

4.3 Diagram for stochastic gradient algorithm. 71
4.4 Parasitic effect validation test bench with changing TX signal phase shift. 71
4.5 Comparison with different algorithms by changing the phase shift of the TX signal. (a) Comparison in RF cancellation depth. (b) Comparison in processing time. 72
4.6 Automatic RF cancellation implementation setup with a subject sitting at 4 m away from the radar system. 73
4.7 Measurement result from 4-m vital sign detection. (a) 20-second time domain waveform that shows the RF cancellation process. (b) Frequency domain analysis without RF cancellation. (c) Frequency domain analysis after applying RF cancellation. 74
4.8 60-s spectrogram based on the demodulated baseband signal resulted from the 4-m vital sign detection. (a) Before applying RF cancellation (b) After applying automatic RF cancellation. 75
4.9 Through-wall measurement setup with a subject sitting 2 m away from the radar system. The obstruction consists of a 15-cm wooden wall in a California school building. 77
4.10 Measurement result from through-wall vital sign detection. (a) 20-second time domain waveform that shows the RF cancellation process (b) Frequency domain analysis without RF cancellation. (c) Frequency domain analysis after applying RF cancellation. 78
4.11 60-s spectrogram based on the demodulated baseband signal resulted from the through-wall vital sign detection. (a) Before applying RF cancellation (b) After applying automatic RF cancellation. 78

5.1 Diagram for the Doppler radar system with considering coupling effect. 82

5.2 MATLAB simulation results with (a) Normalized baseband motion detection power at the fundamental frequency in the form of AM and PM with $A_{CL} = 2A_r$, (b) Comparison between the simulation results of the PM operating-point positions with theoretical predictions considering four scenarios with $\frac{A_{CL}}{A_r}$=2,4,10 and 30. 86
5.3 IQ plots when coupling signal is at different levels. (a) No coupling signal considered (b) With coupling signal involved in the system (c)Scenario when AM is at its optimum point (d) Scenario when PM is at its two optimum points 88
5.4 Simulated relative noise power comparison among $RX_{pn}(t)$, $B_{Env}(t)$ and the prediction when directly applying the range correlation effect to $RX_{pn}(t)$. 91
5.5 System diagram for AM PM effect validation using a dual-PLL low-IF system. 93
5.6 Measured motion spectrum power resulted from the AM and PM involved in the signal with a separation distance of (a) d=0.6 m and (b) d=2 m . . 94
5.7 Example of a saturated IF signal in time domain and frequency domain. 95
5.8 MATLAB simulated results on the relative motion magnitude considering different motion signal phase offsets and relative coupling strength under saturation. 96

6.1 (a) System diagram for the proposed displacement sensing system (b) vector diagram for SIL system at null point 99
6.2 Simulated shape on an IQ plot due to the change of (a) coefficient a (b) coefficient b (c) coefficient c (d) coefficient d with sweeping values across: 0, 0.5, 1, 1.5 and 2. 101
6.3 Picture of the system setup for the ENVSIL radar 102
6.4 (a) Circuit diagram and (b)Photograph of the designed cross-coupled VCO module. 103
6.5 Percentage error in demodulated motion amplitude RMSE as a function of the SNR of the input baseband signals. 107

6.6 Measured time-domain waveform for charge pump output and envelope detection output in response to a 5-cm peak-to-peak motion displacement. 108

6.7 (a) Constructed IQ plot using the direct measurement results with $b = 0$ and $c = 1$. (b) Constructed IQ plot using coefficients identified by the OPTA method. 109

6.8 Demodulated phase from the target reflection signal and its phase error comparing with the theoretical values. 109

6.9 IQ plot for 8 motion segments with 4-mm sine wave motion separated by 5–mm spacing in-between. 110

List of Tables

1.1 System Parameters and FOM 11

2.1 Beam Forming Detection Angle Accuracy Test 33
2.2 Spatial Resolution Measurement 36

3.1 System parameters 50
3.2 Comparison between performance using the phased-array antenna and the patch antenna 61

4.1 Comparison between different setups for through-wall motion detection using LSTG @2 m away 76

6.1 Key Components Used in the System 102
6.2 Short Displacement Measurement Results of LSTG with RC Technique . 111
6.3 Comparison of Radar-Based Displacement Monitoring Systems 112

Abstract

Coupling Effect in Doppler Radar System Used for Remote Sensing

Remote vital sign detection has gained popular interests from researchers to conduct through-clothing and non-contact measurements of the chest wall motion induced by the heart beat and the respiration of the human subjects. Although many architectures have achieved the vital sign detection with decent sensitivity, the Doppler radar system is widely adopted by researchers due to its simple architecture, perfect phase coherence and its cost effectiveness. On the other hand, improvements on the Doppler radar system are imperatively needed on the topics of radar system sensitivity for increased detection robustness, spatial resolution for multi-subject detection and linear displacement demodulation. This dissertation is devoted to improve the Doppler radar system through comprehensive study on the coupling effect during the Doppler radar system.

In this dissertation, we first discussed the development on the system integration of a dual-PLL low-IF Doppler radar system using PLL with a shared input reference. Followed by this, a compact module design has been achieved for constructing the first 6x6 Doppler MIMO radar system. This Doppler MIMO radar has been measured with a detection angle accuracy within 1.5^o, which helps to accurately allocate the motion-sensitive area of the subject to increase the detection sensitivity. The 18^o spatial resolution enables the device to distinguish between vital sign signals from two different subjects measured at the same distance of 1.9 m away.

Next, we analyzed the coupling effect contributing to the residual phase noise in the dual-PLL low-IF system architecture and validated it through controlled experiments. Followed by this analysis, an integrated automatic RF cancellation module has been developed using microcontrollers along with the designed cancellation algorithm. This module has been tested under both in-air and through-wall vital sign detection scenarios, resulting in an effective SNR increase of more than 15 dB with a less-than 2 seconds of implementation time.

Lastly, the coupling effect has been studied on the modulation scheme associated with the remote target motion. Instead of the phase modulation due to the Doppler effect, the coupling effect also results in amplitude modulation at the received waveform. Our work investigated such effect through both theoretical derivations and interpretations in an IQ plot. Based on this finding, a new system architecture has been proposed for remote displacement sensing. The developed new architecture demonstrated a superior performance without using the mixer component, which greatly improves the power utilization efficiency for remote displacement sensing.

Acknowledgments

First and foremost, I would like to thank my advisors Professor Xiaoguang Liu and Professor Jane Q. Gu for their tremendous supports and guidance throughout my graduate studies at UC Davis. I am particularly grateful to Professor Liu for his herculean efforts in bringing in findings to support me and let me explore the research area of my interest. I am also extremely grateful to Professor Jane Q. Gu for the technical guidance and advice on paper revisions. It is such a privilege to work with them and this work could have not been accomplished without their supervision.

I would like to specially express my gratitude to the dissertation committee members and the qualifying exam committee members, Professor J. Sebastian Gomez-Diaz, Professor Anh-Vu Pham and Professor Jinyi Qi. Thank you all for the valuable suggestions and discussions over this work.

I also wish to thank Dr. Xiaomeng Gao for being such a great mentor and friend to me throughout most of my graduate studies. I have really benefited a lot from him through countless meetings and discussions on both technical and personal matters. I cannot image how hard my PhD could have been without him.

I am indebted to Prof. Hooman Rashtian for introducing me to the research path in my Junior year at college. I am greatly appreciated for the weekly meetings and patient guidance on not only the research project but also on my carrier development. It was the positive experience during that summer that solidified my decision to pursue this Ph.D degree.

I am particularly grateful to Dr. Xiaohu Wu for his generous help on my paper revisions and equation derivations. His work includes the detailed equation derivations in the Chapter 3.

I would also like to thank Dr. Heng Zhao, Chen Feng and Prof. Hong Hong for the collaboration on the MIMO project from brainstorming to building and programming the MIMO radar project together during the pandemic. I would like to thank all my colleagues in the DART lab, Dr. Songjie Bi, Jingjun Chen, Li Zhang, Mahmoud Nafe, Daniel Kuzmenko, Saleh Hassanzade, Hind Reggad, Te-Chen (Jenny) Lin, Min Gyo Jeong,

Jie Wang and Zhigang Peng, who have created an uplifting environment in the lab and have been great companies along this journey. They have helped me greatly and spared no efforts on all kinds of problems that I encountered during my studies.

Financial supports from the National Science Foundation (NSF), Cardia Motion LC, as well as the Electrical and Computer Engineering Department at UC Davis have made this work possible. It has been a great honor to have received all the assistanships to complete my Ph.D. study.

I would also like to thank my friend Zhichao Zhang for always being here for me and my family. I hope neither time nor distance will break our friendship apart.

I would like to contribute my sincerest appreciation to my beloved family. I am forever grateful to my parents, Maozhong Jiang and Lihua Liu, who have brought me up and have been my role models throughout my life. They taught me everything through their examples and poured their lifelong caring and endless supports on me. I would like to thank my grandparents, Dehai Jiang, Bingfeng Wang and Fuchen Liu who provided enormous cares and love in my childhood. Last but not least, my deepest appreciation and love to my wife Mengyao Lin, for her endless support and sacrifice on behalf of me. I dedicate this Dissertation to my family, whose encouragement and support have made this possible.

Chapter 1

Introduction

During the recent decade, there is an increasing demand for personalized patient monitoring device due to the rise in healthcare costs and the nursing shortages [1]. Data collected by National Center for Health Statistics shows that the cardiovascular disease is the top leading cause of death in the United States in 2020 followed by cancer and COVID-19 [2]. Among all the cardiovascular diseases, heart failure (HF) is a highly prevalent condition that affects 6.2 million adults in the United States [3]. This number is estimated to increase to 10 million by the year 2040 [4]. Despite the therapeutic advancements in recent history, HF patients are reported to have frequent hospitalization with a readmission rate of 40.2% within 90 days of discharge [5]. This costs the health care system nearly 24.6 billion dollar annually [6] and it is likely to cost patients a minimum of $\$\,34,000$ in hospitalization per year [5]. To contain the readmission rate and reduce the hospitalization cost, noninvasive vial-sign monitoring system has gained a lot of interest from researchers to monitor patients' vital sign condition such that early interventions can be deployed to reduce re-hospitalization rate and improve outcomes of the patients.

Although wearable devices were invented to conduct close contact with people for constant health monitoring, the extra contact attached to the body and the need to frequently replace the battery increase the difficulty in adaptation and prevent it from becoming widely acceptable. Therefore, the remote detection using wireless devices is gaining popularity in the field of research aimed at acquiring the vital sign data without any discomfort or interference with patients' mobility.

Electromagnetic (EM) wave has been widely used for transmitting and receiving data wirelessly through phase and amplitude modulation to provide long-range communication. Based on the same idea, the Radar-based vital sign monitoring device detects the modulation of the EM wave reflected back from the human body. This modulation contains the essential information of the tiny chest-wall vibration induced by the respiration and heart-beat motion of the human subject. In literature, there are three architectures that have been extensively investigated for remote sensing application: the ultra-wide band (UWB) radar, the frequency-modulated continuous-wave (FMCW) radar and the continuous wave (CW) Doppler radar. The UWB radar, also called pulse radar, transmits a very-sharp pulse signal which typically lasts in order of nanosecond. Even though short pulse width (large bandwidth) benefits the UWB radar that results in high resolution in detection distance, the generation of such pulse suffers from power efficiency issue. Compared with the UWB radar, the FMCW radar normally operates with a lower bandwidth which compromises the range precision of the detection [7]. Due to the less phase coherence comparing with the Doppler radar, the phase detection sensitivity of FMCW radar is limited. On the other hand, the Doppler radar only transmits a single-tone waveform which is spectrum efficient. This property also makes CW system attractive due to its cost-effective and simple architecture. Additionally, its high level of phase coherence and precision in displacement measurement [7] drives the Doppler radar to be widely adopted.

Despite the recent advancement in Doppler radar for developing various architectures to improve radar sensitivity and avoiding random body motion to reduce interference, there is missing pieces on understanding and analysis of the coupling effect during the Doppler radar system. For example, the null-point issue and the non-linearity issue for the self-injection locked system, the noise analysis of the envelope detection system and the relationship between different developed system architecture (especially the self-injection locked system and the envelope detection system) all demands interpretations. Besides that, researchers also hold different perspectives on the coupling effect to the noise contribution of the Doppler radar system.

In this dissertation, we focus on the topic of studying the coupling effect to the noise contribution to the Low-IF Doppler radar system and to the change of modulation scheme reacting to the detected motion. This dissertation proposes an effective technique for sensitivity improvement as well as a novel displacement sensing system architecture for high power-efficiency.

1.1 Overview of Doppler Radar System Architectures for Vital Sign Detection

The first ever physiological detection using microwave radar can be traced back to 1960 with Moskalenko's presentation of electrodeless recording of biological volume changes [8]. Followed by this investigation, the Doppler radars have been extensively studied in the past decades as a viable approach for unobtrusive detection and monitoring of human vital signs such as respiration and heart rates. Several system architectures have been demonstrated, such as the self-injection locking (SIL) [9–12], envelope detection [13–17], and the conventional Doppler scheme [18–24]. The target motion induces changes in the frequency, amplitude, or phase of the RF signal. From a signal recovery point of view, conventional Doppler radar systems can be further categorized into the direct conversion (DC) and the intermediate frequency (IF) systems. The DC output signals are directly down-converted using mixer component whereas the IF system adopts digital downconversion in the digital domain to process the motion information. In this section, the history and the system performance of these different system architectures will be briefly reviewed.

Conventional Single-Channel Doppler Radar System The first commonly adopted architecture for vital sign detection is the direct-conversion (DC) system architecture where it uses a mixer to demodulate any amplitude or phase modulation inside the received waveform to the baseband voltage. This system diagram is shown in Fig.1.1 (a) where this architecture is popularized for life detection through barrier reported in [25, 26] in the 20th century.

Conventional IQ Doppler Radar System From 2001, Dr. Amy Droitcour (then a student from Stanford University) started to investigate on integrated circuit (IC) integration for the Doppler radar system used for remote respiration detection [27]. She demonstrated the null point issue associated with the single-channel system where the performance of the system varies with the phase difference between LO and RX signal [18]. When the phase difference offset is near 0 degree, a large dc offset could appear at the baseband output with little response to the motion variation. On the other hand, when the phase offset is at 90 degree, the system operates at its optimum point with a high sensitive to the target motion.

To overcome this null-point issue, the IQ Doppler radar system with a quadrature mixer was proposed in [18] as shown in Fig.1.1 (b). In this architecture, a quadrature splitter has been used to generate a pair of I/Q signals with a phase difference of 90°. The two signals then drive the LO port of two mixers separately. With this two-channel approach, the phase offset between LO and RX will never get to a null-point at the same time. Furthermore, the I/Q channel information can be plotted on an IQ plot which can be further used for phase demodulation after DC offset calibration. This system architecture gained lots of popularity due to its simplicity and robust performance for remote detection and has been adopted in [19, 28–34] and many more other papers.

Double-Sideband Doppler Radar System In the mean time, to tackle the null point issue and the receiver saturation problem due to the high dc offset, a double-sideband(DSB) architecture was adopted for improved detection sensitivity [35]. The system diagram is shown in Fig.1.1 (c) where an IF source is adopted to construct an heterodyne system to avoid the LO leakage from the first RF mixer in the DC system. By adjusting the frequency of the IF or RF sources, the system null points can also be overcome. Thus, [14–17, 36] have adopted such system architecture to demonstrate a higher sensitivity comparing with the conventional IQ system. Even though this architecture has shown a higher sensitivity, it did not gain as much popularity as the DC system due to its more complex architecture design and the potential design consideration to limit the harmonic modulations due to the adoption of the double-sideband spectrum and the downconversion using two mixers.

Low-IF Doppler Radar System Flicker noise acts as a typical noise contribution to any system with a dc output which can limit the SNR of the detected signal at certain scenarios [37, 38]. Therefore, to improve the system sensitivity by avoiding the flicker noise effect near dc, a low-IF Doppler radar system was developed [22] where its baseband is shifted away from dc to a low-IF frequency. The architecture is shown in Fig.1.1 (d) where the baseband output is directly sampled using ADC. To demodulate the motion signal, a further demodulation process is performed inside the digital domain. The system complexity is still considered low as the frequency selection is made to be 1kHz. On the bright side, the I/Q mixer only creates a single-tone RF waveform which reduces the concern for harmonic interference during the downconversion process. On the other hand, the I/Q mismatch could cause concern for the purity of the RF waveform which would affect the overall system performance.

Alternatively, the system architecture proposed by [21] is able to address this concern by generating two RF signals using two separate RF sources that share the same reference. This system architecture avoids the potential image problem in [22] while maintaining the phase coherence between the two RF waveform that have different frequencies. This architecture is also the one adopted in this dissertation and will be studied in more details in the next chapter.

Self-Injection-Locked Radar System Unlike the previously mentioned system architectures that directly demodulate the phase variation of the received RF waveform, the self-injection-locked system converts this phase modulation (PM) to frequency modulation (FM) of a VCO source [9, 11]. The SIL system diagram is displayed in Fig.1.1 (e) where the frequency demodulation has multiple different designs in the past literature. [9, 12] utilize a combination of a delay line and a mixer to effectively convert FM back to PM and further downconvert it to baseband. By adopting this SIL system architecture, the PM can be amplified through VCO design in the RF domain. This is in addition to the conventional voltage amplification at the baseband which is commonly adopted by the other architectures. Besides the delay-line approach, there are two other methods for demodulating the FM of the VCO. One is through PLL locking which converts the FM to the voltage variation at the PLL charge pump output [10]. The other method is to use a microwave differentiator to convert FM to AM which is then demodulated by a power detector [39]. Comparing with the conventional IQ system and the IF system, the SIL system reports a farther heart-rate detection distance, which demonstrates its competitive performance.

Envelope Detection System Six-port network was first invented in 1977 to detect the phase and amplitude response as an alternative network analyzer [40]. Based on this mechanism, [13] first adopts this architecture for remote vital sign detection with its system diagram shown in Fig.1.1 (f). The six-port network can be generalized as a summation tool for the transmitted and the received RF signals. Inside the six-port network, a ring-shaped coupler is used to create 4 output channels that combined the two RF inputs differently with 4 different phase offsets in-between them. The phase shifts are separated by 90^o. Followed by the output of the six-port network, 4 power detectors are used to extract the power level of each signal path with combined waveform between the two RF inputs. Finally, after the system calibration, the 4 baseband outputs are used to extract the relative phase difference between the transmitted and the received RF inputs, which is then used to detect any phase variation caused by the remote target motion. In this dissertation, we call this architecture the envelope detection system due to the adoption of power detector at the output of the six-port network. There has been only one paper that reports to detect remote vital sign using this architecture so far. For such system, the only interpretation provided by [13] is that the six port network itself can be viewed as an alternative network analyzer which demodulates the phase and amplitude response when comparing between the two RF signals. Besides that, the paper also mentioned that the magnitude of two RF input should be as close as possible for highest detection sensitivity.

After discussing the various architectures developed by in the past, the performance

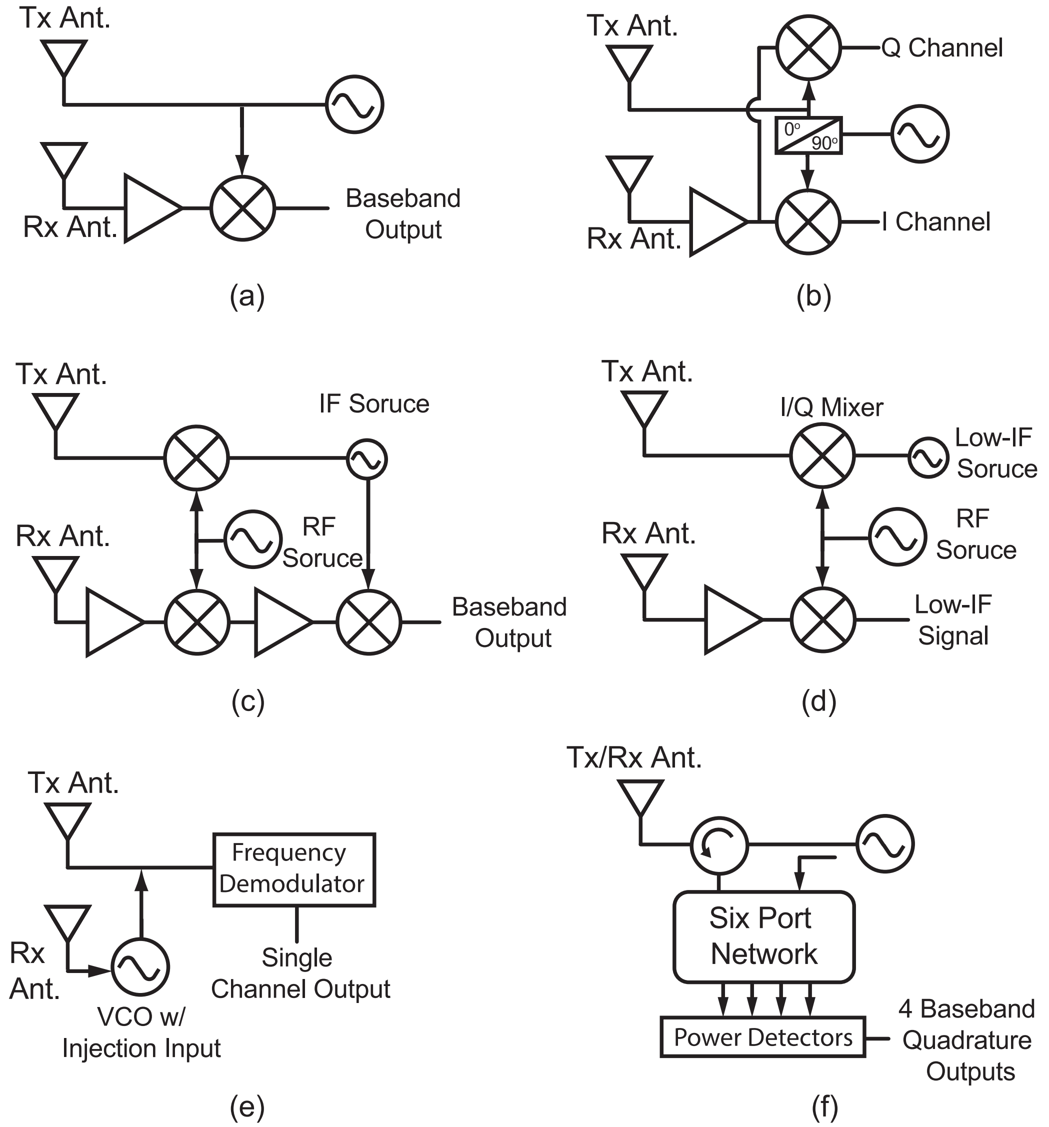

Figure 1.1: System diagrams proposed in the reviewed papers (a) Conventional single-channel Doppler radar system (b) Conventional IQ Doppler radar system (c) Double-sideband system (d) Low-IF Doppler radar system (e) Self-injection locked system (f) Envelope detection six-port network system.

based on their reported results are compared in this section.

1.1.1 FOM Metrics Design for Detection Sensitivity Comparison

Among the system parameters reported by different papers in literature, their values are always different in transmitted power level (P_T), antenna gain (G_{ANT}), operating frequency as well as the detection distance (d) for reporting a successful heart-rate detection. To design an FOM that calibrate the difference in all these parameters, we convert all the system parameters to the detected motion signal level (P_M) to serve as assessment for the system performance.

There are two major factors that contribute to P_M in the system, which are the system received power level (P_r) and the phase modulation depth induced by the target motion. The spectrum diagram of the transmitted and the received RF waveform is shown in Fig. 1.2 where the transmitted RF waveform has a single-tone spectrum centered at ω_{RF}. On the other hand, due to the phase modulation induced by the target motion, the received RF waveform does not only contain a reduced-power spectrum centered at ω_{RF} but it also has sideband spectrum located at $\omega_{RF} \pm n\omega_m$ where ω_m is the target motion frequency and n represents the harmonic number of the motion frequency offset. With assuming the target moving in a sinusoidal trajectory with an amplitude of x_m, the sideband magnitudes are expect to follow the relationship of the Bessel function $J_n^2(4\pi x_m/\lambda)$ [14], where $J_n(x)$ can be approximated as:

$$J_n(x) \approx \frac{1}{2^n n!} x^n. \tag{1.1}$$

Therefore, the magnitude difference between the P_M and P_R is determined to be $4\pi^2 x_m^2/\lambda^2$. To further calculate the absolute power level of P_M, we need to find P_R based on the reported transmitted power (P_T) of the constructed system.

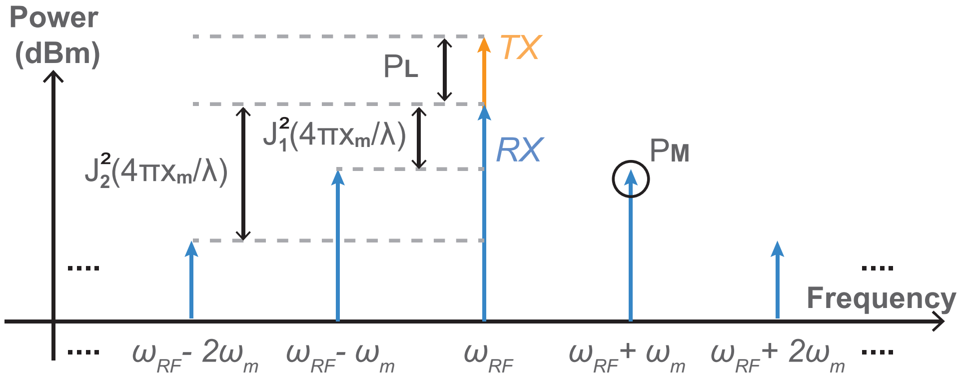

Figure 1.2: Spectrum diagram of the transmitted and received RF waveform of a CW Doppler radar system.

According to [41], the link budget of the Doppler radar system with assuming a perfect matching between the antenna and the radar system follows:

$$P_R = P_T P_L = P_T \frac{G_{ANT}^2 \sigma_{eff} \lambda^2}{(4\pi)^3 d^4}, \tag{1.2}$$

where P_L, σ_{eff} and λ represent the path loss, effective radar cross section area (RCS) of the subject target and the wavelength of the operating frequency respectively. Most of the parameters in the equation are directly associated with the system design parameters except for the RCS, which is varied greatly with person's movement as well as frequency. This effect has been reported in [42] where the RCS of a test subject is measured at the end of the inspiration and expiration process across frequency from 1 GHz to 10 GHz. Since there is not a clear relationship between the RCS and the frequency, the RCS is not included in sensitivity assessment for the system performance comparison.

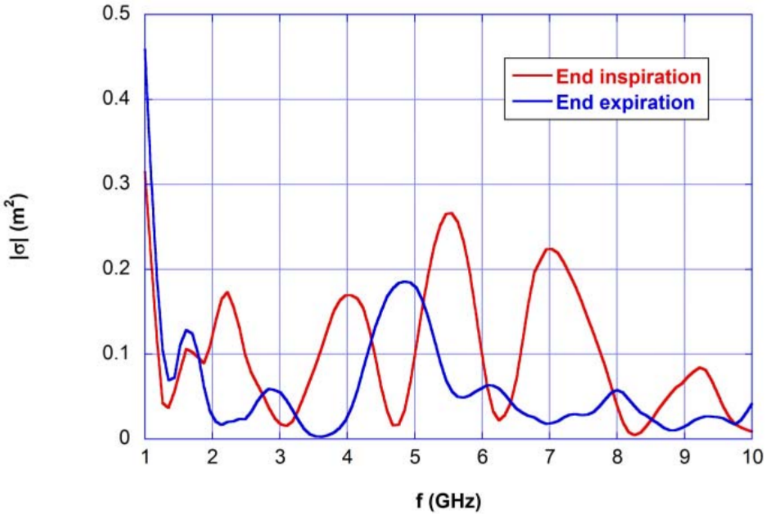

Figure 1.3: Measured RCS of a test subject from 1 GHz to 10 GHz at two scenarios when the test subject completely inhales and and exhales reported from [42]

After combining (1.1) and (1.2), the FOM is designed as a parameter that intends to reflect on the sensitivity of the circuit receiver system such that it is inversely proportional to the equivalent noise floor level after the RX antenna. The noise floor level can be found by subtracting the detection SNR from the detected motion power. Due to the lack of quantified SNR value reported by the paper on its detected heart-motion waveform, we assume the same SNR is required for achieving the successful heart rate detection. Thus, this FOM does not precisely describe the system sensitivity due to the lack of detection SNR input; Instead, it only indicates the lowest sensitivity the system can achieve. Therefore, the FOM can be established by comparing the system sensitivity with a reference system that has a $P_T = 0\,\mathrm{dBm}$, $G_{ANT} = 0\,\mathrm{dBi}$ and $d = 1\,\mathrm{m}$. The equation is shown as follows:

$$FOM = 10\log_{10}\frac{d^4}{P_T G_{ANT}^2} \tag{1.3}$$

where this equation assumes that the subject target among all papers provides a similar RCS which is also unvaried across all operating frequencies. Interestingly, the operating frequency does not affect this FOM results. This is because when the frequency increases, not only does it benefit from the higher phase modulation induced by the motion, the path loss also increases due to (1.2). A major limitation to this FOM is that this does not account for the motion SNR detected by the system. This is due to the lack of quantification of the reported detection SNR of the vital sign motion.

With using the FOM equation, the system parameters along with the resulted FOM value have been listed in Tab.1.1.

1.1.2 System Performance Trend

Due to the lack of target motion SNR quantification, The FOM assumes all successful heart-rate detections to share the same detection SNR for the motion signal. Therefore, the FOM reported in Tab. 1.1 does not fully represent the exact performance of the system; Instead, it indicates the minimum sensitivity reported by the system. To illustrate the trend of the reported FOM developed by system architectures, the parameters from Tab. 1.1 are plotted in Fig. 1.4.

Fig. 1.4 (a) shows the FOM versus the year of publication where the sensitivity of the developed Doppler radar system has gradually increased over the years with 67–dB increase from year 2004 to year 2022. In this figure, our system demonstrates a competitive performance among all the developed systems.

Fig. 1.4 (b) and (c) plot the FOM versus the operating frequency and operating frequency versus the year of publication. As analyzed in FOM calculation, the frequency does not affect the sensitivity of the radar system with a trade off between the modulation depth and the path loss. This is backed up by Fig. 1.4 (b) where there is not an

Table 1.1: System Parameters and FOM

Ref.	Year	Architecture	Freq.	P_T	G_{ANT}	d	FOM
[18]	2004	IQ	1.6 GHz	10 dBm	6 dBi	0.85 m	-24.8
[14]	2006	DSB	27 GHz	-18.5 dBm	20 dBi	2.5 m	-5.6
[15]	2007	DSB	5 GHz	-17 dBm	9.8 dBi	2.8 m	15.3
[16]	2008	DSB	5.5 GHz	-12.5 dBm	9 dBi	2 m	6.5
[28]	2009	IQ	2.4 GHz	0 dBm	6 dBi	2 m	0
[43]	2009	IQ	2.4 GHz	0 dBm	0 dBi	0.5 m	-12.0
[19]	2010	IQ	2.3 GHz	-5 dBm	17 dBi	1.5 m	-22.0
[21]	2010	IF	2.4 GHz	0 dBm	10 dBi	2.5 m	13.1
[44]	2012	IQ	97 GHz	15 dBm	43 dBi	15 m	-54.0
[10]	2013	SIL	2.4 GHz	-22 dBm	12 dBi	4 m	22.1
[13]	2013	Env.	24 GHz	-25.6 dBm	20 dBi	1 m	-14.4
[22]	2014	IF	2.4 GHz	-10 dBm	8 dBi	3 m	13.1
[23]	2017	IF	2.4 GHz	-13 dBm	12.8 dBi	3 m	6.5
[31]	2018	IQ	60 GHz	-0.1 dBm	17 dBi	1.2 m	-30.7
[12]	2019	SIL	2.4 GHz	12 dBm	12 dBi	1.5 m	-29.0
[36]	2020	DSB	100 GHz	-36 dBm	20 dBi	2 m	8.0
[24]	2021	IF	2.41 GHz	-6.5 dBm	6 dBi	1.8 m	4.7
[11]	2021	SIL	5.8 GHz	0 dBm	14 dBi	8 m	8.1
[45]	2021	SIL	2.4 GHz	0 dBm	6 dBi	8.4 m	25.0
This Work	2022	IF	2.45 GHz	-31 dBm	6 dBi	4 m	43.1

upward-trend relationship monitored between the FOM and the operating frequency. Furthermore, Fig. 1.4 (c) shows that there is no trend or preference of developing a mmWave system lately; Instead, most of the systems are designed to operate in ISM bands which are convenient to build using commercial ICs without sacrificing on the system sensitivity. In some cases, higher frequency may be preferred if a small form factor is required during the design. However, the harmonic interference plays more effect during mmWave system

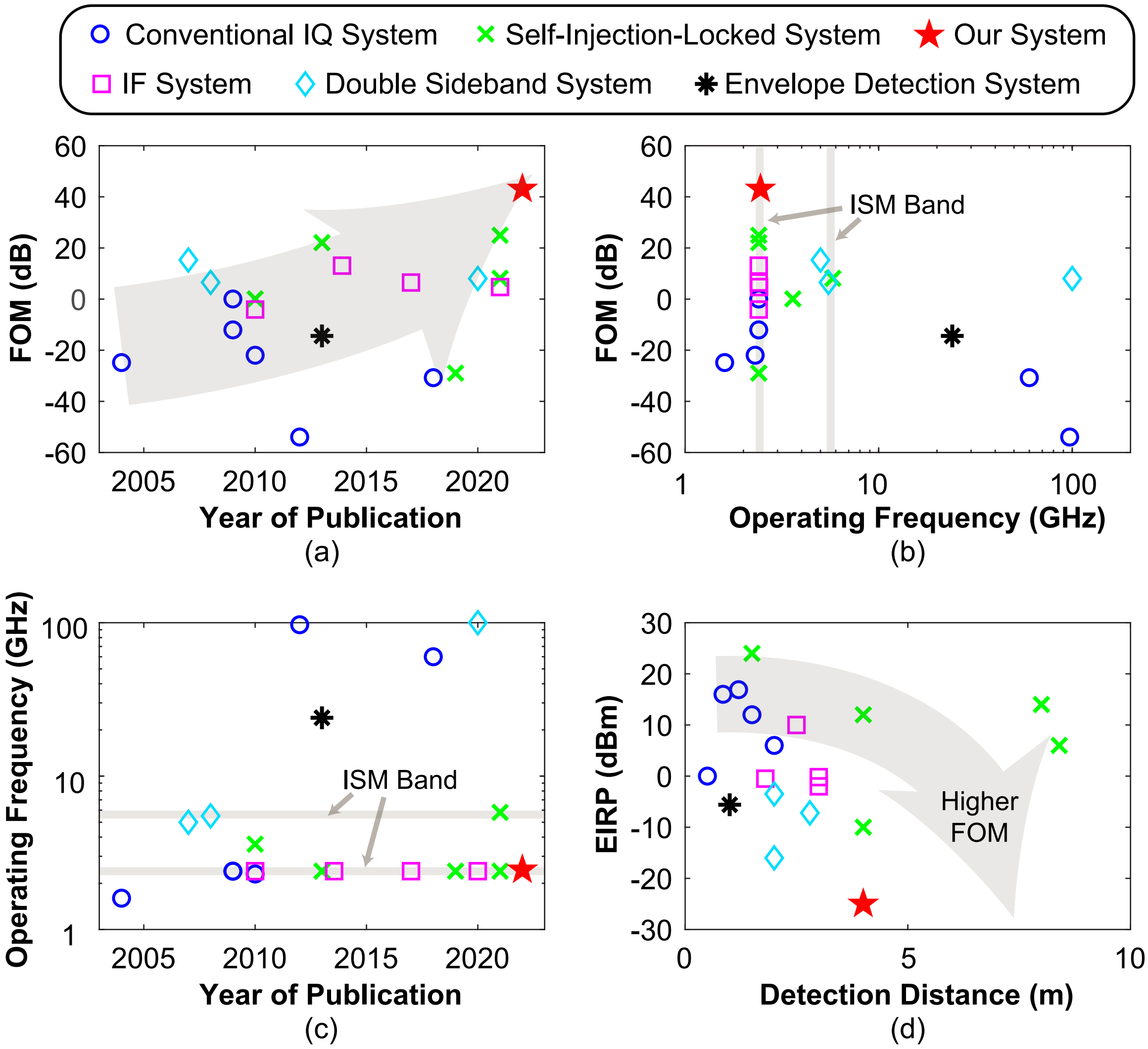

Figure 1.4: Comparison among Doppler radar systems in perspectives of (a) FOM versus year of publication (b) FOM versus operating frequency (c) Operating frequency versus year of publication (d) EIRP versus detection distance.

which creates more difficulty on the signal-processing side [46].

Fig. 1.4 (d) shows the effective isotropically radiated power (EIRP) versus the detection distance where we see that the SIL systems typically report a very long detection distance. Thus, if only compared using detection distance, the SIL system clearly outperforms other system architectures. However, we would like to point out that both EIRP and the detection distance need to be considered when comparing detection sensitivity among systems as the detection distance can be easily extended by increasing transmitted power if the system noise floor is limited by the thermal noise.

1.1.3 Spatial Resolution Review

Due to the fundamental limit to the single-channel Doppler radar, the system cannot distinguish between different movements detected within the radar coverage. This effect can be viewed such that each detected motion signal contributes to a vector moving in a circular trajectory inside an IQ plot. With multiple vectors adding up together, it yields a single vector with a combined complex movement. Due to the irreversible property of the vector summation, the result can not be decomposed to recover the true motion signal contributed by each single vector (target movement). As a result, detection using multiple receiving and transmitting channels is adopted for multi-subject vital sign detection, which creates a controlled narrow beam steering across the space.

Past studies have been done to achieve multi-subject vital sign detection using one-dimensional beam steering. In the work [47], T. Sakamoto et al. achieved two-subject respiration detection based on a SIMO radar platform. This improves the spatial resolution of the radar in one dimension. Followed by this, a 4-element injection-locked oscillators (ILO)-based phased-array system was developed by C. Hsu et al. for increased spatial resolution with beam steering in azimuth direction [48]. This SIMO radar demonstrated enough spatial resolution and high detection sensitivity to accurately detect heart rate from the three subjects simultaneously.

To further extend the beam steering capability to two dimensions, the multi-input-multi-output (MIMO) Doppler radar system has been further studied. Nosrati et al. constructed a phased array MIMO radar prototype to realize respiratory rates detection from two human subjects by steering a concurrent dual-beam to point at two subjects separately [49]. Another FMCW MIMO radar is constructed by A. Ahmad et al in [50] where the conducted experiment demonstrated a successful detection of the respiratory motion from two subjects simultaneously. So far, the previously designed MIMO radar systems are not sensitive enough to demonstrate accurate heart rate detection from multiple subjects at the same time during a single acquisition. Therefore, a MIMO radar with a more robust system design and a higher detection sensitivity needs to be further investigated.

1.2 Overview of Remote Displacement Sensing Using Doppler Radar

Even though the Doppler radar can effectively detect the remote vital-sign signal through the phase modulation of the RF waveform, the system detection output is not perfectly linear to the target motion. This is due to the combination of the coupling effect and the null-point issue inside the system. To precisely measure the displacement of the target motion remotely, a number of system architectures and algorithms have been proposed and investigated in the past.

As a main challenge for displacement demodulation using a conventional IQ radar, the paper [32] first suggested that a precise estimation of the projected circle center in an IQ plot is required to eliminate the dc offset voltage of the arc traced by the detected target motion. Continuing from this investigation, achievements have been made in circle center estimation algorithm include the development of heuristic estimator in [32] and the Levenburg-Marquardt (LM) algorithm developed to improve the robustness for circle center estimation even if the the arc has a increased measurement error, imperfect curvature and un-uniformed data distribution [51]. To improve the estimation algorithm efficiency, the Least Mean method is proposed in [52].

In the work of [53], the large motion displacement accuracy was improved by adopting an elliptical fitting method to compensate for the I/Q imbalance effect in the conventional IQ radar. On the other hand, the performance of the center estimation algorithm degrades with decrease in arc length or motion amplitude detected by the system. To address this limitation, the radius correction method proposed in [33, 54] effectively increases the arc length by shifting the small arc multiple times on the IQ plot to extend the effectiveness of circle center estimation to small motion displacement.

Overall, these prior advancements were built up on the conventional IQ radar system which has been the only architecture adopted for displacement sensing until the recent years when Wang [12] proposed a different system architecture using a QSIL radar. However, the I/Q mixer is still adopted as the primary demodulation component for this proposed system despite the usage of an SIL VCO source. Additionally, a 22-ns delay line is required by the proposed system, which increases the system complexity. Despite the growing interest in the SIL system development, few studies have explored the development of alternative simple system architectures used for displacement sensing using an SIL VCO source. As for the envelope detection system, to the best of the author's knowledge, there has not been any reported research demonstrating its displacement sensing function so far.

1.3 Overview of Coupling Effect in Doppler Radar System

Leakage/coupling have always existed in Doppler radar system where the coupling sources include the antenna mutual coupling, the surface reflection from stationary objects and other direct leakage from TX to RX path. By having excessive leakage/coupling during the system, it can easily saturates the system receiver. This was the major issue for the underground life-detection system where the obstruction in-between the system and the subject creates a strong coupling path despite the high-isolation antennas adopted in the system. Therefore, Lizuka, et al. [55] first implemented the coupling cancellation technique to cancel the surface reflection from the concrete to improve the system dynamic range. This approach requires manual adjustments of the phase shifter and the attenuator, thus it is quite time consuming. In 1991, an automatic coupling cancellation subsystem was firstly designed by Chuang, et al. [56] using a microcontroller for processing time reduction. Followed by that, more automatic coupling cancellation has been demonstrated in [19, 57–61]. These implementations aim to address the receiver saturation effect and further extend the dynamic range of the radar receiver.

As the research topic being redirected towards the remote vital sign detection through open space, the coupling strength has been greatly reduced. However, according to [58], the coupling strength inside a typical Doppler radar still dominates over the target reflection signal. The measurement results are re-posted in Fig. 1.5 where the spectrum

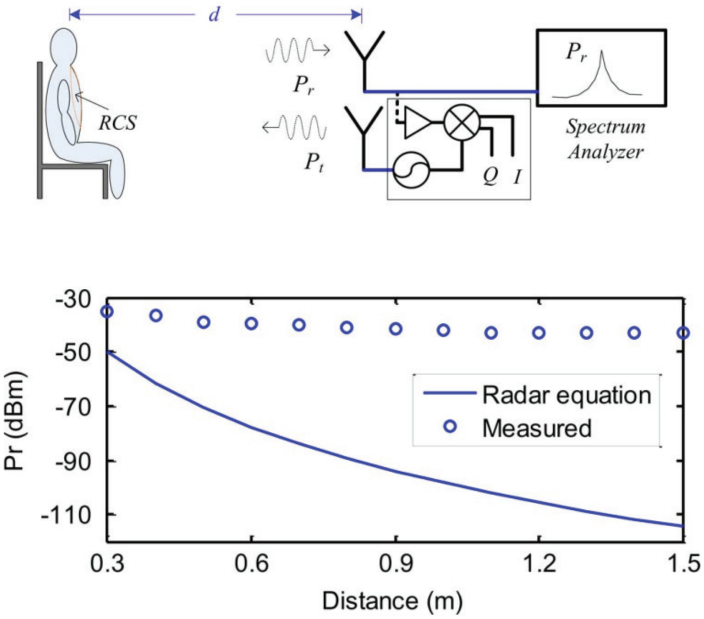

Figure 1.5: Received power at radar front-end with a transmitting power of 1.5 dBm: theoretical versus measured [58].

analyzer directly measures the power level received at the receiver patch antenna. The measured data is compared with the theoretically predicted target reflection power based on the radar equation. The large difference between the prediction and the measurement results indicates that the coupling still plays an important role in the Doppler radar system, especially for the long-distance detection scenario.

Unlike the agreement on the receiver saturation due to the coupling effect, researchers held different perspectives on its effect towards creating additional noise inside the conventional IQ system. In 2008, Yamada et al. [37] found out that the excessive leakage inside the mixer can drive up the flicker noise level at the mixer output. In return, the flicker noise can also be effectively suppressed after applying coupling cancellation. Specifically, their work reports a 19.3-dB flicker noise reduction through a 17-dB LO leakage cancellation. This finding is not widely accepted by researches, for example, a paper published in 2013 [58] writes that "However, this (the strong coupling) does not affect the radar sensitivity because it does not contain phase-modulated information and will generate a DC offset after the mixer."

For the SIL system, the coupling effect has been tested in [10] by using a clutter copper plate as an additional target. The measurement result showed that there is no

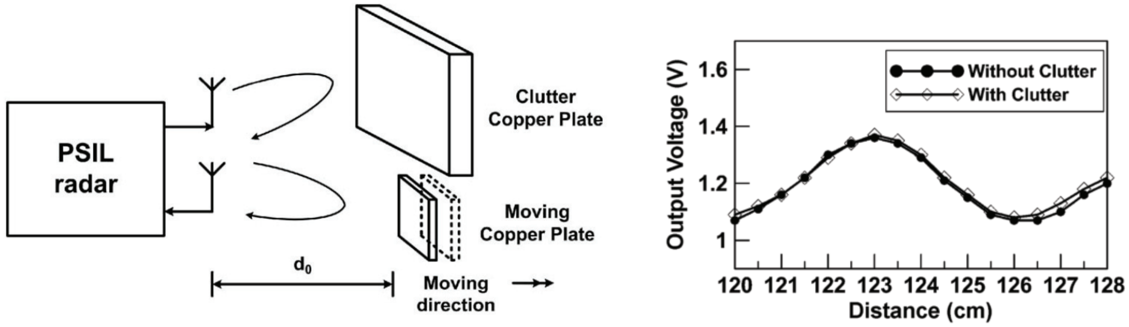

Figure 1.6: Measurement setup and measured output voltages of the PSIL radar with and without nearby clutter [10].

difference in signal level with and without the clutter copper plate placed besides the target. However, we believe this constant signal level comparison does not conclude a negligible effect from the coupling and there is a lack of noise floor measurement due to the coupling effect.

On the hand, the envelope detection system developed in [13] inherently has a source of coupling that mixes with the received signal. Even though it is clear that the six-port network can be viewed as an alternative network analyzer, to our knowledge, no one has analyzed the noise performance of such system under the vital sign detection scenario.

Overall, while the coupling effect results in a high power level at the receiver, its contribution to the system noise level still remains unclear inside a Doppler radar system. Therefore, the noise contribution due to the coupling effect still worth further investigation.

1.4 Summary of Dissertation

In this dissertation, the coupling effects for Doppler radar system are extensively studied. These include the analysis and verification on the coupling effect to elevating noise contribution inside the low-IF Doppler radar system. This dissertation also discusses the amplitude modulation under the effect of excessive coupling. To suppress the noise level contributed from the excessive coupling, the automatic RF cancellation has been developed to achieve a low-power highly-sensitive vital-sign detection radar system. Based on the amplitude modulation, a new system architecture has been proposed for remote displacement sensing. This new architecture offers in-depth interpretation to view the relationship among the conventional radar system, the SIL system and the envelope detection system. Other discipline involves the integration of the low-IF dual-PLL system and a MIMO radar system development to increase detection spatial resolution. The structure of the dissertation is organized as follows.

Chapter 1 has presented an overview of general health facts on the importance of the cardiopulmonary functions monitoring. To meet with the demand for easy-use and contactless vital sign monitoring system development, the Doppler radar has gained popular interest from researchers. Followed by this motivation, multiple system architectures developed in the past have been developed and their sensitivity performance have been compared with each other to review the performance trends of the developed Doppler radar systems. Besides the detection sensitivity, the spatial resolution, displacement demodulation ability and coupling effect have been reviewed in this chapter to provide a full background analysis on the advancements made in the past.

Chapter 2 discusses the integration of the low-IF Doppler radar system by using a dual-PLL architecture with a shared reference. The phase coherence is validated through experiments to demonstrate the feasibility of such method. After reducing the form factor of the radar system, a 6x6 MIMO system has been constructed using the compact radar modules. The developed MIMO system demonstrates a state-of-the-art sensitivity for distinguishing and detecting heart-rate information from two subjects.

Chapter 3 provides noise and SNR analysis to the dual-PLL IF system where the PLL flicker noise is identified as the major contribution to the baseband noise floor which limits the SNR of the system. These analysis is then validated through a series of quantified experiments using a controlled linear-stage actuator. To achieve a higher detection sensitivity, the RF cancellation has been applied to test its effectiveness on reducing the noise level caused by the excessive coupling strength. This cancellation technique is also conducted on vital sign detection to demonstrate its improvement on the system detection sensitivity.

Chapter 4 presents an automatic RF cancellation module and algorithm development. Instead of the manual adjustment adopted in the previous chapter, the automatic RF cancellation determines the optimum settings for the phaseshifter and the variable attenuator in less than 2 seconds. This greatly improves the robustness of the RF cancellation technique to be implemented for real-world applications. The developed system presents a 4-m heart-rate detection from a test subject with only transmitting a CW waveform with a power level of $-31\,\mathrm{dBm}$.

Chapter 5 analyzes the modulation scheme inside a Doppler radar system due to the target movement. The analysis provided an insight to the orthogonal relationship between the amplitude modulation and the phase modulation. This chapter analyzes the range correlation effect during the envelope detection system and points out that during the null point of the SIL system, the motion information gets converted to amplitude change at the received waveform. Thus, it leads to the proposed system architecture described in Chapter 6.

Chapter 6 develops the ENVSIL system which combines the SIL system with the envelope detection system where they compensate each other during their null point condition. The design challenges and proposed solutions are discussed to maintain the the orthogonal relationship between the envelope detection and the SIL system outputs. Such relationship is utilized for displacement sensing of the remote object through I/Q demodulation after coordinate reconstruction processed for the measurement data.

Chapter 7 summarizes the main contribution in the dissertation. A list of topics of the future work as expansions of the preliminary studies will be provided.

The main contributions of this work are either published or are currently under preparation for publication in the following conferences and journals:

- X. Jiang, X. Gao, X. Wu, Q. Gu and X. Liu, "Automatic RF Cancellation for Improved Remote Vital Sign Detection Using Low-IF Dual-PLL Radar System," IEEE Transactions on Microwave and Techniques (Preparing for Submission).

- X. Jiang, X. Liu and Q. Gu, "A Mixerless Displacement Sensing System Based on Amplitude and Phase Modulation inside the Doppler Radar System with Coupling," IEEE Transactions on Microwave and Techniques (Preparing for Submission).

- C. Feng, X. Jiang and et al., "Multitarget Vital Signs Measurement With Chest Motion Imaging Based on MIMO Radar," in IEEE Transactions on Microwave Theory and Techniques, vol. 69, no. 11, pp. 4735-4747, Nov. 2021, doi: 10.1109/TMTT.2021.3076239.
- X. Jiang, X. Gao, H. Zhao, H. Hong and X. Liu, "A Compact Digital Low-IF Dual-PLL Doppler Radar for Remote Vital Sign Detection," 2021 IEEE 21st Annual Wireless and Microwave Technology Conference (WAMICON), 2021, pp. 1-4, doi: 10.1109/WAMICON47156.2021.9443582.

Chapter 2

IF System Development for Improved System Compactness and Spatial Resolution

2.1 Introduction

Critical design challenges of vital sign monitoring radar systems include primarily the cost and sensitivity. Because vital sign signals are usually very low frequency (0.1–10 Hz), many recent radar designs have adopted the digital-IF architecture to minimize the impact of flicker noise in the low-frequency amplifier stages [22]. However, existing demonstrations of digital-IF radar systems rely on quadrature heterodyne architectures for the generation of the transmitted (TX) signal and the local oscillator (LO) signal with a narrow frequency spacing. Good component matching is required to generate a clean TX signal with low spurious emission. For lab demonstrations, bench-top frequency synthesizers have been used [21, 23]. However, these setups are generally bulky and expensive.

In this chapter, a compact digital low-IF Doppler radar architecture using two coherent phase locked loop (PLL) is proposed. The TX and LO signals are generated directly from the two PLLs without using quadrature up-conversion mixers. The two PLLs are locked to the same reference signal to maintain frequency and phase coherence. Motion of the radar target is reconstructed in the digital signal domain. As such, there is no amplitude or phase imbalance issues in this system. With further expanding this system architecture, a 6x6 MIMO radar is further constructed to improve the spatial resolution of the radar detection. Since the vibration induced by subject's chest contributes to the majority of the motion information, the developed MIMO radar can always allocate this area for optimal vital sign detection.

2.2 Architecture of Digital Low-IF Dual-PLL Doppler Radar System

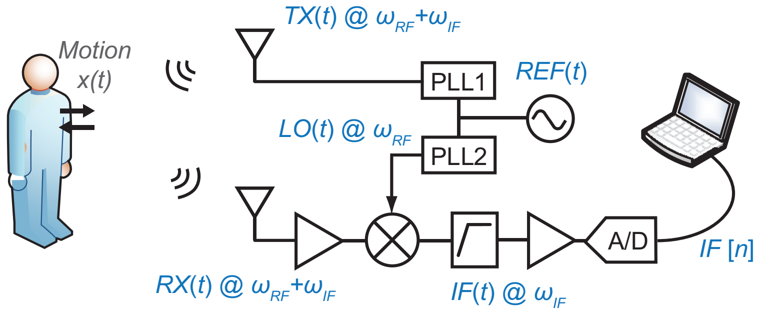

Figure 2.1: Block diagram of the Dual-PLL Doppler radar system.

Fig. 2.1 shows the block diagram of an IF Doppler radar system intended for vital sign monitoring applications. The transmitted signal $TX(t)$ is generated from a PLL-based synthesizer whose reference frequency is f_{REF}

$$TX(t) = A_0 \cos\left[2\pi f_{\mathrm{RF}} t + \phi_T(t)\right], \tag{2.1}$$

where A_0 is the amplitude of the signal, $\phi_T(t)$ represents the phase noise, and $f_{\mathrm{RF}} = N_{\mathrm{TX}} f_{\mathrm{REF}}$. Here, N_{TX} is the divider ratio for the synthesizer. Without affecting the result of the analysis, the fixed initial phase of the TX signal is omitted here for simplicity. The power level of the transmitted signal is denoted as P_{TX}.

The motion of the target modulates the phase of the TX signal and create a reflected signal $RX(t)$

$$RX(t) = A_0 P_L \cos\left[2\pi f_{\mathrm{RF}}\left(t - t_d\right) + \frac{4\pi x(t)}{\lambda} + \phi_T(t - t_d)\right], \tag{2.2}$$

where P_L is the round-trip path loss given by the radar range equation [62], $t_d = 2d/c$ represents the round-trip delay between the RX and TX signals, and $x(t)$ represents the target motion with a frequency of f_m. Here d is the nominal distance between the target and the radar transceiver, c is the speed of light, and $\lambda = c/f_{\mathrm{RF}}$ is the wavelength.

In the receiver, the local oscillator (LO) signal $LO(t)$ is generated by another PLL locked to the same reference as $TX(t)$

$$LO(t) = A_l \cos\left[2\pi f_{LO}\, t + \phi_L(t)\right], \tag{2.3}$$

where $f_{\mathrm{LO}} = N_{LO} f_{\mathrm{REF}} = f_{\mathrm{RF}} - f_{\mathrm{IF}}$, and $\phi_L(t)$ represents the phase noise of $LO(t)$. Here, N_{TX} is the divider ratio for the LO synthesizer and f_{IF} is the intermediate frequency.

The IF signal at the output of the receiver is then derived as

$$IF(t) = A_0 P_L G_{\mathrm{RX}} \cos\left[2\pi f_{\mathrm{IF}}\, t + \frac{4\pi x(t)}{\lambda} + \Delta\phi(t)\right], \tag{2.4}$$

where G_{RX} is the receiver gain and $\Delta\phi(t) = \phi_T(t - t_d) - \phi_L(t)$

This IF signal is then acquired using ADC and high-pass filtered, amplified, and then digitized for further processing. The block diagram of the digital signal processing algorithm is shown in Fig. 2.2. The digitized IF signal $IF[n]$ is first downconverted to baseband by quadrature mixing with the in-phase and quadrature-phase (I/Q) digital LO signals at ω_{IF}. Note that the sampling clock of the analog-to-digital converter (ADC) and the PLL clocks come from two incoherent sources in the current setup. As a result, a small frequency offset is added to the digital LO signals.

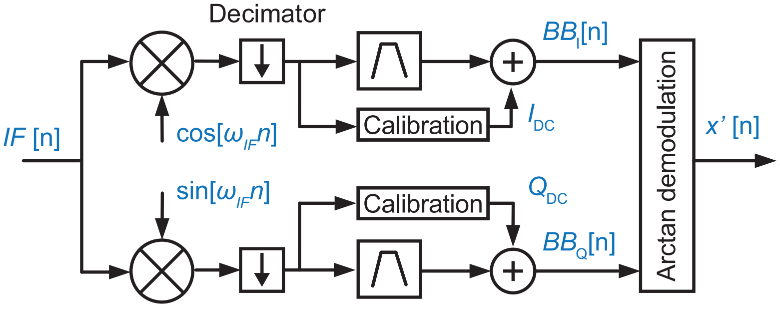

Figure 2.2: Block diagram of the digital signal processing algorithm

The output of the digital mixers are then decimated to a signal with lower sample rate for easier filtering implementation. Due to the imperfect frequency mismatch (sub-0.1 Hz), a bandpass filter with a pass band from 0.1 Hz to 3 Hz is required to eliminate the resulting noise and focus on signals of interests. Concurrently, the dc component of the baseband signals are extracted, calibrated and fed back to the baseband signals to preserve their phase information. After this correction, baseband in-phase and quadrature signals $BB_I[n]$ and $BB_Q[n]$ are now obtained. Arctangent demodulation can then be used to reconstruct the motion signal $x'[n]$ [32].

2.3 Validation of Phase Coherence

To demonstrate the feasibility and performance of the proposed architecture, we construct a proof-of-concept radar system using off-the-shelf components. A single printed circuit board (PCB) with two Texas Instruments (TI) LMX2594 ICs constitute the core of the system. Further details of the setup and measured results are discussed in this section.

In order to validate that the two PLLs are producing coherent output signals, an interferometric experiment is set up as shown in Fig. 2.3 (a). The two PLLs are programmed to output two 2.41-GHz signals from a common 100-MHz reference crystal oscillator. The output signal from PLL1 goes through a Telemakus TEP4000-5 digital phase shifter to sweep the phase from 0° to 360°. The output signal of PLL2 goes through an attenuator that compensates for the insertion loss created by the phase shifter. The two signals are then combined using a Mini-Circuits power combiner (mode# ZX10-2-42-S+) and the output power is observed in a Tektronix RSA3408A spectrum analyzer.

The measured combined power with respect to the phase difference is shown in Fig 2.3 (b). Here, the power is normalized to the input power to each branch of the power combiner inputs. The normalized power scale is limited from $-20\,\mathrm{dB}$ to $3\,\mathrm{dB}$ even though the theoretical value could reach negative infinity (in dB) when the two signals are out of phase. The measured result shows a similar trend as the theory and a minimum normalized output power of $-41.7\,\mathrm{dB}$ is observed when the phase shifter is set to 191.52°. Barring amplitude and phase error in the setup, such as the variable insertion loss of the phase shifter and the limited isolation from the power combiner, the measurement result clearly demonstrates the frequency and phase coherence between the two PLL output signals.

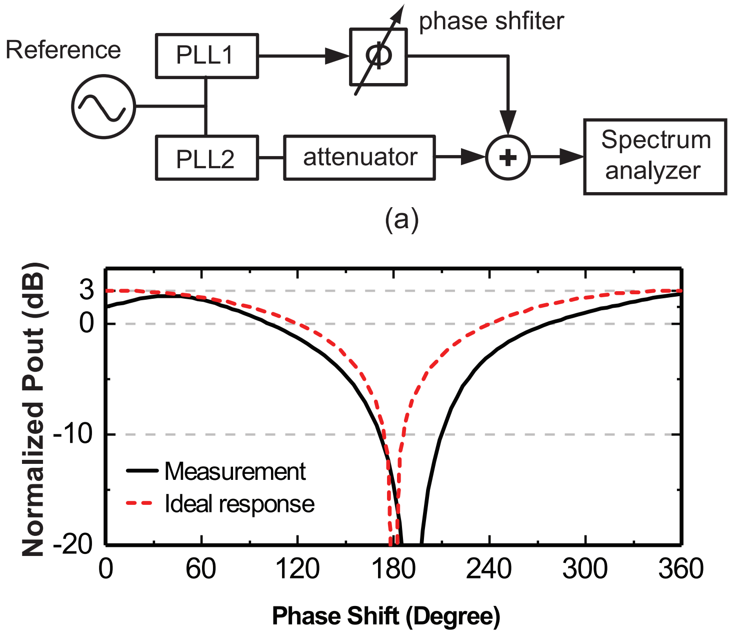

(a)

(b)

Figure 2.3: (a) Experimental setup for phase coherence validation. (b) Comparison between the measured and theoretical results of the normalized output power.

2.4 Single-Channel Prototype System Development

After validating the coherence of the two PLLs, the single-channel prototype system is developed using the modular PCB boards designed using commercial ICs. The constructed radar system is displayed in Fig. 2.4. The frequency for the TX and LO signals are set to 2.41 GHz+1 kHz and 2.41 GHz, respectively, resulting in an IF frequency of 1 kHz. The power of the TX signal is set at -6.5 dBm and the LO signal is set at 5 dBm to drive an Analog Devices ADL5365 passive mixer.

The receiver front-end low-noise amplifier is Mini-Circuits ZX60-272LN-S+ which provides 14.2-dB gain and 0.74-dB noise figure. The highpass filter consists of a series 0.1-μF capacitor and a parallel 100-$k\Omega$ resistor, providing a 3-dB cut-off frequency of 16 Hz. The two-stage differential input single-ended output IF amplifier provides 40-dB of gain to the 1-kHz IF signal which is then digitized at 50 ksps by a National Instruments USB-6002 data acquisition device. Further signal processing is carried out in the Matlab software.

In the experiment, the human subject sits at a distance of 1.8 meter facing the TX and RX antennas. The test subject wears finger-clipped pulse oximeter sensor to provide

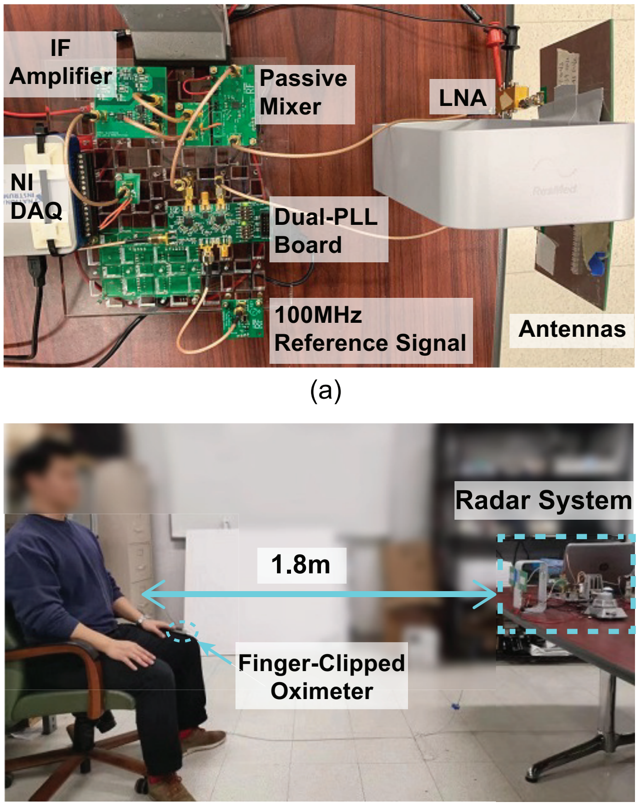

(a)

(b)

Figure 2.4: (a) Top view of the system setup for remote vital sign sensing. (b) Side view of the measurement setup.

the ground truth to the subject's heart rate. In a typical measurement, the nominal recording time is 120 s, although only 15-s post-processed time-domain data is shown in Fig.2.5. In these figures, BB_I, BB_Q, and normalized demodulated motion are shown. The comparison result with an pulse oximeter sensor is shown in Fig.2.6. where the frequency is in unit of beats per minute (BPM) and the spectrum is normalized based on its largest frequency component. In this specific experiment, the detected heartbeat rate is shown to be 67 BPM, which is the same with the result acquired by the oximeter sensor. Even though the measured spectrum has a limited frequency resolution, the comparison shows a very accurate result obtained by the proposed dual-PLL setup comparing with the oximeter reference.

In conclusion, the experimental validation of human vital sign measurement shows very good sensitivity at low output power. Specifically, the heart rate is clearly detected

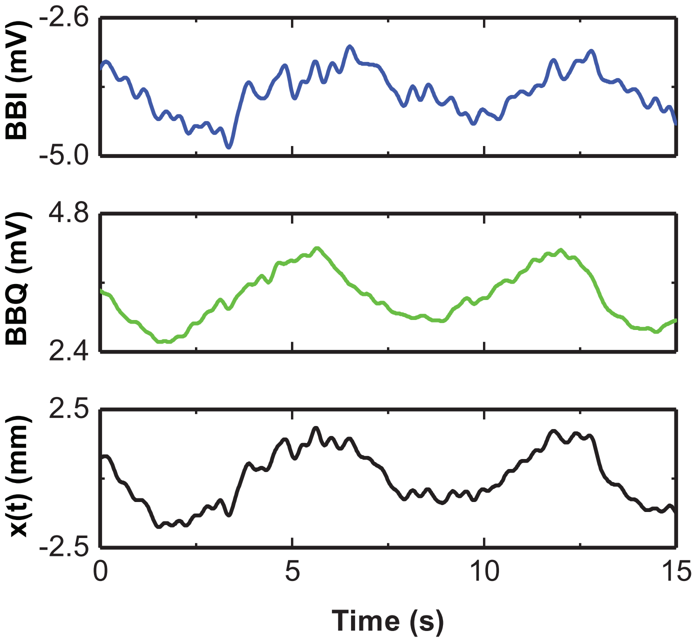

Figure 2.5: 15-second time domain signals for baseband I channel (BB_I), baseband Q channel (BB_Q) and the measured motion signal $x(t)$.

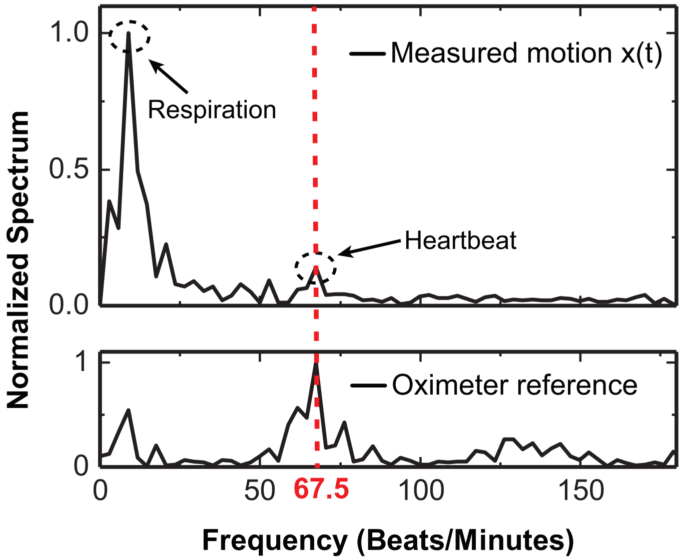

Figure 2.6: Normalized frequency spectrum of the detected motion signal $x(t)$ and the recorded reference signal from pulse oximeter sensor.

at a distance of 1.8-m with only −6.5-dBm transmitted power. The measured heartbeat rate agrees well with the pulse oximeter reading, which proves the effectiveness of the proposed single-channel Dual-PLL Low-IF radar design.

2.5 MIMO System Development

Due to the wide beam-width of the antenna radiation, all motions from multiple subjects can be captured to modulate the phase of the TX signal all together. However, in vital sign sensing, there are multiple sources of motion coming from different body parts of the subject including the random body motion from the subject's legs and hands as well as the desired heartbeat motion majorly induced by the chest of the subject. A single-channel system cannot boost the detection gain for one motion over the others. Benefiting from the phase coherence effect of sharing reference between the PLL ICs, a MIMO system can be achieved with distributing the same reference signal to the input of each radar module. By constructing a MIMO system, the formed narrow beam can accurately locates the chest areas of multiple targets which can significantly enhance the motion signal strength detected from the subject.

2.5.1 Compact Dual-PLL Module Design

To further improve the compactness of the Dual-PLL system design, all components are further integrated into three modular boards: the RX board, TX board and the control board. The RX and TX board are shown in Fig. 2.7 where the TX board in (a) consists of a ADF4351 PLL IC with its peripheral circuits. The same PLL design is also included in the RX board as shown in (b). Besides that, an ADL5365 passive mixer, QPL9057 LNA and AD8628 IF amplifier are also integrated onto the RX module. The control board is integrated with a Teensy 3.2 micro-controller which is used for programming PLL registers

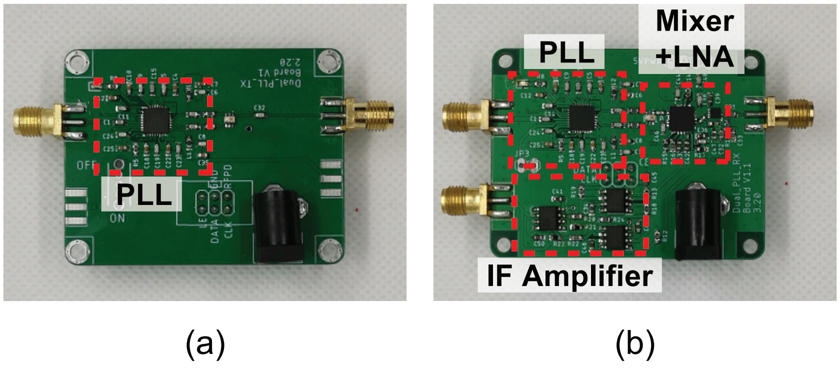

Figure 2.7: Photo of the compact Dual-PLL system module (a) TX board (b) RX board.

using the SPI protocol. All boards are powered through an AC-DC power adapter that can be plugged into the 110V outlet for generating a +6V DC supply. Furthermore, a ±2.5 DC voltage supply is generated on the control board using a switching regulator to serve as biases for the amplifier circuit.

2.5.2 6x6 MIMO System Design

In the setup, 6 RX boards and 6 TX boards are used to generate 12 RF signals. The frequency difference between the RX and TX board is 1KHz. Two baseboards are designed for splitting the reference signal and share it with all the PLL ICs on the modular boards to maintain RF signal phase coherence. A time duplex modulation (TDM) is applied for TX signal transmission in order to identify which TX the output channel is resulted from. Therefore, an FPGA is programmed to control the enable pin at each TX board to generate the TDM signal and make sure only one TX board is transmitting at a time. As a result, a total number 36 channels are created based on this setup.

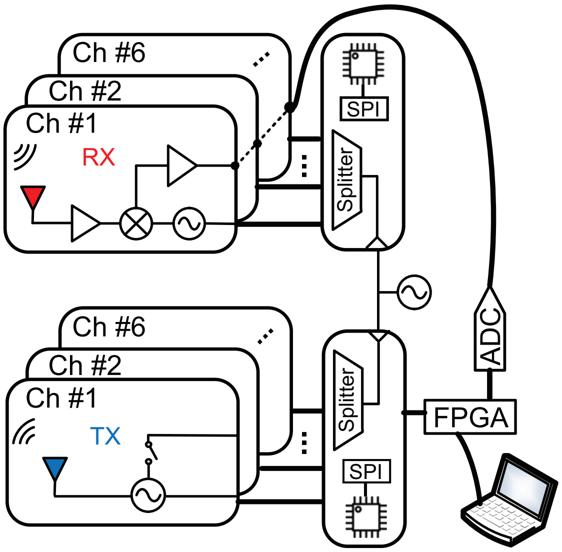

Figure 2.8: System diagram for the proposed dual-PLL based MIMO radar

The sampling of the 1kHz signal is done by using an FPGA controlled 16-bit AD7606 ADC. The 6 RX outputs are sampled simultaneously with a sampling frequency of 50 ksps. The data is first acquired in parallel but then merged into a single data stream for further transmission through an Ethernet cable. This process is done by adding labels based on the TDM control signal sent out by the FPGA. A label indicating which TX

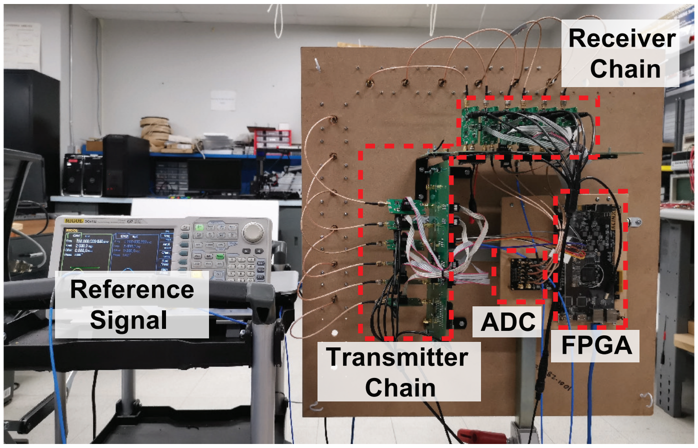

Figure 2.9: System setup for proposed dual-PLL based MIMO radar

operates at that moment is inserted at the beginning of each parallel sampled data stream and then the paralleled data can be put together to a series stream with the ability to be fully recovered. By inspecting the labels, the sampling data can be segmented and its correspondence to different transmitters and receivers can be identified accurately by signal processing inside the digital domain.

2.5.3 System Calibration

System calibration is a crucial step for the phased-array system to successfully form a coherent beam at any direction using all channels. Without calibration, the summation of all channel outputs do not add up constructively at the center due to the phase and amplitude deviation among the 36 output channels. This can be resulted from any difference in chip soldering, performance deviation in IC components and spatial locations of the antenna elements. Therefore, calibration needs to be performed to compensate for these phase and amplitude differences among all channels to ensure all signals share the same amplitude and add up constructively at the center location. Unlike the calibration performed for an FMCW system, the Doppler MIMO system requires a moving target for motion signal generation. Therefore, a linear stage actuator (LSTG) with a metal plate is placed at 2 meters away from the system. The physical setup is shown in Fig. 2.10(a). The moving target aligns with the center of the antenna array and it is programmed to

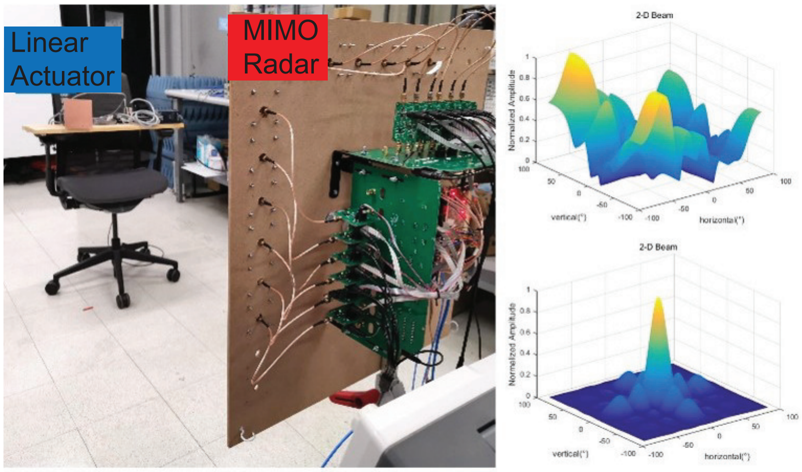

(a) (b)

Figure 2.10: System calibration setup for the proposed dual-PLL based MIMO radar

move in a sinusoidal waveform trajectory with a 0.5-cm amplitude at a 1.2-Hz frequency to generate a single-tone motion spectrum.

The calibration process is based on a 30-second data samples acquired from the system to obtain the phase and amplitude coefficients from the 36 output channels. The normalized power distribution across the azimuth and elevation directions respective to the geometric center of the antenna array are displayed in Fig. 2.10(b), where the top and bottom graphs show the spatial power distribution with and without the calibration process respectively. As shown in Fig. 2.10(b), the motion signal power is spread out randomly in all directions prior to the calibration process. Once the calibration is applied, the power distribution becomes more focused in one direction and added up constructively at the center location $(0^\circ, 0^\circ)$. This comparison demonstrates the effect of the calibration process as required for proper operation for the MIMO Doppler radar system.

2.5.4 Experiments

Three sets of experiments have been performed to evaluate the performance of the proposed MIMO radar prototype. In the first experiment, the accuracy of the measured beam direction is tested using a controlled LSTG as a reliable target motion. Followed by this, the multi-target vital sign detection performance using the MIMO radar is evaluated in the second and third experiments. During these experiments, multiple scenarios including sitting, standing and lying on a bed are conducted. In all vital signs detection setups, two respiration belts and finger-clipped pulse oximeter sensors are used to provide the ground truth data for the respiratory-rate and heart-rate information from the two subjects. Two male volunteers participated in these experiments. They are both in healthy conditions and do not have any respiratory or heart disease.

2.5.4.1 2-D Beam Forming Angle Detection Verification

The accuracy of the MIMO radar beam direction is measured in this experiment through the setup shown in Fig. 2.11, where the LSTG is placed at 9 different positions on the orthogonal plane that is 1.8 m away from the radar system. The distance information of all the target positions are labeled in Fig. 2.11. At each location of the target, the Doppler MIMO system operates for one minute to generate a set of data, which is then processed for the spatial power distribution plot with a step size of 1° across the entire space. The angle with the highest motion power is determined as the detected target angle, which is used to be compared with the theoretical angle calculated based on the physical distance of the measurement setup. The distance information, calculated angle positions as well as the measured angle position detected by the MIMO radar are listed in Tab. 2.1. After comparing between the calculated and the measured angles of the moving target, most of the deviations are within 1° whereas only 2 measurement results are 1.5° off from the calculated values. Therefore, the Doppler MIMO radar demonstrates a very accurate

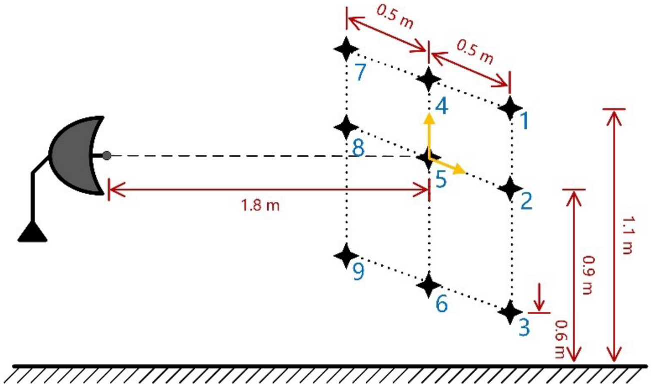

Figure 2.11: MIMO radar beam forming detection angle accuracy test

Table 2.1: Beam Forming Detection Angle Accuracy Test

Point Number	Position	Calculated Angle	Measured Angle
1	(0.5 m,0.2 m)	(15.5°, 6.3°)	(16°, 5°)
2	(0.5 m,0.0 m)	(15.5°, 0.0°)	(16°, 0°)
3	(0.5 m,-0.3 m)	(15.5°, -9.5°)	(16°, -10°)
4	(0.0 m,0.2 m)	(0.0°, 6.3°)	(1°, 6°)
5	(0.0 m,0.2 m)	(0.0°, 0.0°)	(0°, 1°)
6	(0.0 m,-0.3 m)	(0.0°, -0.3°)	(1°, -1°)
7	(-0.5 m,0.2 m)	(-15.5°, 6.3°)	(-15°, 5°)
8	(-0.5 m,0.0 m)	(-15.5°, 0.0°)	(-14°, 0°)
9	(-0.5 m,-0.3 m)	(-15.5°, -9.5°)	(-14°, -9°)

beam steering ability with an measurement error of less than 1.5° when comparing with the geometric angle respective to the center of the antenna array.

2.5.4.2 Chest Motion Allocation and Vital Signs Detection for Two Sitting Subjects

To test its multi-subject vital sign detection capability, two volunteers are asked to sit in front of the Doppler MIMO radar at different angles but the same radial distance, 1.8 m, away from the radar. The measurement setup is shown in Fig. 2.12 where the MIMO radar is installed on a tripod and the two subjects are sitting adjacently with 1 m apart. An Cartesian coordinate is set up with respective to the center of the antenna array where the x-y plane aligns with the antenna array plane. According to the coordinate setup, subject A is sitting at (0.5 m,-0.15 m) and B is sitting at (-0.5 m,-0.2 m). The distance information corresponds to A(15°, -5°) and B(-15°, -6°) as the detected angles expected at the 2-D spatial power distribution plot. In the experiment, two volunteers are instructed to breathe normally for one and a half minutes and 45 seconds of data are used for the final signal processing.

The detection results are displayed in Fig. 2.14 where (a) is the spatial power distribution plot and the rest of the subplots represent the detected vital sign signals in either

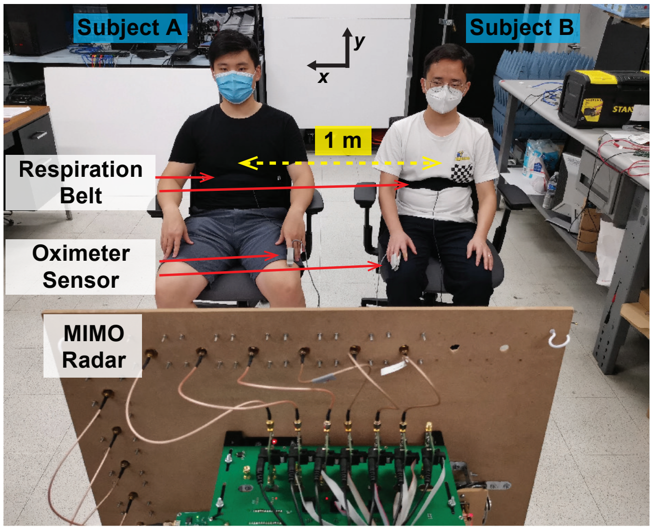

Figure 2.12: Vital-sign measurement setup for two subjects sitting next to each other

time or frequency domain. In Fig. 2.14 (a), the measured motion powers are displayed to be focused onto the chest area of the human subject where the highest motion sensitivity points are determined to be A(17°,-5°) and B(-13°,-7°). The measurement results show good agreement with the theoretical predictions. To improve the detection sensitivity, the most sensitive beam position is found for the two subjects respectively with their time-domain waveform shown in (b) and (e). To further detect the respiration rate and the heart rate from the two subjects, FFT is adopted to result in frequency domain plots as shown in (c), (d), (f) and (g) with different frequency limits. To compare with the ground truth reference, the vital sign rate measured by the oximeter sensor and the respiration belt is overlaid on top of the FFT plot. For subject A, the respiration rate is detected to be 0.1 Hz which agrees with the respiration belt measurement and its 1.05-Hz detected heart rate result also aligns with the oximeter reading. Meanwhile, the vital sign results for subject B are also detected at the same time. The 0.15-Hz respiration rate and 0.98-Hz heart rate are both detected and agreed with the ground truth measurements.

2.5.4.3 Chest Motion Allocation and Vital Signs Detection for Two lying Subjects

In the third experiment, the radar system is tested under a more realistic scenario where the radar is hung above a foam board bed with two volunteers lying on top of it. The foam board has a dimension of 1.8 m wide and 2.4 m long. The radar system is placed 1.9 m away from the bed and the two volunteers on the bed are separated by 0.8 m. With considering the physical dimensions of the subjects' position, A(15°, -15°) and B(-10°, 10°) are identified with respective to the geometric center of the antenna placement. After the subjects are in place, the system is turned on for data recording for 45 s.

After data processing, the measurement results are shown in Fig. 2.15 where Fig. 2.15 (a) clearly identifies the measured motion powers from the chest area of the two test subjects with A(15°, -15°) and B(-10°, -9°) detected. The measured detection angle results agree very well with the theoretical predictions. The detected time-domain vital sign signals are shown in (b) and (e) for subject A and B respectively. To further detect the respiration rate and the heart rate from the two subjects, (c), (d), (f) and (g) are processed with with different frequency limits. For subject A, the respiration rate is detected to be 0.15 Hz which agrees with the respiration belt measurement and its 1.08-Hz detected heart rate result also aligns with the oximeter reading. Meanwhile, the vital sign results for subject B are also detected at the same time. The 0.22-Hz respiration rate and 1.15-Hz heart rate are both detected and agreed with the ground truth measurements.

Finally, the spatial resolution has been tested with two subjects lying on the bed shoulder to shoulder. The vital sign signal for two subjects are trying to be detected with changing the spacing between the two subjects (measured between center of their chests). A table with recorded separation distances and the detection results are listed in Tab. 2.2. Based on these results, the radar can always detect the vital signs from the two subjects until their separation goes down below 0.6 m. This indicates a measured spatial resolution of 18° from the Doppler MIMO radar.

2.6 Summary

This chapter presents the system development for both a single-channel and a 6x6 MIMO prototype systems using Dual-PLL low-IF system architecture. The effectiveness of sharing reference between different PLL ICs has been validated for maintaining phase coherence for the generated RF waveform. The RF module designs have been shown to increase

Table 2.2: Spatial Resolution Measurement

Distance (m)	**Calculated Angle**	**Detection Result (Y/N)**
0.8	24°	Y
0.7	21°	Y
0.6	18°	Y
0.5	15°	N

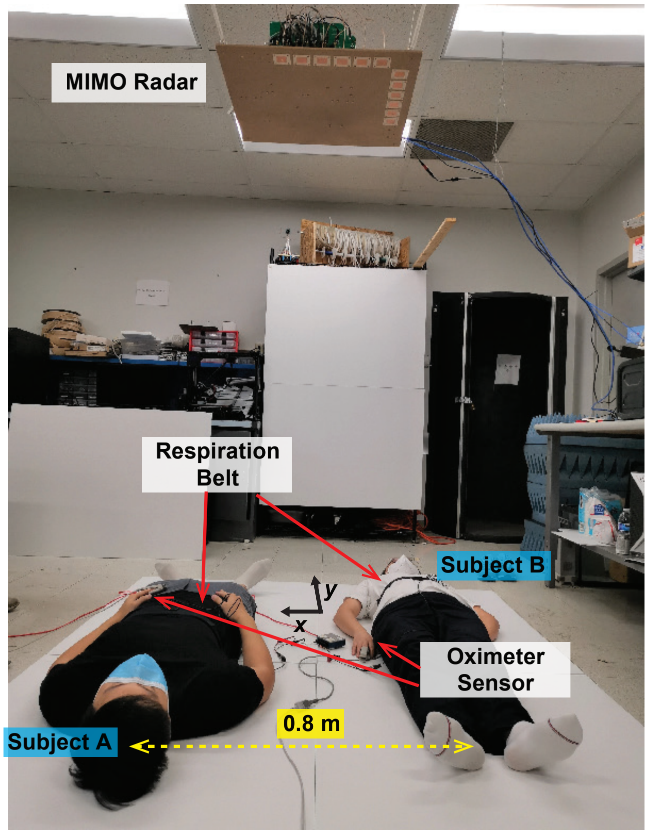

Figure 2.13: Vital-sign measurement setup for two subjects lying down with opposite direction next to each other

the compactness of the system development.

As for the performance of the proposed compact prototype system, the single-channel system successfully achieves a 1.8-m vital-sign detection with using −6.5 dBm transmitted power. The MIMO radar demonstrates a superior performance in chest allocation for improved detection sensitivity in vital detection. The system successfully detects both the heart rate and the respiration rate of the two human subjects in 1.9 meters away. Due to the limited channel numbers of the MIMO system, the system is shown to successfully distinguish the vital sign detected from two subjects if their separation distance is more than 18^o respective to the radar center position.

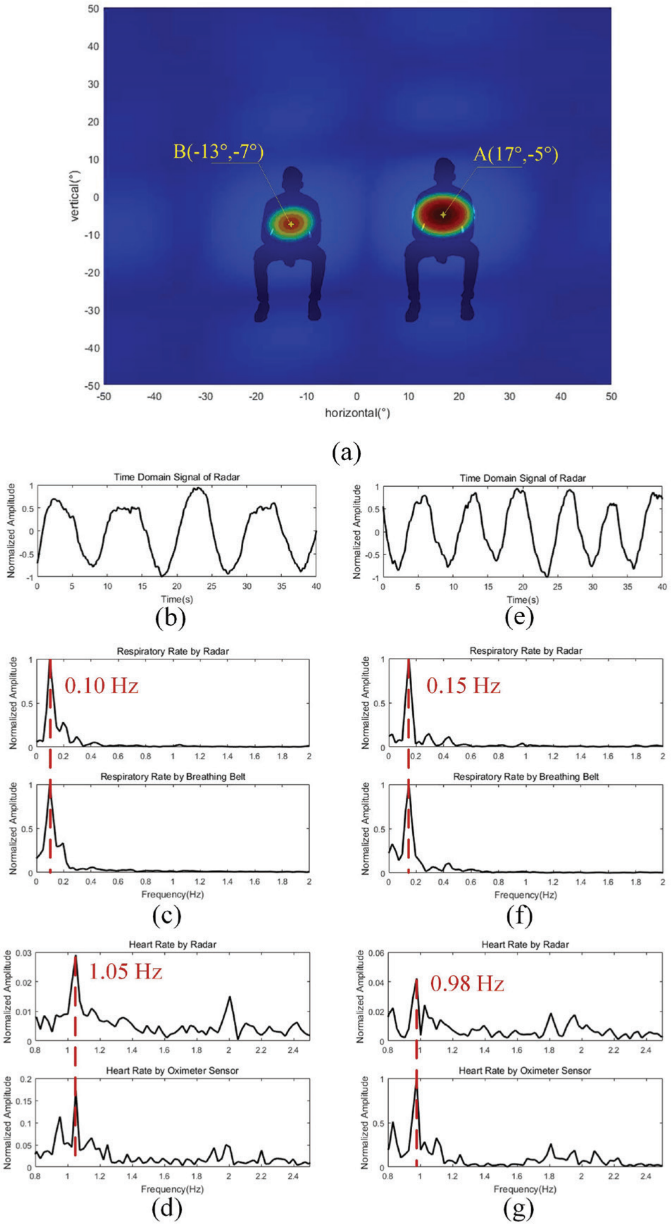

(a)

(b) (e)

(c) (f)

(d) (g)

Figure 2.14: Measurement Results for two subjects sitting next to each other (a) Spatial power distribution plot with steering beam across the 2-D plane (b) Time-domain signal result processed for subject A (c) Frequency domain result between 0 and 2 Hz for subject A (d) Frequency domain result between 0.8 Hz and 2.5 Hz for subject A (e) Time-domain signal result processed for subject B (f) Frequency domain result between 0 and 2 Hz for subject B (g) Frequency domain result between 0.8 Hz and 2.5 Hz for subject B.

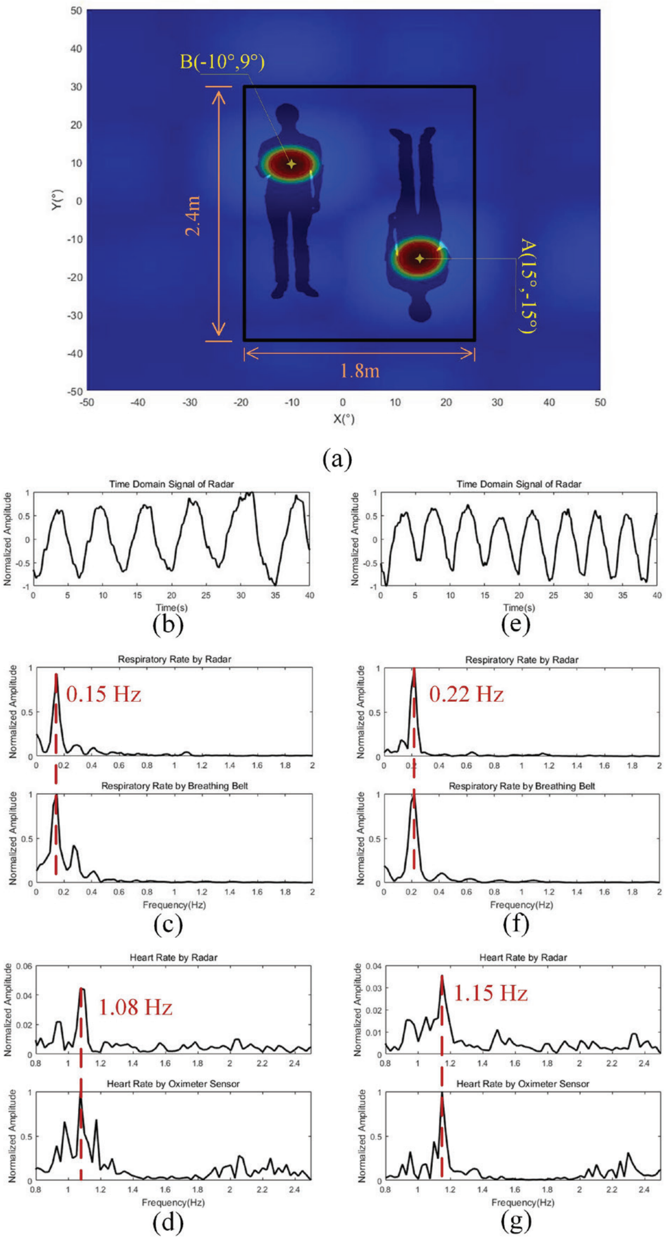

Figure 2.15: Measurement Results for two subjects lying on the bed next to each other (a) Spatial power distribution plot with steering beam across the 2-D plane (b) Time-domain signal result processed for subject A (c) Frequency domain result between 0 and 2 Hz for subject A (d) Frequency domain result between 0.8 Hz and 2.5 Hz for subject A (e) Time-domain signal result processed for subject B (f) Frequency domain result between 0 and 2 Hz for subject B (g) Frequency domain result between 0.8 Hz and 2.5 Hz for subject B.

Chapter 3

Coupling Effect to SNR in Dual-PLL IF System

3.1 Introduction

IF systems take advantages of digital signal processing and avoids issues that are commonly experienced in DC Doppler systems such as local oscillator (LO) leakage, dc offset, and I/Q mismatch. In an IF system, the generation of the baseband IF usually requires an additional coherent signal source. In some IF systems, the second RF signal is generated by mixing the RF and IF using an in-phase quadrature (I/Q) mixer [22, 63]. This guarantees the phase coherence between the two RF signals but attention needs to be paid to any possible I/Q imbalance in the system. The systems presented in [21, 23, 24] use two RF sources sharing with the same reference to create the two coherent RF signals in order to avoid the I/Q imbalance issue. Among them, Gu et al. [21] used lab-grade measurement instrument to demonstrate the feasibility of the system architecture. Systems with more compact designs were developed in [21, 24]. Despite the difference in system design, the measurement performances were similar in these works, showing an approximately 3-m detection distance reported from [22, 23] with a transmitting power between $-13\,\text{dBm}$ and $-10\,\text{dBm}$. Although these studies have achieved good detection sensitivities, the noise analysis has not been discussed in detail for the dual-PLL IF system.

This chapter is motivated to analyze the different noise contributions within the system and identify the coupling effect to the SNR levels. In the end, an effective technique for improving the system SNR is proposed and validated through experiments.

3.2 Noise Analysis

As the received radar signal goes through the receiver, it is subject to the amplitude noise of the receiver circuits as well as the residual phase noise after mixing. Because vital sign signals such as respiration and heartbeat are usually very low in frequency (0.1–10 Hz), the residual phase noise should not be neglected since the phase noise at very low offset frequency can be significant. As such, the TX-RX leakage should also be taken into account because the leakage signal can also mix with the LO signal to introduce additional residual phase noise. This section presents a detailed noise analysis where the RF components, such as the antenna, the low-noise amplifier (LNA), and the mixer, as well as the IF components, such as the IF amplifier and the analog-to-digital converter (ADC), are considered.

3.2.1 Amplitude Noise

The amplitude noise in the radar receiver is comprised of the amplitude noise from the RF components, the thermal noise from the IF amplifier, and the ADC noise including the quantization noise and the thermal noise. Among them, the RF-domain amplitude noise can be quantified using the well-known Friis' formula. The noise spectral density (NSD) of the RF-domain amplitude noise at the IF output of the receiver is

$$S_{\mathrm{RFN}}(\mathrm{dBm/Hz}) = 10\log(kT) + G_{\mathrm{RX}} + NF, \tag{3.1}$$

where $k = 1.38 \times 10^{-23}$ J/K is the Boltzmann's constant and T is the temperature of the antenna in degrees Kelvin (K). $G_{\mathrm{RX}} = G_{\mathrm{LNA}} + G_{\mathrm{mixer}} + G_{\mathrm{IF}}$, where G_{LNA}, G_{mixer}, and G_{IF} are the gain in dB of the LNA, mixer, and the IF amplifier, respectively. NF is the total noise figure of receiver in dB.

It should be noted that S_{RFN} in (3.1) is calculated with a matched load presented to the IF output, as shown in Fig. 3.1 (a). When a typical noise source of amplitude V_{RFN} and source impedance $R = 50$ ohm is used as the noise model of the RX front-end. V_{RFN} can be derived as

$$V_{\mathrm{RFN}}(\mathrm{V}/\sqrt{\mathrm{Hz}}) = \sqrt{8RS_{\mathrm{RFN}}}. \tag{3.2}$$

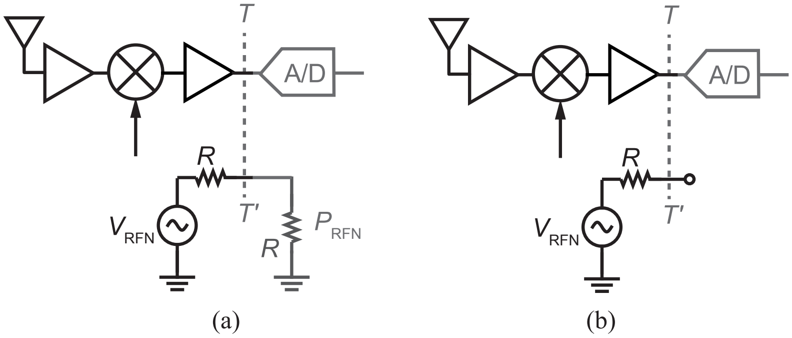

Figure 3.1: Noise modeling at the interface between IF amplifier and ADC. (a) Friis' equation to calculate P_{RFN} with a reference of a matched load connecting at the IF output. (b) An open node exists between IF amplifier and ADC due to the high input impedance of ADC.

In practice, as shown in Fig. 3.1 (b), the ADC as well as its driver amplifiers usually presents a high impedance to the output of the IF amplifier. When the IF amplifier and the ADC are conneted directly, the noise source voltage V_{RFN} is presented to the ADC as an added input noise, which generates a NSD of $8S_{\mathrm{RFN}}$ (dBm/Hz) at the ADC output.

The ADC introduces quantization noise and thermal noise as well. Generally, the ADC noise behavior can be characterized by the term full-scale system noise voltage $e_{\mathrm{n,ADC}}$ [64], corresponding to a NSD of

$$S_{\mathrm{n,ADC}}(\mathrm{dBm/Hz}) = \frac{e^2_{\mathrm{n,ADC}}}{R}\frac{2}{f_s}, \tag{3.3}$$

where f_s is the sampling frequency. As a result, the total NSD of amplitude noise at the ADC output is

$$S_{\mathrm{AM}}(\mathrm{dBm/Hz}) = 8S_{\mathrm{RFN}} + S_{\mathrm{n,ADC}}. \tag{3.4}$$

3.2.2 Residual Phase Noise

The residual phase noise at the mixer output is defined as the remaining phase noise of the mixing product between the two RF signal and the LO signal. If RF signal and the LO signal are coherent in a Doppler radar system, the range-correlation effect can significantly suppress the residual phase noise in the received baseband/IF signal. For example, more than 136-dB reduction in the residual phase noise is obtained due to the range-correlation effect [18].

For the dual-PLL Doppler radar system of Fig. 2.1, the same reference source $REF(t)$ is used for the TX and RX PLLs. The phase noise of the TX and LO signals can be expressed as

$$\phi_T(t) = \frac{f_{\mathrm{RF}}}{f_{REF}}\phi_{\mathrm{REF}}(t) + \phi_{\mathrm{PLL1}}(t), \tag{3.5a}$$

$$\phi_L(t) = \frac{f_{\mathrm{LO}}}{f_{\mathrm{REF}}}\phi_{\mathrm{REF}}(t) + \phi_{\mathrm{PLL2}}(t), \tag{3.5b}$$

respectively. Here, $\phi_{\mathrm{REF}}(t)$ is the phase noise of the reference signal of the PLL, $\phi_{\mathrm{PLL1}}(t)$ and $\phi_{\mathrm{PLL2}}(t)$ are the uncorrelated phase noise of the two PLLs. The uncorrelated noises are mainly contributed by the VCO phase noise and the flicker noise from the phase detector [65]. Due to the high-pass noise filtering feature of the PLL, the closed-loop VCO phase noise is greatly suppressed at the low offset frequency. Consequently, the PLL flicker noise, which has a typical $1/f$ behavior at low offset frequencies, acts as the major contributor to the uncorrelated phase noise in the proposed low-IF system.

According to (2.4), the residual phase noise at the mixer output can be obtained as

$$\begin{aligned}\Delta\phi_1(t) &= \phi_T(t - t_d) - \phi_L(t) \\ &= \phi_{\mathrm{corr1}}(t) + \phi_{\mathrm{uncorr1}}(t),\end{aligned} \tag{3.6}$$

where,

$$\phi_{\mathrm{corr1}}(t) = \frac{f_{\mathrm{RF}}}{f_{\mathrm{REF}}}\phi_{\mathrm{ref}}(t - t_d) - \frac{f_{\mathrm{LO}}}{f_{\mathrm{REF}}}\phi_{\mathrm{REF}}(t), \tag{3.7a}$$

$$\phi_{\mathrm{uncorr1}}(t) = \phi_{\mathrm{PLL1}}(t - t_d) - \phi_{\mathrm{PLL2}}(t). \tag{3.7b}$$

Here, the residual phase noise $\Delta\phi_1(t)$ is the combination of $\phi_{\mathrm{corr1}}(t)$ and $\phi_{\mathrm{uncorr1}}(t)$. $\phi_{\mathrm{corr1}}(t)$ can be greatly suppressed by the range-correlation effect. For the short-range detection ($t_d \approx 0$) of a low-IF radar ($f_{\mathrm{LO}} = f_{\mathrm{RF}} - f_{\mathrm{IF}} \approx f_{\mathrm{RF}}$), an approximately full-cancellation of the correlated phase noise can be achieved, which significantly reduces the residual phase noise.

The IF signal of (2.4) contains the motion information of $x(t)$, the IF frequency term of f_{IF}, and the phase noise $\Delta\phi_1(t)$. To simplify the analysis without loss of generality, the motion displacement, $x(t)$, is assumed to be sinusoidal

$$x(t) = x_{\mathrm{p}}\sin(2\pi f_m t), \tag{3.8}$$

where x_p is the maximum motion magnitude and f_m is the frequency of the motion displacement.

To obtain the power spectral density (PSD) of $V_{\text{IF1}}(t)$, the autocorrelation function, $\mathcal{R}_{\text{IF1}}(\tau)$, can be derived as

$$\begin{aligned}\mathcal{R}_{\text{IF1}}(\tau) =& \mathcal{E}\{V^*_{\text{IF1}}(t)V_{\text{IF1}}(t+\tau)\} \\ =& P_{\text{IF1}}R\cos(2\pi f_{\text{IF}}\tau) - P_{\text{IF1}}R\cos(2\pi f_{\text{IF}}\tau)\mathcal{R}_{\phi_{\text{m}}}(\tau) \\ & - P_{\text{IF1}}R\cos(2\pi f_{\text{IF}}\tau)\mathcal{R}_{\Delta\phi_1}(\tau),\end{aligned} \tag{3.9}$$

where $\mathcal{E}\{\}$ refers to the expected value of the function of interests. $\mathcal{R}_{\Delta\phi_{\text{m}}}(\tau)$ and $R_{\Delta\phi_1}(\tau)$ are the autocorrelation function of $\Delta\phi_{\text{m}}(t)$ and $\Delta\phi_1(t)$, respectively:

$$\begin{aligned}\mathcal{R}_{\Delta\phi_{\text{m}}}(\tau) &= \left(\frac{4\pi x_P}{\lambda}\right)^2\frac{1}{2}\cos(2\pi f_m\tau), \\ \mathcal{R}_{\Delta\phi_1}(\tau) &= \left(\frac{f_{\text{RF}}}{f_{\text{REF}}}\right)^2\mathcal{R}_{\phi_{\text{REF}}}(\tau) \\ &\quad - \frac{f_{\text{RF}}f_{\text{LO}}}{f^2_{\text{REF}}}\left[\mathcal{R}_{\phi_{\text{REF}}}(\tau - t_d) + \mathcal{R}_{\phi_{\text{REF}}}(\tau + t_d)\right] \\ &\quad + \mathcal{R}_{\text{PLL1}}(\tau) + \mathcal{R}_{\text{PLL2}}(\tau).\end{aligned} \tag{3.10}$$

The PSD of $V_{\text{IF1}}(t)$, $\mathcal{S}_{\text{IF1}}(f)$ (V^2/Hz), with reference to the system impedance R, can be obtained by taking the Fourier transform of $R_{\text{IF1,IF1}}(\tau)$. Then it can be converted from V^2/Hz to dBm/Hz by dividing the reference impedance R.

$$\mathcal{S}_{\text{IF1}}(f)(\text{dBm/Hz}) = \mathcal{F}\{\mathcal{R}_{\text{IF1}}(\tau)\}\frac{1}{R}. \tag{3.11}$$

Taking (3.9) and (3.10) into (3.11), the explicit expression of $\mathcal{S}_{\text{IF1}}(f)$ can be derived as:

$$\begin{aligned}\mathcal{S}_{\text{IF1}}(f) =& P_{\text{IF1}}\left[\frac{1}{2}\delta(f - f_{\text{IF}}) + \frac{1}{2}\delta(f + f_{\text{IF}})\right] - P_{\text{IF1}}\left[\frac{1}{2}\delta(f - f_{\text{IF}}) + \frac{1}{2}\delta(f + f_{\text{IF}})\right] * \mathcal{S}_{\phi_{\text{m}}}(f) \\ & - P_{\text{IF1}}\left[\frac{1}{2}\delta(f - f_{\text{IF}}) + \frac{1}{2}\delta(f + f_{\text{IF}})\right] * \mathcal{S}_{\Delta\phi_1}(f).\end{aligned} \tag{3.12}$$

where the symbol $*$ denotes convolution. The convolution with $\delta(f - f_{\text{IF}})$ and $\delta(f + f_{\text{IF}})$ translates the PSD spectrum so that it is centered at f_{IF} and $-f_{\text{IF}}$, respectively. In the following analysis, this convolution will be dropped with the tacit assumption that the

PSD is centered at f_{IF}. Besides, the PSD centered at f_{IF} and $-f_{\mathrm{IF}}$ are symmetrical and thus only the PSD centered at f_{IF} is given for simplicity. As such, $\mathcal{S}_{\mathrm{IF1}}(f)$ can be re-written as

$$\mathcal{S}_{\mathrm{IF1}}(f) = \frac{P_{\mathrm{IF1}}}{2}\left[\delta(f) - \mathcal{S}_{\phi_{\mathrm{m}}}(f) - \mathcal{S}_{\Delta\phi_1}(f)\right], \tag{3.13}$$

where

$$\mathcal{S}_{\phi_{\mathrm{m}}}(f) = \left(\frac{4\pi x_p}{\lambda}\right)^2 \frac{1}{4}\delta(f - f_m), \tag{3.14a}$$

$$\mathcal{S}_{\Delta\phi_1}(f) = \mathcal{S}_{\mathrm{corr1}}(f) + \mathcal{S}_{\mathrm{uncorr1}}(f), \tag{3.14b}$$

$$\mathcal{S}_{\mathrm{corr1}}(f) = \mathcal{S}_{\phi_{\mathrm{REF}}}(f) \times \left[\left(\frac{f_{\mathrm{IF}}}{f_{\mathrm{REF}}}\right)^2 + \left(\frac{f_{\mathrm{RF}} f_{\mathrm{LO}}}{f_{\mathrm{REF}}^2}\right) 4\sin^2(2\pi f t_d)\right], \tag{3.14c}$$

$$\mathcal{S}_{\mathrm{uncorr1}}(f) = \mathcal{S}_{\mathrm{PLL1}}(f) + S_{\mathrm{PLL2}}(f) \approx 2S_{\mathrm{PLL}}(f). \tag{3.14d}$$

It can be observed that the phase noise of the IF signal, $\mathcal{S}_{\Delta\phi_1}(f)$, is a combination of the correlated and uncorrelated parts. The correlated residual phase noise, $\mathcal{S}_{\mathrm{corr1}}(f)$, comes from the shared reference signal and is significantly suppressed in noise level with the help of frequency scaling and the range-correlation effect. On the other hand, the uncorrelated residual phase noise, $S_{\mathrm{uncorr1}}(f)$, is caused by the combined phase noise contribution from two RF inputs at the offset frequency f. Further approximation is made in (3.14d) where the same PLL IC model is used for both TX and LO signal generation, i.e. $\mathcal{S}_{\mathrm{PLL1}}(f) \approx \mathcal{S}_{\mathrm{PLL2}}(f) \approx \mathcal{S}_{\mathrm{PLL}}(f)$.

Considering both the amplitude noise and the residual phase noise, the RX SNR equation at the motion signal frequency f_m can be obtained as

$$\mathrm{SNR} = \frac{\left(\frac{4\pi x_p}{\lambda}\right)^2 \frac{P_{\mathrm{IF1}}}{4}}{S_{\mathrm{AM}} + S_{\Delta\phi_1}(f_m) P_{\mathrm{IF1}}}. \tag{3.15}$$

3.2.3 Interference from TX-RX Leakage

In a practical mono-static Doppler radar system, there is a finite coupling/leakage between the transmitter and the receiver due to the antenna mutual coupling, the parasitic coupling through the circuit substrate, and the packages. Although this TX-RX leakage signal does not result in a receiver output at the same frequency with the motion signal when mixed with the LO signal, its residual phase noise must be considered when the motion signal is very weak.

For simplicity, the TX-RX leakage signal is modeled as a delayed version of the TX signal

$$\begin{aligned} V_c(t) &= \sqrt{G_{\mathrm{C}}} V_{\mathrm{TX}}(t - t_c) \\ &= \sqrt{2 G_{\mathrm{C}} P_{\mathrm{T}} R} \cos\left[2\pi f_{\mathrm{RF}} t + \phi_c + \phi_{\mathrm{T}}(t - t_c)\right], \end{aligned} \tag{3.16}$$

where G_{C} is the coupling/leakage coefficient defined as the power ratio between the leakage signal and the TX signal, t_c is the equivalent time delay of the leakage signal, and $\phi_c = 2\pi f_{\mathrm{RF}} t_c$ is the phase shift due to the delay t_c. ϕ_c is neglected in the following analysis since it has no effect on the SNR behavior.

The leakage signal $V_c(t)$ combines with the receiver signal $V_{\mathrm{RX}}(t)$ at the receiver front-end, and generates an additional component to the IF signal

$$V_{\mathrm{IFc}}(t) = \sqrt{2 P_{\mathrm{IFc}} R} \cos\left[2\pi f_{\mathrm{IF}}\, t + \Delta\phi_c(t)\right], \tag{3.17}$$

where $P_{\mathrm{IFc}} = G_{\mathrm{RX}} G_{\mathrm{C}} P_T$ and $\Delta\phi_c(t) = \phi_T(t - t_c) - \phi_L(t)$ is the corresponding residual phase noise due to the TX-RX leakage. Besides, similar to $\Delta\phi_1(t)$ of (3.6), $\Delta\phi_c(t)$ can be obtained as

$$\begin{aligned} \Delta\phi_c(t) &= \phi_T(t - t_c) - \phi_L(t) \\ &= \phi_{\mathrm{corr,c}}(t) + \phi_{\mathrm{uncorr,c}}(t), \end{aligned} \tag{3.18}$$

where,

$$\phi_{\mathrm{corr,c}}(t) = \frac{f_{\mathrm{RF}}}{f_{\mathrm{REF}}} \phi_{\mathrm{ref}}(t - t_c) - \frac{f_{\mathrm{LO}}}{f_{\mathrm{REF}}} \phi_{\mathrm{REF}}(t), \tag{3.19a}$$

$$\phi_{\mathrm{uncorr,c}}(t) = \phi_{\mathrm{PLL1}}(t - t_c) - \phi_{\mathrm{PLL2}}(t). \tag{3.19b}$$

When the TX-RX leakage is considered, the IF signal $V_{\mathrm{IF}}(t)$ is a linear combination of $V_{\mathrm{IF1}}(t)$ and $V_{\mathrm{IFc}}(t)$,

$$V_{\mathrm{IF}}(t) = V_{IF1}(t) + V_{\mathrm{IFc}}(t). \tag{3.20}$$

The autocorrelation function of $V_{\mathrm{IF}}(t)$ can be derived as

$$\mathcal{R}_{\mathrm{IF}}(\tau) = \mathcal{R}_{\mathrm{IF1}}(\tau) + 2\mathcal{R}_{\mathrm{IF1,IFc}}(\tau) + \mathcal{R}_{\mathrm{IFc}}(\tau), \tag{3.21}$$

where $\mathcal{R}_{\mathrm{IF1,IFc}}(\tau)$ is the autocorrelation between $V_{\mathrm{IF1}}(t)$ and $V_{\mathrm{IFc}}(t)$, as expressed

$$\begin{aligned}\mathcal{R}_{\mathrm{IF1,IFc}}(\tau) =&\sqrt{P_{\mathrm{IF1}}P_{\mathrm{IFc}}}R\left[\cos\left(2\pi f_{\mathrm{IF}}\tau\right)+\cos\left(2\pi f_{\mathrm{IF}}\tau\right)\mathcal{R}_{\Delta\phi_1,\Delta\phi_{\mathrm{c}}}(\tau)\right],\\ \mathcal{R}_{\Delta\phi_1,\Delta\phi_{\mathrm{c}}}(\tau) =&\left(\frac{f_{\mathrm{RF}}}{f_{\mathrm{REF}}}\right)^2\mathcal{R}_{\mathrm{REF}}(\tau+t_d-t_c)-\frac{f_{\mathrm{RF}}f_{\mathrm{LO}}}{f_{\mathrm{REF}}^2}\mathcal{R}_{\mathrm{REF}}(\tau+t_d)\\ &-\frac{f_{\mathrm{RF}}f_{\mathrm{LO}}}{f_{\mathrm{REF}}^2}\mathcal{R}_{\mathrm{REF}}(\tau-t_c)+\left(\frac{f_{\mathrm{LO}}}{f_{\mathrm{REF}}}\right)^2\mathcal{R}_{\mathrm{REF}}(\tau)\\ &+\mathcal{R}_{\mathrm{PLL1}}(\tau+t_d-t_c)+\mathcal{R}_{\mathrm{PLL1}}(\tau).\end{aligned} \tag{3.22}$$

Similarly, the PSD of $V_{\mathrm{IF}}(t)$, $\mathcal{S}_{\mathrm{IF}}(f)$, can be obtained as

$$\begin{aligned}\mathcal{S}_{\mathrm{IF}}(f)(\mathrm{dBm/Hz}) &= \mathcal{F}\{\mathcal{R}_{\mathrm{IF}}(\tau)\}\frac{1}{R}\\ &= \mathcal{S}_{\mathrm{IF1}}(f)+2\mathcal{S}_{\mathrm{IF1,IFc}}(f)+\mathcal{S}_{\mathrm{IFc}}(f),\end{aligned} \tag{3.23}$$

where $\mathcal{S}_{\mathrm{IF1}}(f)$ is the PSD of $V_{\mathrm{IF1}}(t)$ as given in (3.13), $\mathcal{S}_{\mathrm{IF1,IFc}}(f)=\mathcal{F}\{\mathcal{R}_{\mathrm{IF1,IFc}}(\tau)\}/R$ in (3.24), and $\mathcal{S}_{\mathrm{IFc}}(f)$ is the PSD of $V_{\mathrm{IFc}}(t)$ in (3.26), as shown bellow.

$$\mathcal{S}_{\mathrm{IF1,IFc}}(f) = \sqrt{P_{\mathrm{IF1}}P_{\mathrm{IFc}}}\left[\frac{1}{2}\delta(f)+\frac{1}{2}\mathcal{S}_{\Delta\phi_1,\Delta\phi_{\mathrm{m}}}(f)\right], \tag{3.24}$$

where

$$\begin{aligned}\mathcal{S}_{\Delta\phi_1,\Delta\phi_{\mathrm{m}}}(f) = \mathcal{S}_{\phi_{\mathrm{REF}}}(f)&\left[\left(\frac{f_{\mathrm{RF}}}{f_{\mathrm{REF}}}\right)^2 e^{j2\pi f(t_d-t_c)}-\frac{f_{\mathrm{RF}}f_{\mathrm{LO}}}{f_{\mathrm{REF}}^2}e^{j2\pi f t_d}-\frac{f_{\mathrm{RF}}f_{\mathrm{LO}}}{f_{\mathrm{REF}}^2}e^{-j2\pi f t_c}+\left(\frac{f_{\mathrm{LO}}}{f_{\mathrm{REF}}}\right)^2\right]\\ &+e^{j2\pi f(t_d-t_c)}\mathcal{S}_{\mathrm{PLL1}}(f)+\mathcal{S}_{\mathrm{PLL2}}(f).\end{aligned} \tag{3.25}$$

$$\mathcal{S}_{\mathrm{IFc}}(f) = \frac{P_{\mathrm{IFc}}}{2}\left[\delta(f)-\mathcal{S}_{\Delta\phi_{\mathrm{c}}}(f)\right], \tag{3.26}$$

where

$$\mathcal{S}_{\Delta\phi_{\mathrm{c}}}(f) = 2\mathcal{S}_{\mathrm{PLL}}(f)+\mathcal{S}_{\phi_{\mathrm{REF}}}(f)\left[\left(\frac{f_{\mathrm{RF}}}{f_{\mathrm{REF}}}\right)^2+\left(\frac{f_{\mathrm{RF}}f_{\mathrm{LO}}}{f_{\mathrm{REF}}^2}\right)4\sin^2(2\pi f t_c)\right]. \tag{3.27}$$

Accordingly, the SNR with TX-RX leakage can be quantified as shown below:

$$\mathrm{SNR} = \frac{\left(\frac{4\pi x_p}{\lambda}\right)^2\frac{P_{\mathrm{IF1}}}{4}}{S_{\mathrm{AM}}+S_{\Delta\phi_1}(f_m)P_{\mathrm{IF1}}+2|S_{\Delta\phi_1,\Delta\phi_c}(f_m)|\sqrt{P_{\mathrm{IF1}}P_{\mathrm{IFc}}}+S_{\Delta\phi_c}(f_m)P_{\mathrm{IFc}}}. \tag{3.28}$$

Compared with that of (3.15), the TX-RX leakage deteriorates the system SNR by increasing the residual phase noise. As will be seen in the numerical analysis in the next subsection, this deterioration is significant since the leakage signal is usually much higher than the reflected signal from the motion target.

3.2.4 A Numerical Example

To quantify the above analysis, a numerical example is given in this subsection. The parameters of an actual low-IF Doppler system, which will be developed in Section.3.4, are used in this example and given in Table.3.1. The system works at 2.4 GHz and uses an IF frequency of 1 kHz. According to the Friis' equation, we estimate the path loss $|G_\mathrm{P}| = 56\,\mathrm{dB}$ for a 2-m detection with an effective radar cross section area of $0.326\,\mathrm{m}^2$ for the test subject reported in [41].

The NSD of the amplitude noise, $8S_{RFN} = -129.1\,\mathrm{dBm/Hz}$ and $S_\mathrm{n,ADC} = -98.9\,\mathrm{dBm/Hz}$. Thus, the ADC noise is the dominant amplitude noise, resulting in $S_\mathrm{AM} = -98.9\,\mathrm{dBm/Hz}$.

For the NSD of the phase noise, we first study the uncorrelated phase noise NSD $S_\mathrm{uncorr}(f)$, which is mainly due to the PLL flicker noise and it is determined once the PLL chip is chosen. For example, the PLL ADF4351 (Analog Devices, Cambridge, MA) is used in our constructed system and its noise behavior is shown in Fig. 3.2. This graph compares different phase noise contributions of ADF4351 at different offset frequencies. At 1–Hz offset, which is the motion frequency of our interest ($f_m = 1\,\mathrm{Hz}$), the PLL flicker noise, with a power level of $-68\,\mathrm{dBc/Hz}$, dominates the total PLL phase noise. When two of ADF4351 are used for the TX and LO signal generation, respectively, it results in a $S_\mathrm{uncorr}(f)$ of $-65\,\mathrm{dBc/Hz}$ at 1–Hz offset frequency. $S_\mathrm{uncorr}(f)$ can be easily elevated by choosing PLL chip of lower flicker noise. For example, a 12-dB improvement can be observed in Fig. 3.2 when PLL LMX2594 (Texas Instruments, Dallas, TX) is used.

3.2.4.1 Without TX-RX leakage

Fig.3.3 shows the calculated NSD $\mathcal{S}_\mathrm{corr}(f_m)$ and $\mathcal{S}_\mathrm{uncorr}(f_m)$ with respect to the normalized detection range d/λ, where $\lambda = 0.125\,\mathrm{m}$ at 2.4 GHz. $\mathcal{S}_\mathrm{corr}(f_m)$ gradually increases as d increases while $\mathcal{S}_\mathrm{uncorr}(f_m)$ stays the same at $-65\,\mathrm{dBc/Hz}$. Interestingly, when $d = 2238\lambda = 279.75\,\mathrm{m}$, $\mathcal{S}_\mathrm{corr}(f_m) = \mathcal{S}_\mathrm{uncorr}(f_m) = -65\,\mathrm{dBc/Hz}$, although this range is

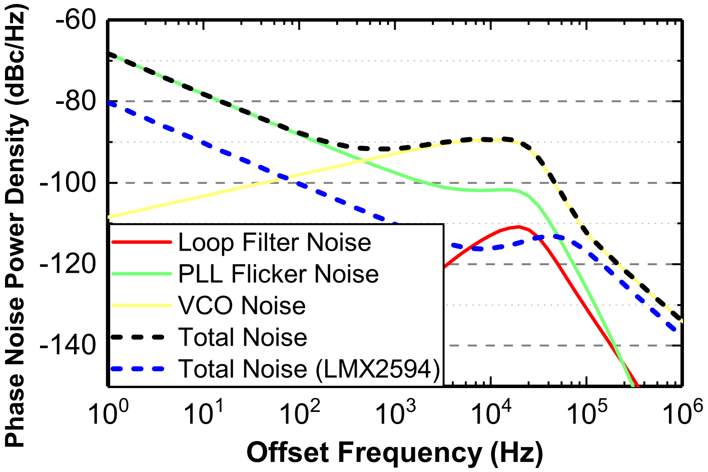

Figure 3.2: Simulation data consisting all sources of phase noise levels for PLL ADF4351 and the total phase noise level of PLL LMX2594.

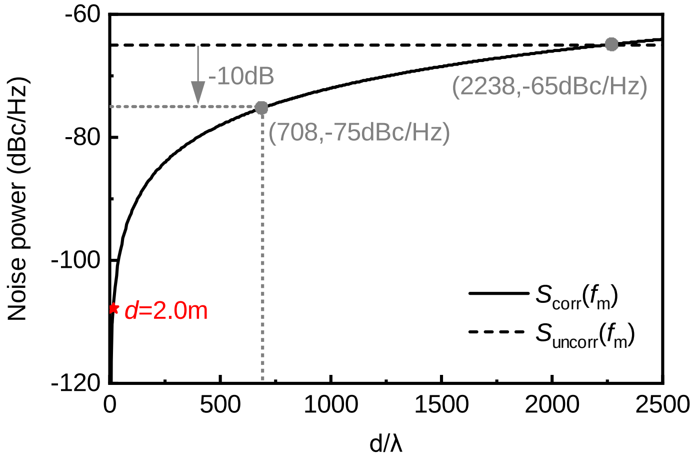

Figure 3.3: Caculated $\mathcal{S}_{\text{corr}}(f_m)$ and $\mathcal{S}_{\text{uncorr}}(f_m)$ with respect to different detection range d/λ.

unrealistic in motion detection due to the limited radiation power. When d is in the range of $0 \sim 708\,\lambda$ (88.5 m), $\mathcal{S}_{\text{corr}}(f_m)$ is more-than 10-dB lower than $\mathcal{S}_{\text{uncorr}}(f_m)$. For example, in the proposed example, $d = 2\,\text{m}$ corresponds to a $\mathcal{S}_{\text{corr}}(f_m)$ of 107.9 dBc/Hz, which is 42.9 dB lower than $\mathcal{S}_{\text{uncorr}}(f_m)$. Thus, $\mathcal{S}_{\text{uncorr}}(f_m)$ is the major contribution to the residual phase noise and $\mathcal{S}_{\text{corr}}(f_m)$ can be neglected. As a result, the SNR in (3.15)

Table 3.1: System parameters

Description	Symbol	Value
Antenna gain	G_{ant}	6 dBi
LNA gain	G_{LNA}	22.8 dB
LNA NF	NF_{LNA}	0.28 dB
Mixer gain	G_{mixer}	-7.3 dB
Mixer NF	NF_{mixer}	8.3 dB
IF OPAMP gain	G_{IF}	20 dB
IF OPAMP NF	NF_{IF}	34 dB
ADC system noise	$e_{\text{n,ADC}}$	$0.4\,\text{mV}_{\text{rms}}$
ADC sampling frequency	f_s	50 ksps
TX power	P_T	0 dBm
Reference frequency	f_{REF}	100 MHz
LO frequency	f_{LO}	2.45 GHz
IF frequency	f_{IF}	1.0 KHz
RF noise temperature	T	290 K
Motion magnitude	x_p	0.25 mm
Round-trip delay	t_d	$26.7\,\text{ns}^{\#}$
Reference PSD*	$S_{\Phi_{\text{REF}}(f)}$	-40 dBc/Hz

#: corresponding to a 2-m detection range.

*: at 1-Hz offset frequency.

can be approximated as

$$\text{SNR} \approx \frac{\left(\frac{4\pi x_p}{\lambda}\right)^2 \frac{P_{\text{IF1}}}{4}}{\mathcal{S}_{\text{AM}} + 2\mathcal{S}_{\text{PLL}}(f_{\text{m}})P_{\text{IF1}}}. \tag{3.29}$$

With a TX power level of P_T and a RX gain of $G_{\text{RX}} = 35.5\,\text{dB}$, the IF signal power P_{IF1} can be extracted as

$$P_{\text{IF1}} = G_{\text{RX}} + G_p + P_T = -20.5\,\text{dB} + P_T\,(\text{dBm}). \tag{3.30}$$

The motion signal and the residual phase noise power are proportional to the IF signal power P_{IF1}. As such, both of them increase linearly when the TX power changes from -40 dBm to 20 dBm, as shown in Fig. 3.4 (a). However, the amplitude noise level stays the same at -98.9 dBm/Hz. When the TX power is lower than -13 dBm, the total system noise is dominated by the amplitude noise and in this case the SNR increases with

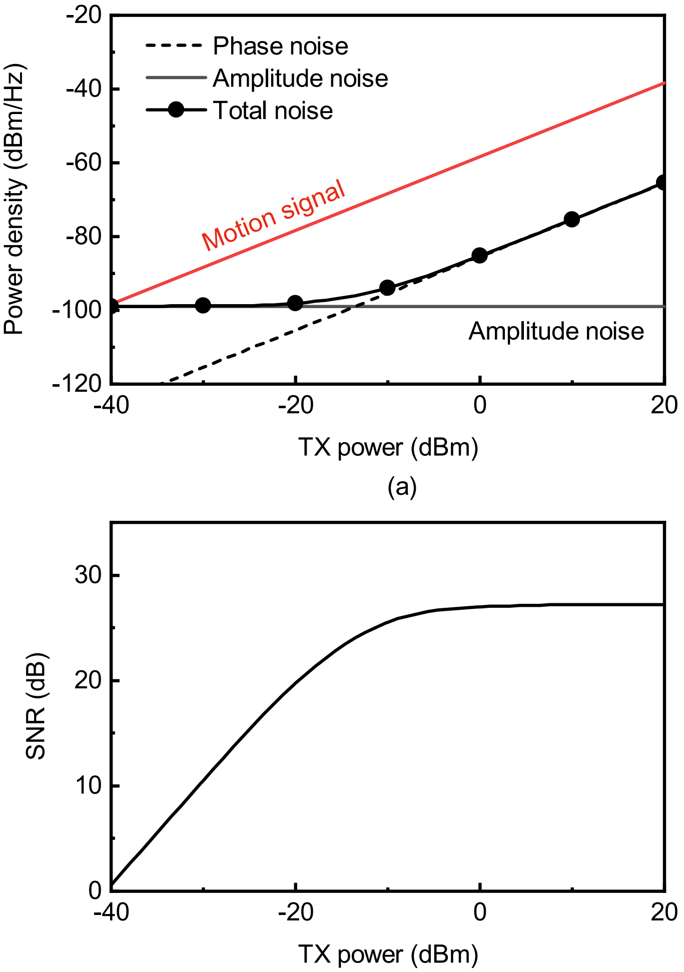

(a)

(b)

Figure 3.4: Calculated noise and SNR results without coupling. (a) Motion signal and noise power density with respect to TX power. (b) SNR with respect to TX power.

respect to the increased TX power, as shown in Fig. 3.4 (b). When the TX power exceeds $-13\,\mathrm{dBm}$, the phase noise overtakes the amplitude noise and increases at the same trend with the motion signal power, leading to an unchanged SNR even when the TX power is further increased. Consequently, increasing the TX power can improve the system SNR only when the residual phase noise is much lower than the amplitude noise level.

3.2.4.2 With TX-RX leakage

A TX-RX leakage signal is included here to study the behavior of the leakage signal effect on the system SNR. In a similar way, the SNR with leakage effect in (3.28) can be simplified by neglecting $\mathcal{S}_{\mathrm{corr}}(f_m)$ since it is 42.9 dB lower than $\mathcal{S}_{\mathrm{uncorr}}(f_m)$, as shown

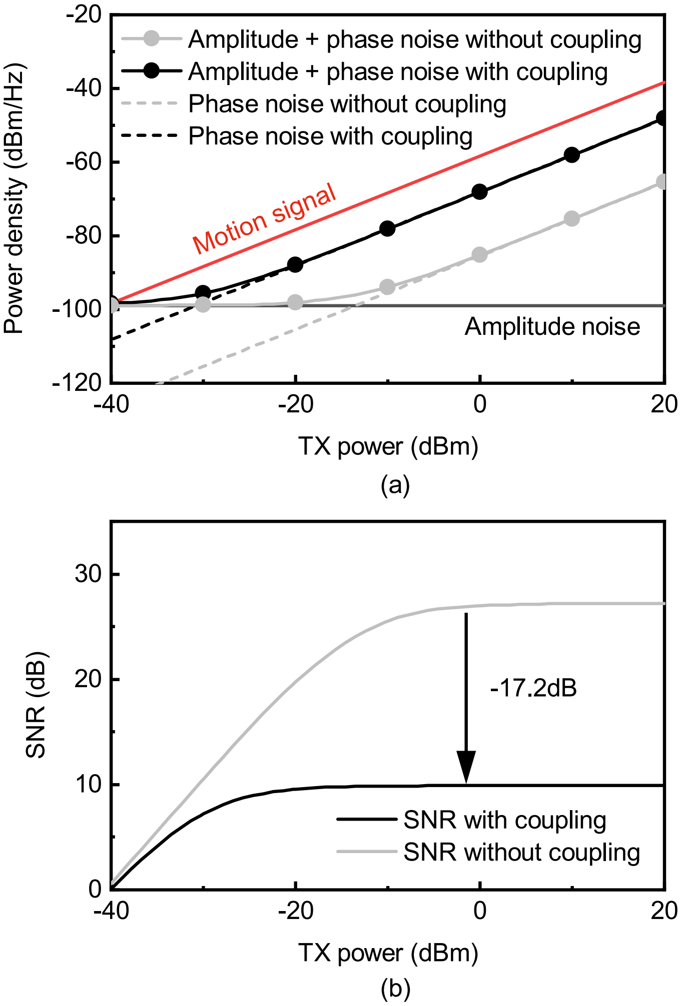

(a)

(b)

Figure 3.5: Calculated noise and SNR results with a −40-dB TX-RX leakage. (a) Motion signal and noise power density with respect to TX power. (b) SNR with respect to TX power.

bellow.

$$\mathrm{SNR} \approx \frac{\left(\dfrac{4\pi x_p}{\lambda}\right)^2 \dfrac{P_{\mathrm{IF1}}}{4}}{S_{\mathrm{AM}} + 2\mathcal{S}_{\mathrm{PLL}}(f_m)\left[P_{\mathrm{IF1}} + 2\sqrt{P_{\mathrm{IF1}}P_{\mathrm{IFc}}} + P_{\mathrm{IFc}}\right]}. \tag{3.31}$$

The TX-RX leakage G_{c} is set to $-40\,\mathrm{dB}$ and P_{IFc} due to the TX-RX leakage signal can be extracted as

$$P_{\mathrm{IFc}} = G_{\mathrm{RX}} + G_{\mathrm{C}} + P_{\mathrm{T}} = -4.5\,\mathrm{dB} + P_{\mathrm{T}}\,(\mathrm{dBm}). \tag{3.32}$$

Compared (3.32) with (3.30), P_{IFc} is 16-dB higher than P_{IF1} even though the TX-RX leakage is as low as $-40\,\mathrm{dB}$. Fig. 3.5 plots the calculated noise and SNR results with leakage. It can be clearly seen from Fig. 3.5 (a) that the introduced TX-RX leakage significantly enlarges the residual phase noise while it has no effect on the motion signal and amplitude noise power. When the TX power increases from −40 dBm to 20 dBm, the amplitude noise level stays the same, but the motion signal and the residual phase noise level increase at the same trend. The interchange point of −13-dBm TX power in Fig. 3.4 (a) moves down to −30 dBm due to the enlarged phase noise. When the TX power is lower than −30 dBm, the amplitude noise is the dominant source for the system noise and the SNR in Fig. 3.4 (b) increases linearly to the TX power due to the increased motion signal power. On the contrary, when the TX power is higher than −30 dBm, the residual phase noise becomes the dominant factor for the system noise and increasing the TX power does not improve the SNR. Specifically, SNR remains at 10 dB regardless of the TX power as long as TX power is over 0 dBm. From the comparison results of Fig. 3.4 (b), it can be found that the introduced −40-dB leakage signal deteriorates the system SNR by almost −17.2 dB when the TX power is over 0 dBm. The analysis and numerical results reveal that the TX-RX leakage plays a significant roll in the system SNR which is of great importance in the motion detection of human vital signs.

3.2.5 System SNR Analysis Method Comparison

In this paper, we would like to investigate the coupling effect due to its various power levels without concerning the change of its phase offset relative to $LO(t)$. As a result, before starting the experiment section, two signal processing algorithms are compared to analyze their reliability with SNR analysis responding to the possible phase shift between the coupling and the reflection signal during the experiment.

3.2.5.1 Analysis with IQ Demodulation

The IQ demodulation is the most widely used processing algorithm to demodulate the motion information with avoiding the null-point issue. For the digital IQ demodulation performed in IF system, a sine and cosine waveform with a matched IF-frequency is generated to downconvert the acquired baseband signal to I and Q signals at dc. Since the motivation behind I and Q is to avoid the null-point operation of the system, only one of these outputs with high sensitivity is used for the analysis. Therefore, the generalized demodulated output, B_{out}, is derived as follows:

$$\begin{aligned} B_{out}(t) = A_{IF}cos\left[\frac{4\pi x(t)}{\lambda} + \phi_n(t-t_d) + \Delta\phi\right] \\ +A_{IFCL}cos\left[\phi_n(t-t_{CL}) + \Delta\phi_{CL}\right], \end{aligned} \tag{3.33}$$

$$\begin{aligned} Q(t) = A_{IF}sin\left[\frac{4\pi x(t)}{\lambda} + \phi_n(t-t_d) + \Delta\phi\right] \\ +A_{IFCL}sin\left[\phi_n(t-t_{CL}) + \Delta\phi_{CL}\right], \end{aligned} \tag{3.34}$$

with ϕ_n being the residual phase noise contributing majorly to the noise floor. In these equations, the first term represents the motion signal power varying with $\Delta\phi$ and the second term, which is due to the coupling/leakage without motion modulation, represents the changing noise power related to $\Delta\phi_{CL}$. Based on these equations, both signal and noise power can vary drastically with change in different phase offsets. Thus, this processing method will lead to inconsistent processed SNR results for I or Q signals, which creates difficulty in determining the relation between the coupling magnitude and the system SNR.

3.2.5.2 Analysis with Direct FFT

Due to the property of the IF system architecture, this single-channel system is immune to the detection null-point issue [22]. Unlike the varying signal and noise level with respect to different phase shifts in the IQ demodulation analysis, a constant phase shift does not affect the signal and noise level in a direct FFT spectrum of $IF(t)$. As a result, the direct FFT method is more favored in an IF system architecture for its consistency in SNR quantification during the measurements.

3.3 Phase Noise Validation

Section 3.2 revealed that the PLL flicker noise is the major contribution to the residual phase noise. To validate this, an experiment is conducted to measure the residual phase noise directly from the IF signals, as shown in Fig. 3.6 (a).

The experiment is designed as combination of the following parameters: two PLL ICs of ADF4351 and LMX2594; and two different lengths of wires: 0.3 m and 6 m. The various

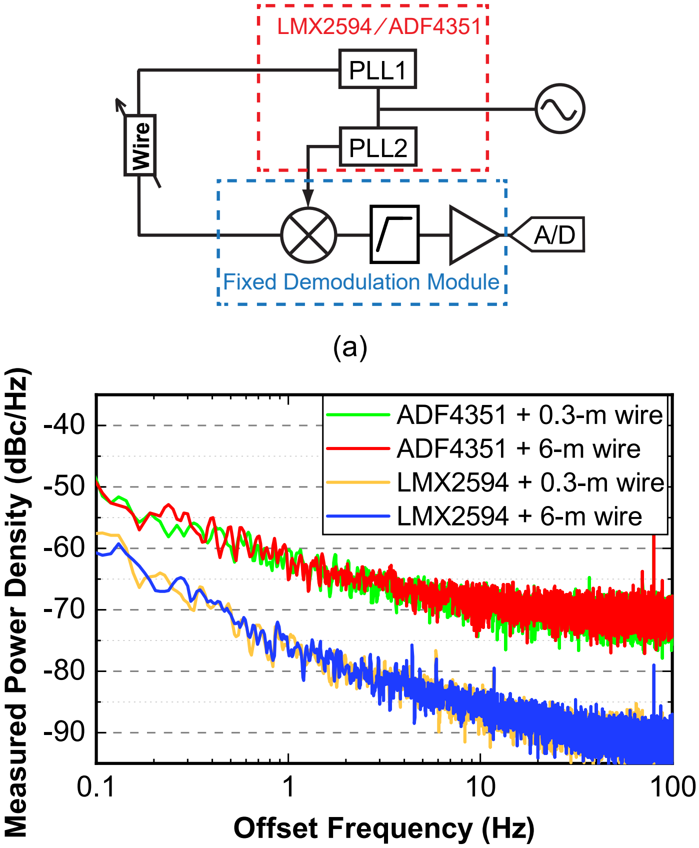

(a)

(b)

Figure 3.6: Phase noise measurement with changing PLL IC and delay between LO and RX signal. (a) Measurement diagram. (b) Measured power density for IF signal.

lengths of the wire correspond to different delay time travelled by the RF signal and three 2-m RF cables (FMC0202085-200CM) from Fairview Microwave are used for making this configuration. To make a fair comparison, the same PLL output power, reference signal, and demodulation module are applied for this experimental comparison.

During the signal processing step, each IF signal measurement includes both the signal and noise information where the signal power also takes RF cable insertion loss into account. A subtraction between the signal and phase noise power level is performed to convert the result unit from dBm to dBc. Each phase noise measurement result averages out over 10 recorded data (1-minute duration each) for smooting out the noise measurements. To further recover the noise power density from the power level readings from the FFT spectrum, the FFT processing gain of 15.5-dB is subtracted from the measured power. After that, the measured power spectrum in unit of dBc/Hz is shown in Fig. 3.6 (b).

On the other hand, the results obtained from varying different signal time delay overlap with each other no matter which PLL is used, as shown in Fig. 3.6 (b). Therefore, the measurement validates the theoretical analysis that the residual phase noise is majorly affected by the PLL flicker noise instead of the signal time delay within a travel distance of 6 m. From the ADF4351 PLL IC measurement result, the phase noise at 1-Hz offset is measured to be -63.5 dBc/Hz. Comparing with the simulation result, -65 dBc/Hz, there is a nearly 1.5-dB difference, which is expected due to the difference between the simulation and the fabricated IC performance. Compared with the measurement result of LMX2594, the phase noise level is observed to have a 13.5-dB improvement. This agrees reasonably well with the simulation prediction of 12 dB. Therefore, this indicates that the residual noise floor after the mixer is determined by the PLL flicker noise. By simply swapping the PLL IC, a 13.5-dB gain in SNR can be obtained.

3.4 Measurements using Test Bench Setup

Experiments are carried out to validate the coupling effect analyzed in the theory section. Due to the human body motion artifacts that bring uncertainty for the quantitative analysis, we used a linear-stage actuator (LSTG) to provide a reliable target motion. A flat reflector is attached to the front of the LSTG, together following a sine-wave trajectory with a 1-cm peak-to-peak range of motion oscillating at a frequency of 1.2 Hz. The LSTG is placed at a fixed distance of 2 m away from the radar system and the same settings are configured during all the quantified experiments conducted in this paper.

3.4.1 Coupling/Leakage Effect

As analyzed in the previous section, even a low TX-RX leakage can elevate the residual phase noise and therefore deteriorate the system SNR. To verify this effect, an extra leakage signal is introduced intentionally with a controlled amplitude. Fig. 3.7 (a) shows the system diagram where a 20-dB directional coupler is used at the TX output to introduce a coherent leakage signal. A USB-controlled attenuator with a tunable range of $0 \sim 30$ dB is used in the leakage path. Besides the 2-dB insertion loss due to the cables and tran-

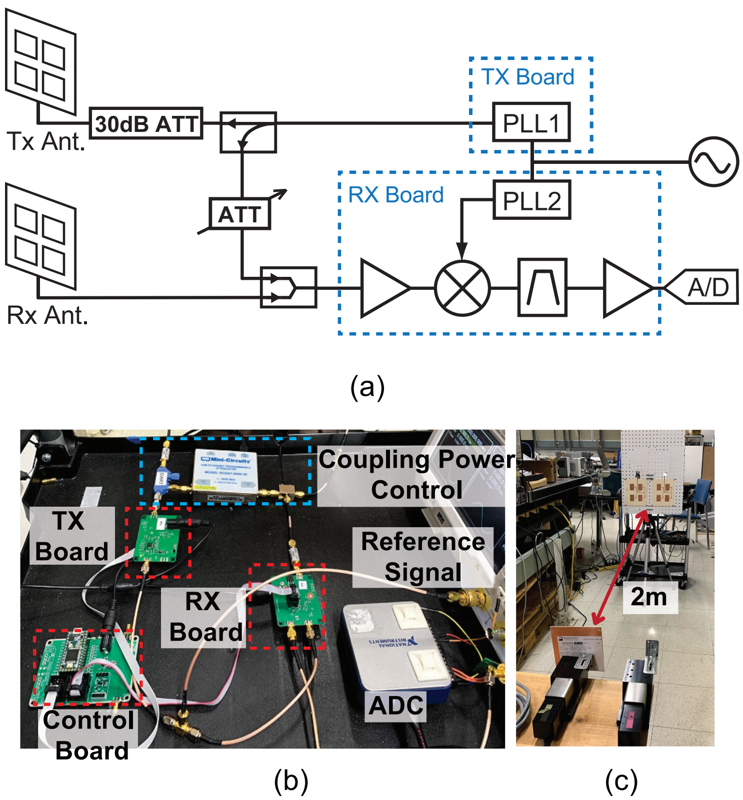

Figure 3.7: Coupling effect assessment with varying introduced power level of coupling (a) System diagram. (b) System setup. (c) Front view of the experiment setup.

sition connectors, the introduced coupling path can provide a TX-RX leakage signal of $-52 \sim -22$ dBm for a 0-dBm TX power. To minimize the transmission effect between the TX and RX antennas, a 30-dB attenuator is connected before the TX antenna. Besides, the antenna coupling is further suppressed by using a pair of array antennas with a high isolation property. Through all these means, the TX-RX leakage signal through the intentionally constructed leakage path is considered as the dominant TX-RX leakage source within the power adjustment range.

The dual-PLL system architecture is constructed using the compact dual-PLL TX and RX board modules. To ensure the phase coherence between the two RF signals, an 100-MHz reference generated using the function generator RIGOL DG4162 is shared between the two boards. The output frequency of PLL1 inside the TX board is set to 2.45 GHz while the PLL2 within the RX board is set to 2.450001 GHz, resulting in an 1-kHz output signal. At the IF output port of the RX board, the ADC is connected for acquiring the output signal with a sampling rate of 50 ksps. Fig. 3.7 (c) shows the front view of the system setup in which the LSTG is placed at 2 meters away from the system.

During the experiment, two 60-s data sets are recorded each time. For each data set, it first gets multiplied by the Blackman-Harris window function to increase the FFT dynamic range and then the FFT results are averaged to be displayed in Fig. 3.8 (a). As predicted from the theory section, the noise floor rises up with the increased IF level while the detected motion signal power remains the same. A quantitative comparison is displayed in Fig. 3.8 (b) where the detected motion signal power is obtained by averaging between the two peaks of the motion signal observed in Fig. 3.8 (a). Due to the preset motion frequency of 1.2 Hz, an average in linear scale across the spectrum between 1.3 $\sim$ 2.2 Hz is determined as the noise floor level of the system. On top of the measurement results, the simulated noise level is also added for comparison where the noise level is estimated based on three noise sources:

$$P_{nsimulated} = P_{AMPN} + P_{IF} \cdot S_{\text{uncorr}}(1) + P_{msig} \cdot S_{\text{uncorr}}(0.1) \tag{3.35}$$

The predicted noise level includes the absolute amplitude noise which is -114.4 dBm, the residual phase noise from IF that is 80.5 dB below the measured IF power level and the residual phase noise from the motion signal which is averaged to be 76.5 dB below the motion signal level. A less-than 2-dB error is observed when comparing between the predicted noise levels and the measurement results.

The measurement data in Fig. 3.8 (a) shows that the system noise level linearly goes up with increase in coupling magnitude. A 30–dB increase in coupling magnitude leads to a 29–dB increase in the noise level. On the other hand, the detected motion signal level initially remains constant within 1 dB but goes down when the coupling level gets closed to the motion signal power. In terms of SNR level, an extra 30-dB increment in change of the coupling power level decreases the system SNR from 46 dB to 21 dB. In conclusion, this experiment justifies that the amount of extra coupling leads to a linear increase in the signal noise floor when the residual phase noise dominates the system noise floor.

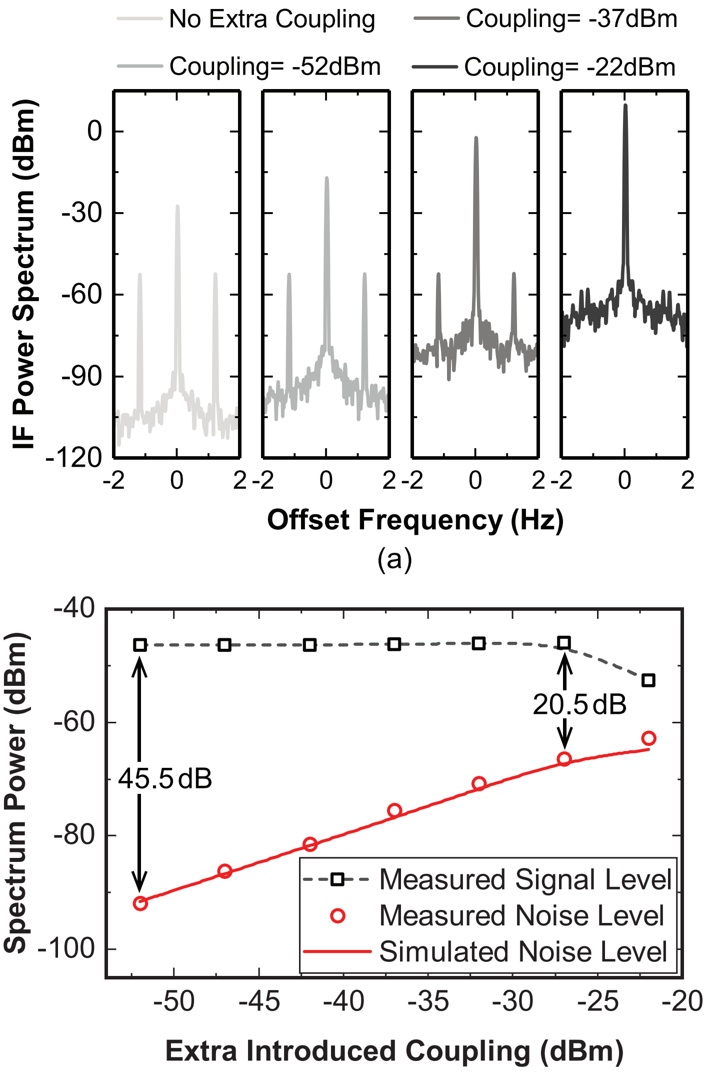

(a)

(b)

Figure 3.8: (a) The measured IF spectrum with different levels of introduced coupling power. (b) Motion signal and Noise floor magnitudes for different coupling power levels.

3.4.2 System Gain Effect

TX power level is a key parameter determining the system sensitivity during vital sign detection comparison, listed in the comparison table from [66]. Therefore, an experiment is carried out to test the impact of increasing TX power level on the system SNR for low-IF dual-PLL system.

The system diagram in Fig. 3.9 shows that the TX power level is controlled by a combination of a USB-controlled variable attenuator, a 30-dB fixed attenuator and a 12--dB LNA connected at the TX output. This power control unit is possible to configure the TX output to sweep across $-72\,\text{dBm} \sim +10\,\text{dBm}$. However, to overcome the other parasitic TX-RX leakage paths radiated between the RF boards, $-47\,\text{dBm}$ is set for the lowest power level during this experiment.

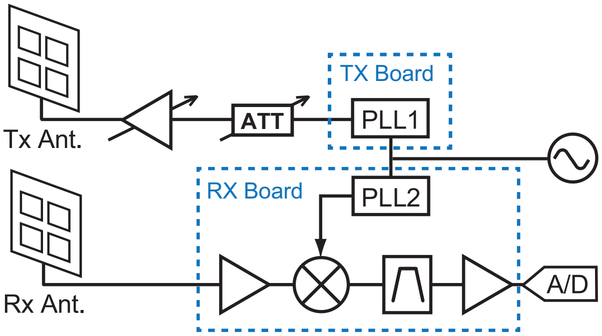

Figure 3.9: System diagram for varying TX power level using array antennas.

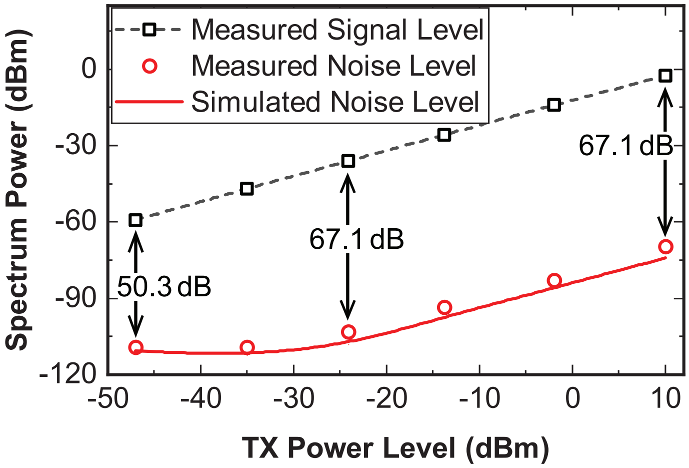

Figure 3.10: Motion signal amplitude and measured noise floor amplitude measured in IF domain with varying TX power levels.

The experiment monitors the signal and noise levels with sweeping TX power level from $-47\,\text{dBm}$ to $+10\,\text{dBm}$ with a step size of 10 dB. For each configuration, the IF output power is acquired as reference to analyze the detected motion signal and the noise level from the FFT spectrum. The results are reported in Fig. 3.10 where the precised TX power level is calibrated using its linear relationship with the measured signal level. On the other hand, for the noise floor level, the measurement and predicted noise level are reported to agree within 5.3-dB difference. The measured noise level kept at $-109.2\,\text{dBm}$ when P_{TX} is set below $-35\,\text{dBm}$. However, with P_{TX} going up beyond this power level,

Table 3.2: Comparison between performance using the phased-array antenna and the patch antenna

	Phased-Array Antenna	Patch Antenna
Gain	12 dBi	6 dBi
TX-RX Isolation	46 dB	30 dB
TX Power	-2 dBm	-5 dBm
Measured Noise Floor	-107.6 dBm	-92 dBm
Measured Motion Signal	-38.8 dBm	-55.4 dBm
Measured SNR	68.8 dB	36.6 dB

the noise floor level starts to elevate with similar slope as shown in the figure. Thus, the SNR are almost constant to be 68 dB within 1–dB error regardless of the TX power level when it is high enough so that the residual phase noise dominates the noise floor. These results and conclusions further support (3.28) analyzed in the theory section.

3.4.3 Antenna Parameters on System SNR

Since the phase noise level depends on the coupling strength where the antenna coupling plays a big effect, how would antenna parameters affect the system SNR? To address this question, a comparison study in the system performance is made between using a pair of phased-array antenna and the single-element patch antenna. The antenna parameters are shown in Table.3.2.

Based on the antenna gain difference and the TX power level difference, the difference in detected motion signal level is expected to be 15 dB while the measurement reports a motion signal level difference of 16.6 dB with only off by 1.6 dB. On the hand, the phase noise which is dominated by the antenna coupling signal can be predicted by the TX-RX isolation of the antenna. The phase noise level difference based on the measurement is reported to be 15.6 dB which agrees with the predicted 16 dB with an error within 1 dB. The SNR difference is measured to be 32.2 dB which is contributed by both gain and isolation difference between the two antennas.

Therefore, this comparison shows that during antenna design for Doppler radar system, the isolation between the TX and RX antennas is as important as the gain parameter that was traditionally focused on in communication system design. It is worth mentioning that the traditional view on the benefit of high antenna isolation in Doppler radar system is considered to create more headroom for higher LNA gain to be added for higher SNR achievement. This series of experiments show that without changing in system gain, a higher isolation for antenna will decrease the phase noise level which potentially leads to a higher system SNR.

3.4.4 RF Cancellation Effect

This section is to investigate the coupling cancellation effect on noise floor levels. As shown in the experiment diagram of Fig. 3.11, a pair of patch antennas is used to provide a relatively high TX-RX antenna coupling. The coherent cancellation path is created by a power divider adding to the output of the TX board. The coherent waveform then goes through a phase shifter and a variable attenuator connected in series to be finally combined with the coupling received from the RX antenna.

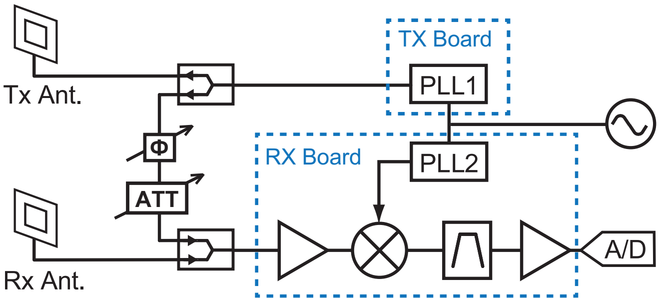

Figure 3.11: System diagram for RF cancellation using patch antennas.

To achieve a complete cancellation of the coupling, the cancellation path waveform needs to have the same power level but 180° out of phase comparing with the coupling. The same linear actuator is used and placed at 2m away from the system and the actual setup is shown in Fig. 3.12. To observe the cancellation depth, which represents how much the RF signal gets suppressed, a spectrum analyzer RSA3408 from Tektronix is connected to the output of the RX board for continuous IF power monitoring. By manually going through different settings for the phase shifter and variable attenuator, different cancellation depths are achieved.

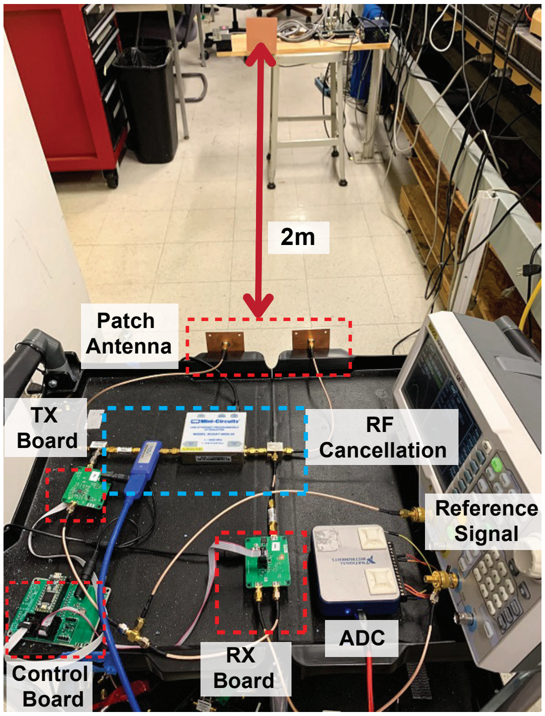

Figure 3.12: System Setup for RF Cancellation

The measurement result is shown in Fig. 3.13 where the noise floor first linearly decreases with the cancellation depth within the first 20 dB as the total noise level is mainly contributed by the residual phase noise from the coupling. Then, the residual phase noise from the IF and motion signal starts to dominate during the 30-dB and the 55-dB RF cancellation depth. Overall, the 43–dB coupling cancellation depth leads to a 30.4–dB noise floor reduction, which decreases from −67.1 dBm to −97.5 dBm. With the motion signal level unchanged within 1 dB, this leads to an SNR improvement around 30 dB. Therefore, the RF cancellation is verified to be an effective method to increase the system SNR.

Additionally, the predicted noise level is included in Fig. 3.13 which shows that the prediction agrees with the measured noise level within 4 dB when the RF cancellation depth is less than 30 dB. The prediction error is increased to 9 dB when the RF cancellation depth is 55 dB where the residual phase noise does not further go down with the IF power. This effect can be caused by the residual noise after the cancellation between the target reflection signal and the cancellation signal due to their long delay-time difference.

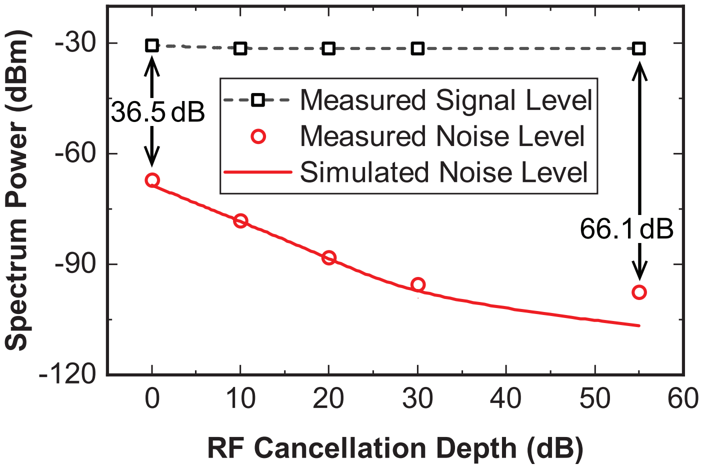

Figure 3.13: Motion signal amplitude and measured noise floor amplitude measured in IF domain with varying RF cancellation depth with using patch antennas.

3.5 RF Cancellation on Improving Vital Sign Detection

Due to its ability to lower the noise level of the system, the RF cancellation is performed on vital sensing. The subject sits at 2 meter away from the system and the cancellation is done with changing the phase and amplitude of the cancellation path signal to decrease the IF carrier signal. A comparison is done with and without cancellation to testify the effect of the RF cancellation. The result is presented in Fig. 3.15 where the IF signal

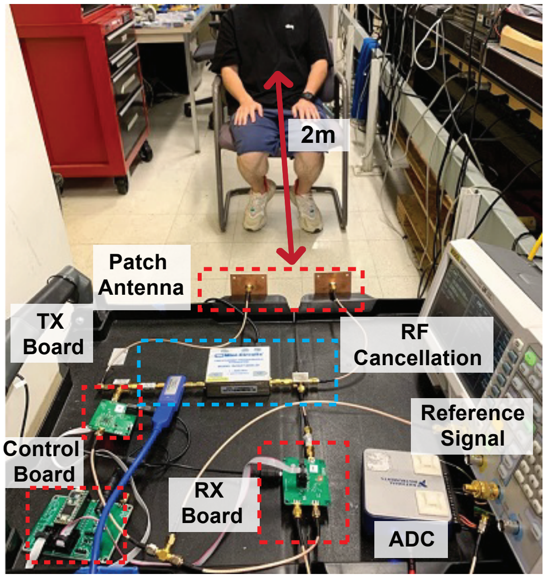

Figure 3.14: Vital sign measurement setup with RF cancellation technique

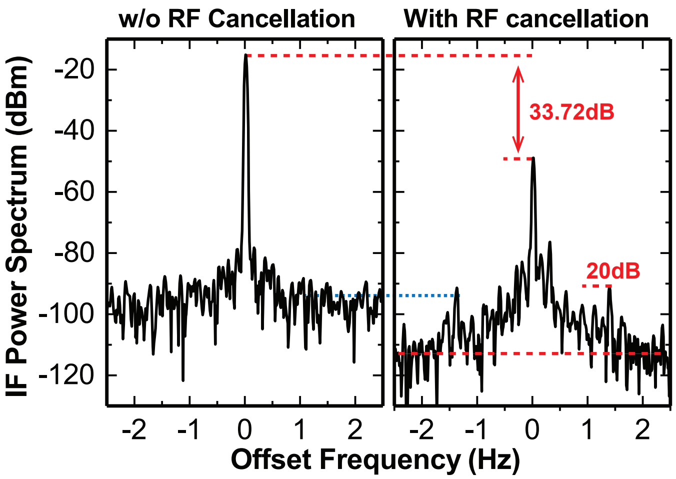

Figure 3.15: RF cancellation technique during Vital sign detection result

is cancelled by 33.72 dB marked by the red dashed line. The system noise floor is also improved by at least 20 dB. This prediction can be made because the motion of the subject is not a pure sinusoidal wave so that the spectrum of the motion will consist of a wide-band frequency components. As a result, the system noise floor should below the lowest spectrum component caused by the motion. Furthermore, the blue dotted line indicates that the heart motion signal is indeed blocked by the noise floor when no RF cancellation is applied. Therefore, this comparison shows that the RF cancellation can improve the system SNR by at least 20 dB to make it possible for the system to detect heart motion of an subject in 2 meter away.

3.6 Summary

In this chapter, we first analyze the noise contribution for the Dual-PLL system architecture and identify the PLL flicker noise to be the major contribution to the noise floor. The system SNR analysis is provided with the consideration of the coupling effect. We also show that excessive coupling/leakage level can raise the noise floor in the system. Therefore, the RF cancellation technique is proposed and verified to effectively improve the system SNR by at least 20 dB. The manual RF cancellation technique is also proven to be an effective method to improve the system sensitivity during remote vital sign detection.

Chapter 4

Automatic Coupling Cancellation Development for IF System

Instead of the bulky devices used in the experiment studies in the previous section, an integrated and robust hardware solution of the RF cancellation technique based on the commercial ICs is presented in this section. Besides that, a processor unit is designed for algorithm implementation to automatically find the optimum phase and amplitude settings for the phase shifter IC and the variable attenuator IC respectively.

4.1 Hardware Implementation

Fig. 4.1 shows the hardware implementation diagram of for RF cancellation where two additional modules are designed: the RF cancellation module and the DSP (Digital signal processing) module. To begin with, the RF cancellation module takes in a portion of the TX signal which then goes through a variable phase shifter (PE44820B) with a fine phase adjustment step of 1.4^o across the whole range and a variable attenuator (HMC624) with a fine gain adjustment step of 0.5 dB for a range of 31.5 dB. After that, the output gets combined with the RX signal received from the RX antenna. To compensate the loss during the power combining, the waveform is amplified by an LNA (QPL9096) and fed into the RX board. For the control unit, the DSP module consists of an analog level shifter, an STM32H7 micro-controller and an ESP32 microcontroller. Two microcontrollers are used here to separate the date acquisition and the algorithm implementation tasks. The

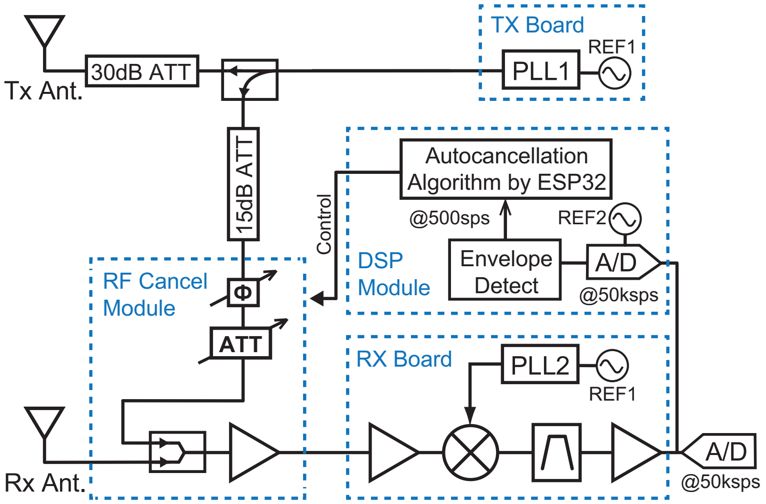

Figure 4.1: Automatic RF cancellation implementation diagram.

STM32H7 is used for sampling the output signal with a sampling rate of 50 ksps. This requires a level shifter at front to shift the bias level from 0 V to 1.5 V. The STM32H7 then processed for the output signal amplitude information, which is then passed to the ESP32 via UART communication. Note that only processing the amplitude information of the IF output is enough to analyze the RF cancellation depth during the algorithm implementation. To ensure an accurate reading for the amplitude, a coherent sampling is implemented by synchronizing the reference between the PLL and the STM32H7. After the ESP32 processor reads the amplitude data, the phase shifter and the attenuator of the RF cancellation module are digitally controlled by the ESP32 through the SPI protocol. In summary, this design is able to automatically configure the phase and magnitude of the waveform in the RF cancellation path based on the feedback provided from the amplitude reading of the acquired output signal.

4.2 Automatic RF Cancellation Algorithm

Gradient descend algorithm has been adopted for a fast RF cancellation implementation that requires an initial pair of attenuation and phase values to start with. The algorithm first finds the slopes in the nine directions around it and then takes a fine step towards the direction with the strongest negative slope. This process is repeated until no negative slope is observed from any direction. To implement this algorithm in this scenario, we first construct a coordinate system with two input variables: attenuation and phase shift values. Each pair of input variables corresponds to an IF amplitude that indicates its coupling cancellation depth. Fig. 4.2 provides an illustration of the coordinate structure in which the IF power levels change with different input combinations. The final optimum point is the attenuation and phase shift setting that produces the lowest IF amplitude. In order to estimate the slopes in different directions, a subtraction in IF magnitudes between the surrounding points and the center point is applied. Then, the neighboring point with the strongest negative slope is selected to be the next center point. Eventually, the optimal settings are found until the slopes are non-negative in all directions.

4.2.1 Accommodation for Wide-range Scenarios

Depending on the different magnitude and phase of the coupling/leakage, the optimum point is shifted away from the case shown in Fig. 4.2. In fact, it will be randomly scattered over this 2D map. Thus, if a fixed starting point is chosen for the gradient descend algorithm, the search time will vary greatly between the different scenarios. In order to average the search time, a 2-D coarse sweep is therefore carried out over the entire range of the attenuation and phase values to find the optimal starting point with the lowest IF amplitude. The 2-D coarse sweep also effectively increases the system dynamic range by always starting in the areas without baseband saturation for the gradient descend algorithm.

4.2.2 Trade-off Due to Components Parasitic

Ideally, the RF cancellation depth versus the input variables follows a strict convex functional behavior, which means that there is only one local minimum during any data sets of the function. This indicates that the gradient descend method should be perfectly suited for this situation without having to worry about being trapped to a local minima.

The convex functional behavior is guaranteed when transition states within the phase shifter and the attenuator IC are monotonic. This is expected for ideal phase shifter where the phase shift should always increase as the code changes from the lowest state to the highest state. At the same time, the attenuation for the phase shifter should ideally

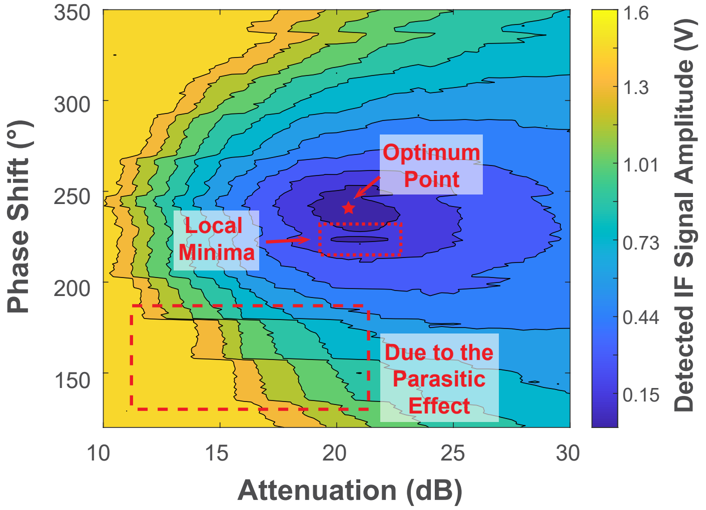

Figure 4.2: Part of two-dimensional sweep done by the RF cancellation board with full range of attenuation and phase shift settings.

be kept the same in all states, since only one variable should change at a time. Similar standards are expected from the ideal attenuator IC.

However, due to the differential non-linearity in the product ICs, the monotonicity cannot be maintained, which results in local minimum points. The parasitic effect is shown in Fig. 4.2 where most of the abrupt changes occur horizontally. This indicates that the phase-shifter is mainly responsible for the cause of this effect due to the mismatch between different bits. Because this creates a sharp local minimum, a big step in the gradient descend algorithm can be adopted to avoid getting the algorithm trapped. To compensate for the resolution lost from the big-step algorithm, a 2D sweep with the least significant bit of the ICs is required to keep the same search resolution. However, this 2D sweep increases the overall processing time for the algorithm and introduces a trade-off between speed and accuracy. A small step size has the advantage of faster algorithm speed but carries the risk of being trapped to a local minimum while a large step will likely to locate the area containing the global minimum but with a longer processing time.

4.2.3 Optimum RF Cancellation Algorithm

There are two basic algorithms: gradient descend and 2D map algorithm. gradient descend has been discussed at the beginning of this subsection. The 2D map is to always sweep a fixed number of points in the selected range and the algorithm is to decrease the range from the full-scale by half each time until the step size reaches the least significant bit of the IC component. The 2D map is less sensitive to parasitic of the IC components but comes with a drawback of longer processing time. Therefore, an optimum algorithm needs to balance between accuracy and processing speed.

Apart from increasing the step size, another approach to increase gradient descent accuracy is to introduce more stochastic elements in the algorithm. Therefore, randomness adding to the starting position can be adopted for accuracy improvement while maintaining a lower processing time. This leads to our proposed optimum algorithm whose diagram is shown in Fig. 4.3. This algorithm performs three gradient descend processes starting with three different starting positions. Because the phase shifter is observed in Fig. 4.2 to contribute the majority of the parasitic, the two other starting points are selected with one phase step size away from the minimum point derived from the coarse 2D sweep. In the end, the optimum RF cancellation point is determined by comparing the results obtained from the three processes.

4.2.4 Comparison Between RF Cancellation Algorithms

In order to validate the optimum algorithm proposed in the previous section, an experiment has been set up to feed an attenuated TX signal directly to the receiver through a phase shifter to vary the optimum point position obtained from the RF cancellation algorithm.

In this experiment, the gradient descent method, 2D map method and the stochastic gradient descent method are used to compare in aspects of the processing time and the RF cancellation depth. The experiment setup is shown in Fig. 4.4 where a 45-dB attenuation has been fixed and added to the TX signal. On the other hand, the phase shifter connecting to the TX output adjusts the TX signal phase from $0°$ to $400°$ with a step size of $8°$. The comparison result is shown in Fig. 4.5 where the box chart in (a) shows that the stochastic gradient descend algorithm has a similar accuracy comparing with the 2D map algorithm and the average cancellation depth for both algorithms is 30 dB. However, the gradient descend algorithm is lack of consistency to obtain the optimum

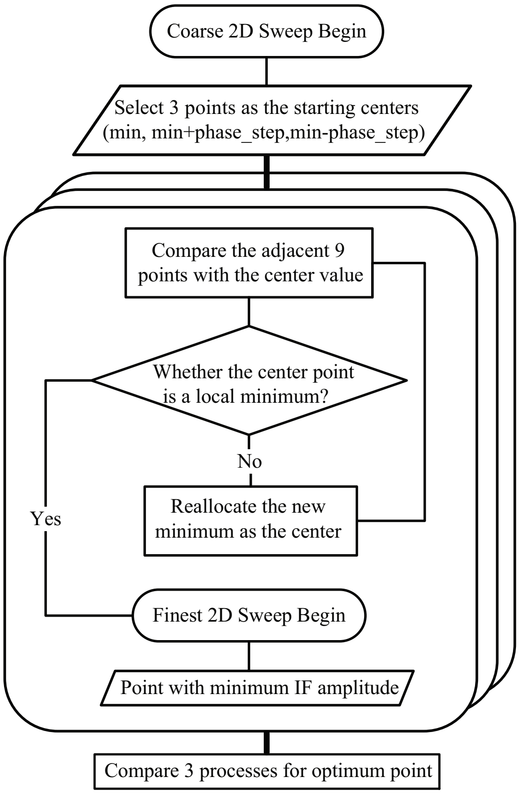

Figure 4.3: Diagram for stochastic gradient algorithm.

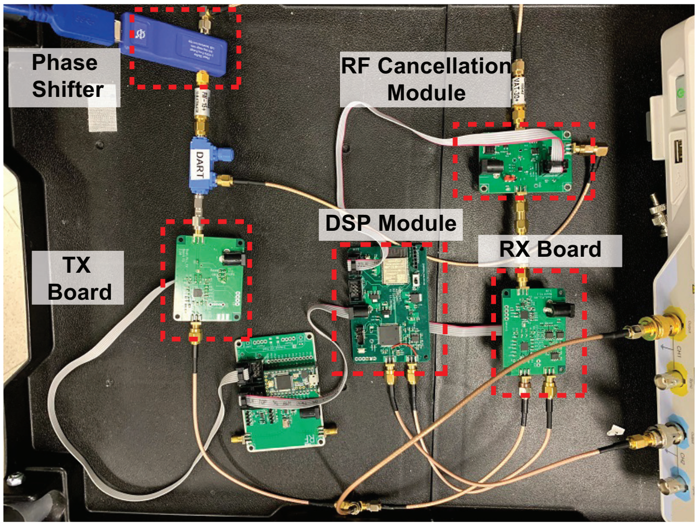

Figure 4.4: Parasitic effect validation test bench with changing TX signal phase shift.

RF cancellation depth due to the parasitic effect. The average cancellation depth for Gradient descend method is 25.7 dB. On the other hand, the box chart in (b) reports that the gradient descend algorithm consumes the least amount of processing time averaging

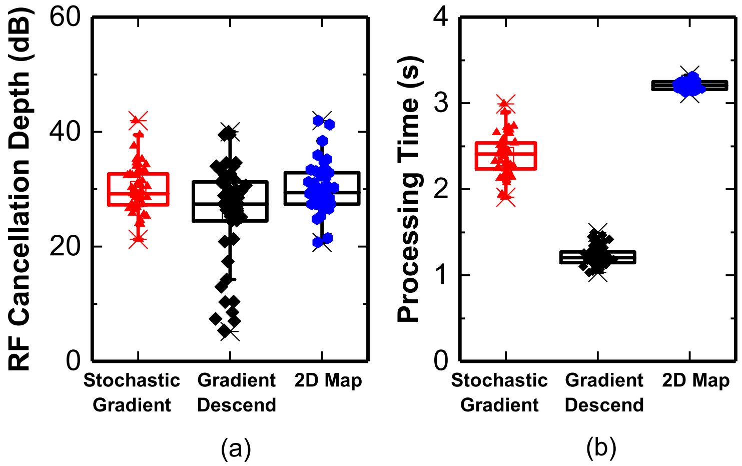

Figure 4.5: Comparison with different algorithms by changing the phase shift of the TX signal. (a) Comparison in RF cancellation depth. (b) Comparison in processing time.

1.23 s per process. The 2D map algorithm consumes the highest amount of processing time, 3.2 s. The stochastic gradient method is in between the others and uses 2.4 s in average for one cancellation process. Therefore, in order to keep the same accuracy and to speed up the process, the stochastic gradient algorithm is considered as an optimum algorithm to balance the cancellation accuracy with the processing speed.

4.3 Low TX Power Vital Sign Detection

Since it has been experimentally verified that a large TX power does not effectively increase the system SNR for remote motion detection when residual phase noise is the determining factor, a system can maintain a similar SNR with much less transmitted power to save power consumption. Combining with the RF cancellation technique, the detection distance can also be extended for vital sign detection. Therefore, a low-power and long-distance experiment has been conducted to evaluate the performance of the automatic RF cancellation technique.

4.3.1 Experiment Setup

The patch antenna was used in the system with a gain of 6 dBi. A 30-dB attenuator was added to the TX board output where the output power was measured to be −31 dBm at

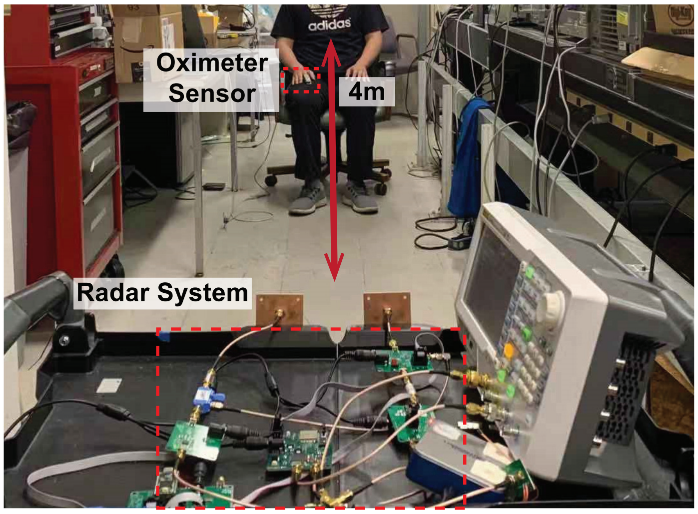

Figure 4.6: Automatic RF cancellation implementation setup with a subject sitting at 4 m away from the radar system.

2.450001 GHz. To suppress the effect of RF interference in the industrial, scientific and medical (ISM) band, the WiFi and Bluetooth service for all ISM devices are disabled trying to neglect the effect from the RF interference. One male healthy volunteer participated in this experiment and was asked to be seated in a distance of 4 m away from the radar system for a period of 130 seconds. The picture of the measurement setup is displayed in Fig. 4.6. During the first half of the recording, the attenuator on the cancellation path was set to the highest attenuation setting for minimum cancellation effect. Automatic RF cancellation was triggered at around 65 s so that a comparison can be made before and after the RF cancellation. The subject was wearing an oximeter sensor to provide a ground truth reference for comparison with the radar measurement.

4.3.2 Result Analysis

The measurement result is shown in Fig. 4.7 where (a) displays a 20-s time domain waveform that shows the full cancellation process which takes approximately 2.5 s. The time domain waveform (a) shows the amplitude change before and after the RF cancellation. (b) and (c) are the fft results based on a 60-second time domain data. The comparison identifies an IF power reduction of 34.5 dB. This leads to a decrease in the spectrum noise floor which results in a clear identification of the heart rate information of the subject after RF cancellation as shown in (c). Even though it is not possible to quantify how much

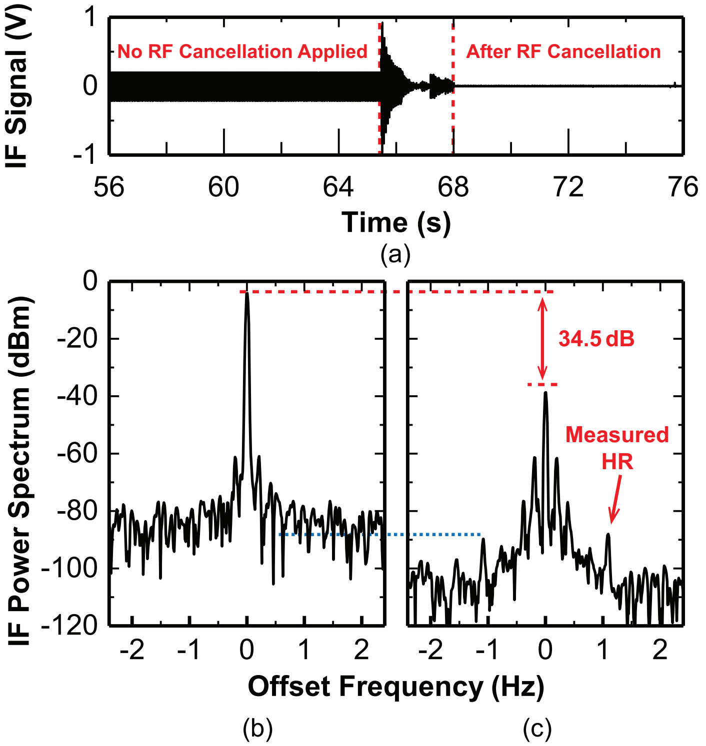

Figure 4.7: Measurement result from 4-m vital sign detection. (a) 20-second time domain waveform that shows the RF cancellation process. (b) Frequency domain analysis without RF cancellation. (c) Frequency domain analysis after applying RF cancellation.

improvement on noise floor level due to the complex motion detected by the system, a more than 15-dB SNR improvement is observed with adopting the RF cancellation in this scenario.

In order to demonstrate the accuracy of the heart rate detection by the proposed RF cancellation technique, a spectrogram with 20-s time domain window was processed and compared with the reference data acquired by the oximeter sensor with a threshold of −95 dBc/Hz. The two graphs (a) and (b) in Fig. 4.8 compare the spectrogram based on the measurement data before and after RF cancellation respectively. The red dash line marks the heart-rate frequency reference from the oximeter sensor. Fig. 4.8 (a) is resulted from the first 60-s data where the noise power spreads across 1–2 Hz without observable RF detection result aligning with the reference. In comparison, (b) has a clear heart-motion spectrum standing out during the 1–2 Hz frequency range. The oximeter reference detected the heart rate of the subject gradually changed from 1.05 Hz to 1.13 Hz which

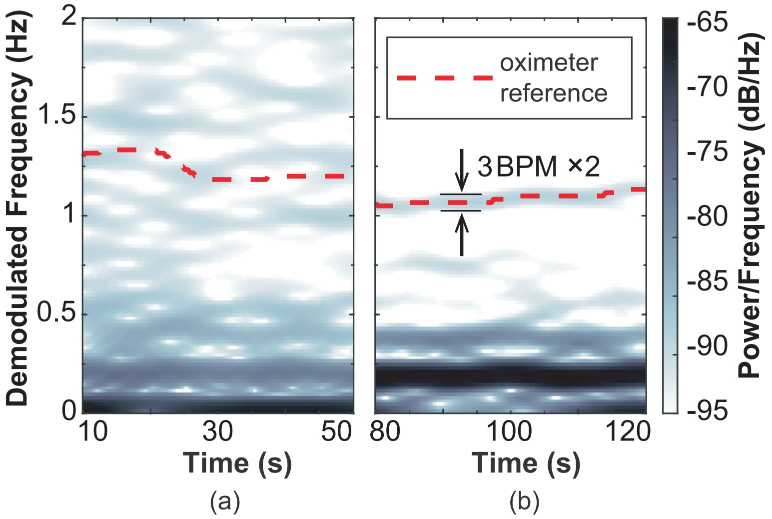

Figure 4.8: 60-s spectrogram based on the demodulated baseband signal resulted from the 4-m vital sign detection. (a) Before applying RF cancellation (b) After applying automatic RF cancellation.

converts to 63 BPM and 68 BPM respectively. As shown in (b), the radar measurement always agrees with the oximeter reference data with a confidence level of 3 BPM difference across the entire 60-s measurement.

4.4 Through Wall Vital Sign Detection

In the previous section, it has been shown that the antenna coupling effect can be improved by the RF cancellation technique to extend the system sensing range. That also indicates that if there is no coupling/leakage existed in the first place by using high-isolation antennas, the sensing range could also be inherently far. However, there is one scenario that the system inevitably experiences SNR degradation and high coupling power even if high-isolation antennas are adopted. It is the through-wall vital sign detection.

One advantage for RF system to detect vital sign signal is that it can ”see-through” the objects in between the radar and the target. However, the obstruction in-between can add return loss to the RF signal as well as increase unwanted coupling power by acting as a big reflector. And this has not been quantified well with how much SNR degradation a wall in-between brings to the measurement result. Furthermore, it also requires an effective way to increase the system sensitivity in this scenario. Therefore, a test-bench measurement is firstly conducted to quantify the through-wall detection effect as well as to investigate the benefit of RF cancellation applicable to this scenario.

4.4.1 Test-bench Setup Measurement

The LSTG was placed 2-m away in all test cases to act as a constant motion target. Several tests have been conducted to compare the performance between the reference case with the through-wall measurement to quantify the SNR variation due to the effect of wooden wall and the RF cancellation technique. The measurement results are reported in Tab. 4.1 where the setup in Case 1 acts as a reference case with air in between. When the TX power was set to −31 dBm, the IF power was measured to be −11.3 dBm which leads to a noise floor level of −91.7 dBm. A detected motion signal level of −33.6 dBm leads to a measured SNR level of 58 dB for the reference case. On the other hand, the case 2 and 3 were set up with a 15-cm wooden wall in-between the LSTG and the radar system. In case 2, the −5.8 dBm measured IF power and −45.3-dBm motion signal level indicate that the wooden wall contributes to a 5.5-dB coupling power level increase and an additional 11.7-dB increase in path loss. In total, the SNR degradation due to the obstruction wall is around 16 dB.

Table 4.1: Comparison between different setups for through-wall motion detection using LSTG @2 m away

Case Number	1	2	3
TX Power	−31 dBm	−31 dBm	−31 dBm
Object in-between	Air	Wall	Wall
Cancellation Status	OFF	OFF	ON
IF Power	−11.3 dBm	−5.8 dBm	−38.5 dBm
Motion Signal	−33.6 dBm	−45.3 dBm	−44.2 dBm
Noise Level	−91.7 dBm	−87.3 dBm	−102.4 dBm
Measured SNR	58 dB	42 dB	58 dB

After RF cancellation been applied in Case 3, the noise floor level decreases by 15.1 dB with a RF cancellation depth of 32.7 dB. The detected motion signal level is 0.9 dB in difference comparing with the Case 2, which leads to an SNR improvement of 16 dB by adopting the RF cancellation technique. Since the noise floor is now dominated by the ISM band RF interference, the RF cancellation effect is underrated during this low-power detection setup. However, with the 16-dB SNR improvement, the SNR degradation due to the obstruction wall can still be effectively diminished.

4.4.2 Through-Wall Vital Sign Detection Using RF Cancellation

After quantifying the SNR degradation, another vital sign detection test was conducted to verify the effect of automatic RF cancellation technique. The setup is shown in Fig. 4.9 where the same wooden wall was used in between the subject and the RF system. The subject was asked to sit 2 meter away from the radar system and to wear an oximeter sensor to provide a reference data for heart rate information to be compared with radar measured results. The same measurement process has been repeated in this scenario where a 130-s test was performed. After 65 seconds, the automatic RF cancellation was triggered and applied to cancel the coupling waveform.

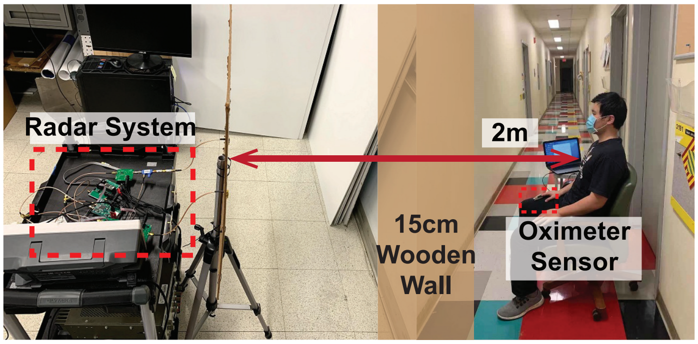

Figure 4.9: Through-wall measurement setup with a subject sitting 2 m away from the radar system. The obstruction consists of a 15-cm wooden wall in a California school building.

Similarly, the Fig. 4.10 (a) (b) (c) display the 20-s time domain waveform, spectrum of output waveform before and after RF cancellation respectively. The figure shows the RF cancellation effect in both time and frequency domain where the automatic RF cancellation process takes around 2.4 s and the SNR gets improved by at least 15-dB with an RF cancellation depth of 40.2 dB. The vital sign detection accuracy is verified in Fig. 4.11 where (a) and (b) are the spectrogram with 20-s time domain window before and after automatic RF cancellation process. The oximeter reference overlays on top of the two

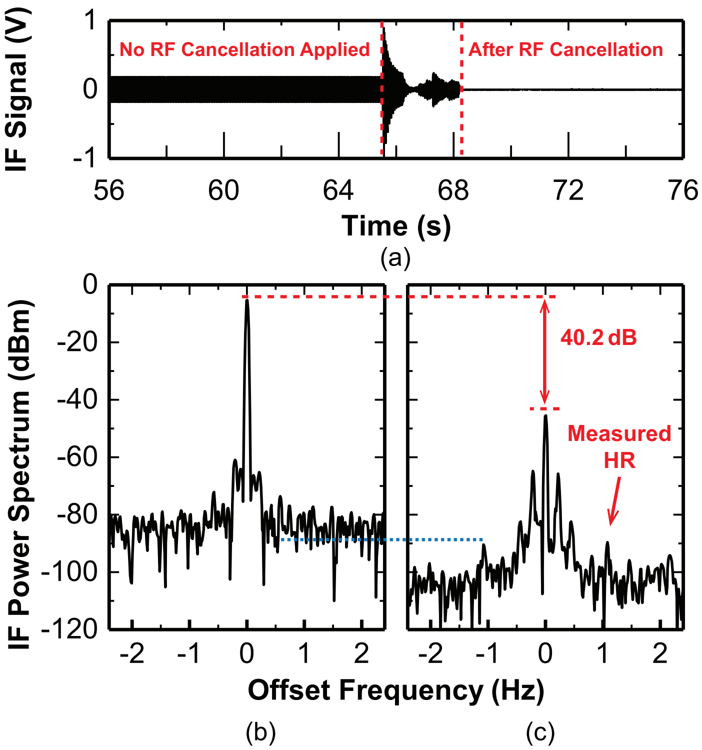

Figure 4.10: Measurement result from through-wall vital sign detection. (a) 20-second time domain waveform that shows the RF cancellation process (b) Frequency domain analysis without RF cancellation. (c) Frequency domain analysis after applying RF cancellation.

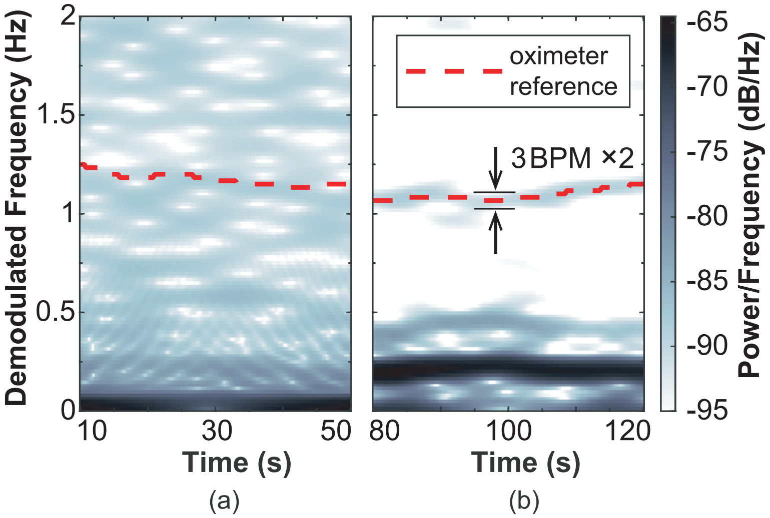

Figure 4.11: 60-s spectrogram based on the demodulated baseband signal resulted from the through-wall vital sign detection. (a) Before applying RF cancellation (b) After applying automatic RF cancellation.

spectrogram. This leads to an observation that the true HR spectrum is buried under the phase noise before cancellation applied in (a) whereas the HR spectrum is clearly identified after automatic RF cancellation applied in (b) where the detected HR always tracks the oximeter reference data across this entire 60-s measurement. As shown in Fig. 4.11 (b), the detected HR of the subject gradually changed from 1.07 Hz to 1.15 Hz with a confidence of 3 BPM difference when comparing with the reference.

4.5 Summary

To reduce the complexity of the implementation, an automatic RF cancellation module is developed by using two micro-controllers. With applying the automatic RF cancellation, the low-IF Dual-PLL system using a pair of patch antennas achieves a sensing range of 4 m with a transmitting power of −31 dBm. Even with using a pair of high-isolation array antennas in a through-wall detection scenario, the automatic RF cancellation can still be effective to improve the system SNR by achieving a 2-m through-wall detection with a −31 dBm transmitting power. In both of these scenarios, the measured HR result is proven to constantly track the reference signal accurately within 3 BPM error. Overall, the system addresses the coupling effect through adopting the automatic RF cancellation and demonstrates a highly competitive sensitivity with using a low transmitting power.

Chapter 5

Coupling Effect to AM and PM inside Doppler Radar System

5.1 Introduction

Phase modulation (PM) has always been considered as the major modulation scheme during the continuous-wave (CW) Doppler radar system used for remote displacement sensing. However, the self-injection-locked (SIL) system, whose output signal is proportional to the small phase variation of the RF waveform, still experiences the null-point effect during the remote detection. This contradicts with the assumption made in the first place. Even though equations have been used to analytically explain this null-point effect in the SIL system, the proof may not be enough to explain the disappearance of the modulation information induced by the motion signal. In this chapter, both a quantitative and a qualitative analysis have been performed to demonstrate the effect of PM converted to amplitude modulation (AM) during the CW Doppler radar system with high coupling involved in the system.

5.2 Modulation Analysis in Doppler Radar System

To date, many papers [18, 21–24, 66] have assumed a constant reflection power level from the target despite the motion variation that causes difference in path loss. In this regard, the PM is considered as the major modulation scheme for the RF reflection signal while the AM from the reflection signal is considered to be negligible. However, Peng [67] held a different perspective while stating that the AM component due to the equation can help the system achieve a high sensitivity and avoid the null-point issue at the same time. To analyze and compare the contributions between AM and PM inside the system, the equations are derived with considering two scenarios: with and without the coupling effect involved in the system.

5.2.1 Analysis without Coupling Effect

The Doppler radar system transmits a CW single-tone signal, $TX(t)$. The signal is partially reflected after it reaches the target at a distance of d, and its phase is modulated by the target movement, $x(t)$. Then the reflection signal gets picked up by the receiver antenna to be considered as $RX(t)$. According to the well-known Friis transmission equation, the amplitude of the reflection signal in far field is proportional to $\frac{1}{d^4}$, this results in waveform equations described as follows:

$$TX(t) = A_t \cos\left(\omega_{RF} t\right), \tag{5.1}$$

$$RX(t) = A_r \left[\frac{d}{d + x(t)}\right]^4 \cos\left[\omega_{RF} t + \frac{4\pi x(t)}{\lambda} + \Delta\phi\right], \tag{5.2}$$

where A_r is the detected signal amplitude when the target is placed at a distance of d and $\Delta\phi$ represents the phase offset caused by the RF signal traveled between the radar system and the target. To compare the contribution between AM and PM inside $RX(t)$, its amplitude information, $A(t)$, and phase information, $\theta(t)$, is obtained as:

$$A(t) = A_r \left[\frac{d}{d + x(t)}\right]^4, AM_{index} = \frac{2x_{max}}{d} \tag{5.3}$$

$$\theta(t) = \frac{4\pi x(t)}{\lambda} + \Delta\phi, \quad PM_{index} = \frac{2\pi x_{max}}{\lambda}. \tag{5.4}$$

where x_{max} represents the peak-to-peak value of the assumed sinusoidal motion trajectory. In this analysis, we use the modulation index to estimate the modulation contributions during the motion detection with using AM_{index} and PM_{index} to represent the modulation index for AM and PM respectively. In frequency spectrum, the modulation index indicates the difference between the fundamental side-band power level induced by the motion signal and the RF carrier power. When comparing between AM_{index} and PM_{index}, the

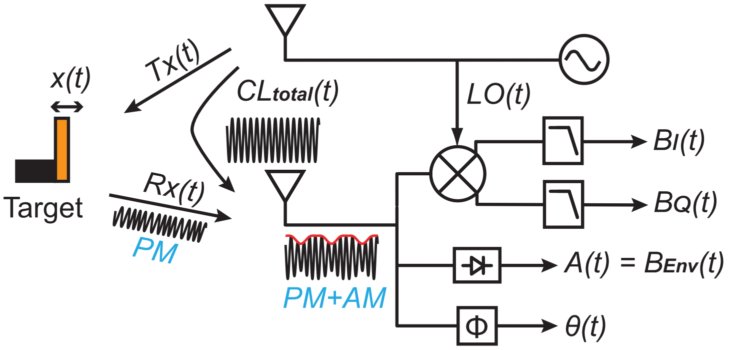

Figure 5.1: Diagram for the Doppler radar system with considering coupling effect.

PM is reported to dominate the modulation scheme if $d \gg \frac{\lambda}{\pi}$. This condition is easily satisfied with a far-field detection distance requirement of more than 1 m and an operating frequency of 2 GHz. Therefore, it suggests that the motion information is mainly stored in the form of PM involved in the RF signal while the reflection signal strength can be treated as a constant value, A_r. This aligns with the motivation behind many developed system architectures, which is to detect PM of the returned RF signal.

5.2.2 Coupling Signal Representation

Any signal path from TX to RX with a constant phase shift is considered as a source of coupling. It includes the TX-to-RX antenna coupling, board coupling and the clutter reflection from any stationary object. By summing up all the coupling sources, the total coupling representation can be shown as:

$$CL_{total}(t) = \sum_{N=1}^{n} A_N \cos\left(\omega_{RF} t + \phi_N\right) \tag{5.5}$$

where each coupling source can be represented using a cosine function with a different amplitude, A_N, and phase offset, ϕ_N. After applying the trigonometric identity, the summation can be further simplified to a single cosine equation with a constant amplitude and phase defined as A_{CL} and $\phi_{CL} + \Delta\phi$ respectively. The equation is now updated as:

$$CL_{total}(t) = A_{CL} \cos\left(\omega_{RF} t + \phi_{CL} + \Delta\phi\right) \tag{5.6}$$

where ϕ_{CL} is defined as the phase difference between the total coupling and the target reflected signal.

5.2.3 Amplitude Modulation with Coupling

After taking account the coupling effect modeled in (5.6), the received signal representation from (5.2) is now modified to:

$$\begin{aligned} RX_C(t) = & A_r \cos\left[\omega_{RF}t + \frac{4\pi x(t)}{\lambda} + \Delta\phi\right] \\ & + A_{CL}\cos\left(\omega_{RF}t + \phi_{CL} + \Delta\phi\right) \end{aligned} \tag{5.7}$$

where $\Delta\phi$ will be set to 0 in the following analysis for simplicity without affecting the derivation. Then, the updated amplitude information, $A_C(t)$, and the phase information of the total received signal with coupling, $\theta_C(t)$, are derived as:

$$A_C(t) = \sqrt{A_{CL}^2 + A_r^2 + 2A_rA_{CL}cos\left[\frac{4\pi x(t)}{\lambda} + \phi_{CL}\right]}, \tag{5.8}$$

$$\theta_C(t) = \arctan\left[\frac{A_rsin\left[\frac{4\pi x(t)}{\lambda}\right] + A_{CL}sin(\phi_{CL})}{A_rcos\left[\frac{4\pi x(t)}{\lambda}\right] + A_{CL}cos(\phi_{CL})}\right]. \tag{5.9}$$

Instead of a constant power level assumed for the target reflection signal analyzed in Sec.5.2.1, the equation (5.8) indicates that there is another AM contribution introduced to the modulation scheme inside the total received signal. The contribution level of such AM is comparable with that of PM with both associated with the value of ϕ_{CL}. Similar to I and Q signals that are always quadrature to each other, these AM and PM contributions are complementary to each other which means that when AM is at the null point, PM always operates at its optimum point.

To support the above statement, the conditions for the null point and the optimum point of AM and PM are derived. Since the first derivative of (5.8) and (5.9) respective to the motion signal, $x(t)$, represents the conversion gain between the motion variation to the amplitude and phase variation, the null point happens when the conversion gain is set to zero. After applying this condition, i.e. $\frac{d}{dx(t)}A_C(t) = 0$ or $\frac{d}{dx(t)}\theta_C(t) = 0$, we can identify the values of $\phi_{CLPMNull}$ or $\phi_{CLPMNull}$ which is the condition for ϕ_{CL} that leads to the null-point operation for AM or PM during the system as:

$$\phi_{CLAMNull} = n\pi, \tag{5.10}$$

$$\phi_{CLPMNull} = \begin{cases} 2n\pi \pm cos^{-1}\left(-\frac{A_r}{A_{CL}}\right), A_r \leq A_{CL} \\ Not\ Applicable \qquad\quad, A_r > A_{CL} \end{cases}, \tag{5.11}$$

where n belongs to the set of integers. The equation (5.10) indicates that the null point for AM happens when the phase of the coupling aligns with the reflection signal, i.e. $\phi_{CLAMNull}$ is equal to integer multiple of π. On the other hand, according to (5.11), the null point for PM only happens when $A_r \leq A_{CL}$ where $\phi_{CLPMNull}$ depends on the relative magnitude level between A_r and A_{CL}. Therefore, when there is little coupling, i.e. $A_r > A_{CL}$, no null-point effect is involved in PM. Once A_{CL} surpasses A_r, the PM null point starts to show up when $\phi_{CL} = 180^o$ and its value changes with repective to $\frac{A_{CL}}{A_r}$. As A_{CL} further increases relative to A_r, $\phi_{CLPMNull}$ approaches to 90^o.

The optimum points for AM and PM can be derived by setting the second derivative of (5.8) or (5.9) to zero with $\frac{d^2}{dx^2(t)}A_C(t) = 0$ or $\frac{d^2}{d^2x(t)}\theta_C(t) = 0$. This finds the $\phi_{CLAMOpt}$ or $\phi_{CLPMOpt}$ which locally maximizes the conversion gain that translates the motion information to variation in the form of AM or PM. The derived results are shown below:

$$\phi_{CLAMOpt} = 2n\pi \pm cos^{-1}\left(-\frac{min(A_{CL}, A_r)}{max(A_{CL}, A_r)}\right), \tag{5.12}$$

$$\phi_{CLPMOpt} = n\pi. \tag{5.13}$$

where it is found that $\phi_{CLAMOpt} = \phi_{CLPMNull}$ and $\phi_{CLPMOpt} = \phi_{CLAMNull}$. This clearly shows a complementary relationship between the AM and PM inside the system.

To further assess and compare the contribution between AM and PM, the conversion gain at their optimum points are determined to be:

$$\left|\frac{d}{dx(t)}A_C(t)|_{\phi_{CL}=\phi_{CLAMOpt}}\right| = \frac{4\pi min(A_{CL}, A_r)}{\lambda}, \tag{5.14}$$

$$\left|\frac{d}{dx(t)}\theta_C(t)\right| = \begin{cases} \frac{4\pi A_r}{\lambda(A_{CL}+A_r)}, \phi_{CL} = 2n\pi \\ \frac{4\pi A_r}{\lambda|A_{CL}-A_r|}, \phi_{CL} = (2n+1)\pi \end{cases}. \tag{5.15}$$

where all AM optimum points share the same conversion gain while there are two different conversion gain values at PM optimum points that locally maximize the motion detection sensitivity. With the above conversion gain equation, it leads to the updated modulation index for AM and PM, AM_{Cindex} and PM_{Cindex}, specified as follows:

$$AM_{Cindex} \approx \frac{2\pi min(A_r, A_{CL})x_{max}}{\lambda\sqrt{|A_{CL}^2 - A_r^2|}}, \tag{5.16}$$

$$PM_{Cindex} \approx \begin{cases} \frac{2\pi A_r x_{max}}{\lambda|A_{CL}+A_r|}, \phi_{CL} = 2n\pi \\ \frac{2\pi A_r x_{max}}{\lambda|A_{CL}-A_r|}, \phi_{CL} = (2n+1)\pi \end{cases}, \tag{5.17}$$

where a small motion displacement, x_{max}, is assumed for reaching these results. The above modulation index equations are generalized forms of (5.3) and (5.4) with additional consideration of the coupling effect, with $AM_{Cindex} = AM_{index}$ and $PM_{Cindex} = PM_{index}$ when $A_{CL} \ll A_r$. After introducing the coupling effect, based on (5.16), AM_{Cindex} is reported to increase as A_{CL} gets larger. While $A_{CL} < A_r$, the contribution from AM is always smaller than that of PM indicated in (5.17). As A_{CL} further elevates and exceeds A_r, AM_{Cindex} and PM_{Cindex} become comparable and almost the same when $A_{CL} \gg A_r$. This reveals that at the null point of PM, the motion information is majorly converted to AM caused by the coupling effect and this AM is not related to the path loss variation.

Noted that the modulation index, AM_{Cindex} or PM_{Cindex}, only describes the modulation depth corresponding to the target motion while it does not represent the resulted voltage variation. To better compare the optimum detected motion signal power due to AM or PM at their optimum point, the motion spectrum power denoted as P_{maxAM} or P_{maxPM} is derived using the modulation index of AM or PM, which is displayed as follows:

$$P_{maxAM} = AM_{Cindex}\sqrt{A_{CL}^2 - A_r^2} \tag{5.18}$$

$$P_{maxPM} = PM_{Cindex}\sqrt{A_{CL}^2 + A_r^2 + 2A_rA_{CL}\cos(\phi_{CL})} \tag{5.19}$$

where the resulted voltage variation is the modulation index scaled with the RF carrier magnitude. When $A_{CL} > A_r$, the motion spectrum power is determined to be $\frac{2\pi A_r x_{max}}{\lambda}$ for both P_{maxAM} and P_{maxPM}. This further proves the complementary relationship between the AM and PM where it indicates the motion information is transferred in-between these two modulation schemes as ϕ_{CL} changes.

To verify the complementary relationship and the null point prediction for AM and PM analyzed during this section, a MATLAB simulation is conducted to analyze the motion spectrum due to AM or PM with change of ϕ_{CL}. During the simulation, two signal waveform representing the coupling and the reflection signal respectively are generated with $\omega_{RF} = 1\,\text{KHz}$. The reflection signal contains PM with $PM_{index} = 0.0873$, which corresponds to a 11–mm peak-to-peak motion detected by a system operating at 2.4 GHz. After adding up the coupling and the reflection signal, the amplitude and phase information of the combined waveform are extracted to be processed as the motion power spectrum caused by AM and PM respectively. With sweeping ϕ_{CL} across the whole range, the detected motion spectrum power resulted from AM or PM changes accordingly with their results displayed in Fig. 5.2.

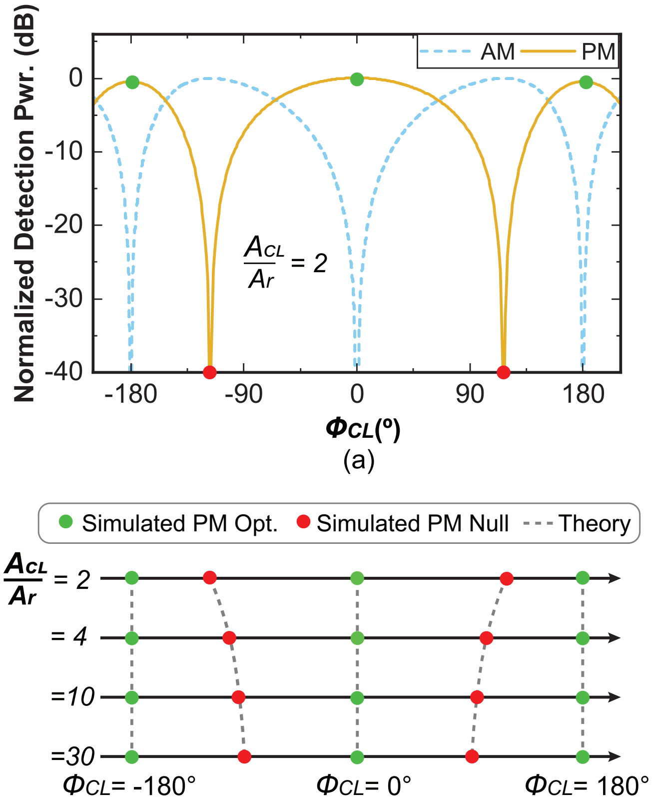

(a)

(b)

Figure 5.2: MATLAB simulation results with (a) Normalized baseband motion detection power at the fundamental frequency in the form of AM and PM with $A_{CL} = 2A_r$, (b) Comparison between the simulation results of the PM operating-point positions with theoretical predictions considering four scenarios with $\frac{A_{CL}}{A_r}$=2,4,10 and 30.

Fig. 5.2 (a) represents the normalized detection power demodulated from AM and PM separately with sweeping ϕ_{CL} from -210^o to 210^o with a step size of 1^o. $\frac{A_{CL}}{A_r} = 2$ is set for this simulation, which yields $\phi_{CLPMNull} = \pm 120^o + n \cdot 360^o$ and $\phi_{CLPMOpt} = n \cdot 180^o$ according to (5.11) and (5.13). These predictions perfectly agree with the simulation results observed from Fig. 5.2 (a). This plot justifies the complementary relationship between AM and PM involved in the combined waveform. To further verify the dependency between the null-point position and the relative coupling magnitude predicted from (5.11), Fig. 5.2 (b) compares between the theoretical and the simulated operating conditions positions with sweeping $\frac{A_{CL}}{A_r}$. The results show that the PM null-point position indeed moves towards 90^o as the coupling signal becomes bigger while the optimum points stay at $n\pi$. All the operating-point positions agree with the theory predictions within 1^o due to the discrete step size of ϕ_{CL} adopted for the simulation.

5.2.4 Interpretation of AM and PM in IQ Plot

IQ plot is a popular method for interpreting the phase and amplitude information carried by an RF waveform. It has been used for demonstrating various effects in the demodulation process, e.g. the I/Q imbalance effect in [53], effect of using different estimation algorithms in [51] and the radius calibration demodulation technique in [68]. In this section, we will use the IQ plot to interpret the AM and PM contribution inside the total received waveform. To first obtain the baseband I and Q signals, the setup during Fig. 5.1 is assumed where $cos(\omega_{RF}t + \Delta\phi)$ is considered for $LO(t)$. This setup down-converts the total received signal, $RX_C(t)$ from (5.7) to the demodulated $B_I(t)$ and $B_Q(t)$ specified as:

$$B_I(t) = \frac{A_r}{\sqrt{2}} sin\left[\frac{4\pi x(t)}{\lambda} + \Delta\phi\right] + \frac{A_{CL}}{\sqrt{2}} sin(\phi_{CL} + \Delta\phi), \tag{5.20}$$

$$B_Q(t) = \frac{A_r}{\sqrt{2}} cos\left[\frac{4\pi x(t)}{\lambda} + \Delta\phi\right] + \frac{A_{CL}}{\sqrt{2}} cos(\phi_{CL} + \Delta\phi). \tag{5.21}$$

While the I/Q signals are used as a set of Cartesian coordinate for constructing an IQ constellation plot, the amplitude and phase information is considered to serve as a set of polar coordinates for the IQ plot. This means that any movement in angular or radial direction on an IQ plot corresponds to the amplitude or phase variation involved in the received signal.

A series of IQ plots are presented in Fig. 5.3 where the path loss variation due to the target motion is neglected. Fig. 5.3 (a) first describes the ideal scenario that does not involve any coupling effect with $A_{CL} = 0$. The arc $\widehat{AB}$ represents the voltage variation caused by the target motion. In this plot, $\widehat{AB}$ only lies in the angular direction of $\hat{\theta}$ while its amplitude always maintains the same throughout the variation with $\overline{AC} = \overline{BC}$. This indicates the detected motion is mostly embedded in the received signal through PM. Once we introduce coupling to the system, it begins to shift the center of the received signal from Point C to Point D as shown in Fig. 5.3 (b). From the IQ plot, we can also tell that $\widehat{AB}$ does not only lie in $\hat{\theta}$ but also partially in radial direction. With $\overline{AC} \neq \overline{AB}$, it indicates that there is additional AM involved in the RF received signal simply by introducing the coupling.

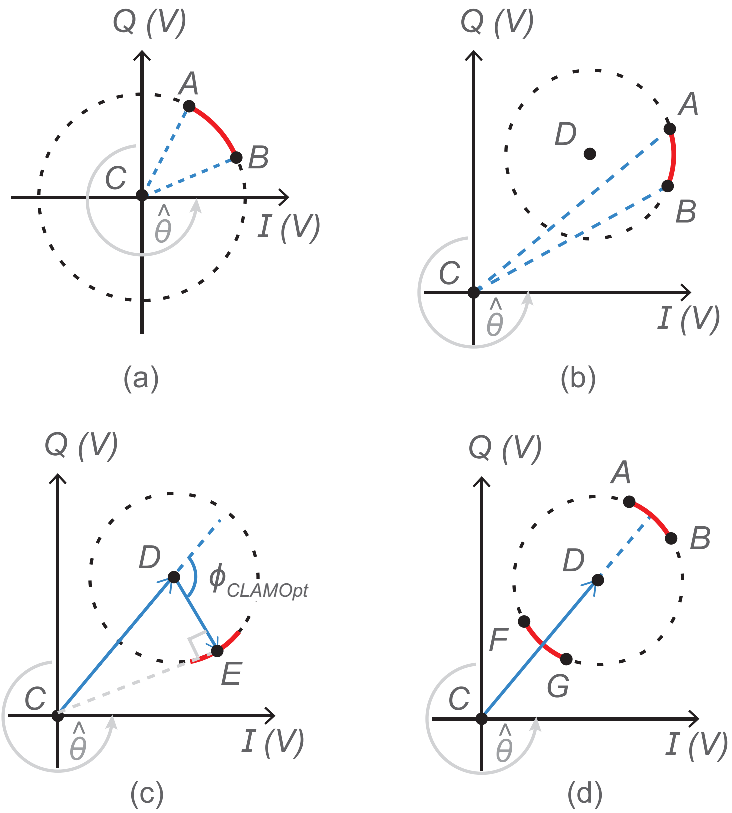

(a) (b) (c) (d)

Figure 5.3: IQ plots when coupling signal is at different levels. (a) No coupling signal considered (b) With coupling signal involved in the system (c)Scenario when AM is at its optimum point (d) Scenario when PM is at its two optimum points

To verify the null point and the optimum point conditions for AM and PM derived in (5.10), (5.12), (5.11) and (5.13), the optimum-point scenario for AM and PM are illustrated in Fig. 5.3 (c) and (d) respectively. In Fig. 5.3 (c), the motion arc is shown to always lie in the radial direction at the AM optimum point on an IQ plot. This is because when $\phi_{CL} = \phi_{CLAMOpt}$, $\overrightarrow{\mathrm{CE}}$ forms a right angle with $\overrightarrow{\mathrm{DE}}$, which aligns the tangential direction of the circle at Point E with the radial direction in the IQ plot. Therefore, when the motion arc moves around at point E, the motion information mostly translates to AM embedded inside the received signal. On the other hand, for the optimum-point scenario of PM shown in Fig. 5.3 (d), the motion arc always lies in $\hat{\theta}$, which corresponds to PM for the received signal while the variation in the radial direction is limited. Note that there are 2 optimum point scenarios that are different in distance away from the center. These two PM optimum points do not generate the the same motion variation corresponding to the same change in $\hat{\theta}$. More specifically, $\widehat{FG}$ experiences a bigger variation in $\hat{\theta}$ to obtain a higher PM index comparing with $\widehat{AB}$. However, due to the same length of the motion arc, the motion spectrum power obtained from these two PM optimum points is ended up to be the same. Overall, these four graphs serve as an analogy to back up the theories derived previously in this section.

5.3 Range Correlation Effect in AM

After analyzing the additional AM resulted from the coupling effect, the AM noise analysis is carrier out in this section to estimate the feasibility of AM detection using a linear envelope detector. Ideally, the envelope detector is immune to any phase noise involved in an RF waveform as the phase and amplitude information of the same waveform are orthogonal. Due to the PM to AM conversion effect analyzed in the previous section, it is necessary to quantify how much phase noise is also converted to the signal amplitude, contributing to the resulted output SNR. Therefore, to understand the noise level of such AM signal, the noise analysis of the converted AM signal is conducted. With the phase noise from the RF signal source, $\phi_n(t)$, added to the analysis, the received signal equation from (5.7) is now updated to the following expression:

$$\begin{aligned} RX_{pn}(t) = A_r \cos\left[\omega_{RF}t + \frac{4\pi x(t)}{\lambda} + \phi_n(t - t_{dr})\right] \\ + A_{CL}\cos\left[\omega_{RF}t + \phi_{CL} + \phi_n(t - t_{dCL})\right] \end{aligned} \tag{5.22}$$

where t_{dCL} and t_{dr} represent the time delay of the coupling and the reflection signal respectively with both relative to $TX(t)$. After passing through an ideal envelope detector, the demodulated amplitude signal, $B_{Env}(t)$, is derived in (5.23) where its residual amplitude noise is determined by the cosine function with phase subtraction between the phase noise of the coupling and the reflection signals.

$$B_{Env}(t) = \sqrt{A_r^2 + A_{CL}^2 + 2A_rA_{CL}\cos\left[\frac{4\pi x(t)}{\lambda} - \phi_{CL} + \phi_n(t - t_{dr}) - \phi_n(t - t_{dCL})\right]} \tag{5.23}$$

This indicates that the resulted amplitude noise converted from the RF phase noise also goes through the same range correlation effect (RCE) following the equation from [69] that:

$$S_{\Delta\phi}(f) = S_\phi(f) \times 4sin^2[\pi f \cdot \Delta t_d], \tag{5.24}$$

where the residual noise spectral density, $S_{\Delta\phi}(f)$, is reduced from the RF phase noise spectral density, $S_\phi(f)$, depending on the time delay difference between the two waveform adding with each other, Δt_d. Therefore, with using an ideal envelope detector, the demodulated AM signal also benefits from RCE, which makes it ideally possible to achieve a similar SNR level comparing with the I and Q signal obtained during the conventional Doppler radar system.

This noise suppression effect between the RF signal phase noise to the resulted amplitude noise is simulated in MATLAB with its results presented in Fig. 5.4. In this simulation, a sampling frequency of 1 GHz is used to model $RX_{pn}(t)$ with $\omega_{RF} = 10\,\text{MHz}$ for a total time of 10 ms. Both the coupling and the reflection signal are modeled in the simulation with $A_{CL} = 2A_r$. To model the phase noise for the RF waveform, a random-walk data series with a step size of 0.0007 is used to generate $\phi_n(t - t_{dr})$ and $\phi_n(t - t_{dCL})$ with $\Delta t = t_{dCL} - t_{dr}$ randomly chosen to be 1 µs. This leads to an $RX_{pn}(t)$ spectrum with a phase noise level of $-40.8\,\text{dBc}$ at 10-KHz frequency offset and a roll off with a slope of

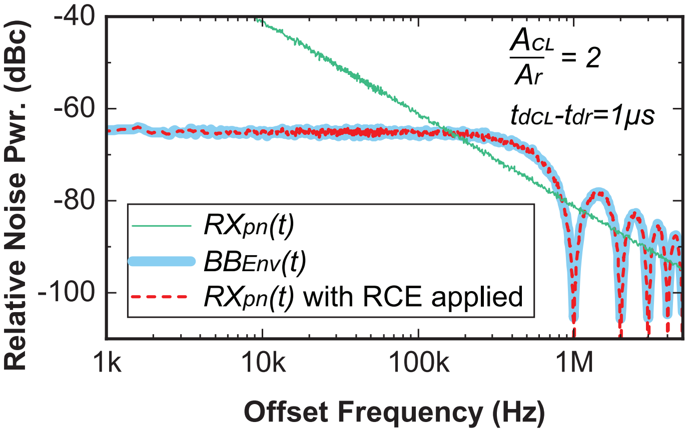

Figure 5.4: Simulated relative noise power comparison among $RX_{pn}(t)$, $B_{Env}(t)$ and the prediction when directly applying the range correlation effect to $RX_{pn}(t)$.

-20 dB per decade as shown in Fig. 5.4. After that, we obtain the amplitude information of $RX_{pn}(t)$ to be $B_{Env}(t)$ where the amplitude level depends on ϕ_{CL}. To maximize the detected amplitude noise inside $B_{Env}(t)$, its noise spectrum is measured at $\phi_{CL} = 120^o$ which is the condition for AM optimum point. Then the noise spectrum is normalized relative to A_r. After repeating this simulation for 200 times to obtain an averaged noise behavior, the simulated amplitude noise of $B_{Env}(t)$ is compared with the expected residual baseband noise after directly applying RCE to $RX_{pm}(t)$. The two curves overlaid on top with each other as shown in Fig. 5.4. Thus, this verifies the range correlation effect involved during the phase-noise-to-amplitude-noise conversion and serves as a foundation for using envelope detector as an effective demodulation method.

To provide a better interpretation of the envelope detection demodulation with respective to the conventional IQ demodulation approach, we further simplify (5.23) to the following equation with assuming $A_{CL} \gg A_r$.

$$B_{Env}(t) \approx A_{CL} + A_r \cos\left[\frac{4\pi x(t)}{\lambda} - \phi_{CL} + \phi_n(t - t_{dr}) - \phi_n(t - t_{dCL})\right] \tag{5.25}$$

With this approximation, $B_{Env}(t)$ is almost equivalent to the I channel output, $B_I(t)$, derived as follows:

$$B_I(t) = A_{CL} + A_r \cos\left[\frac{4\pi x(t)}{\lambda} - \phi_{CL} + \phi_n(t - t_{dr}) - \phi_n(t - t_{dLO})\right] \approx B_{Env}(t) \tag{5.26}$$

where this requires $LO(t)$ to be specified as:

$$LO(t) = 2A_r \cos\left[\omega_{RF}t + \phi_{CL} + \phi_n(t - t_{dLO})\right]. \tag{5.27}$$

The only notable difference between $B_I(t)$ and the approximated $B_{Env}(t)$ is the difference in phase noise time delay. Typically, the time delay of these RF waveform follows $t_{dLO} < t_{dCL} < t_{dr}$ based on the path length taken by these signals. Overall, we can view the ideal envelope detection output as a conventional I channel output after a mixer driven by an RF source that shares the same phase offset with the coupling. In terms of the noise behavior, the ideal envelope detection benefits a potentially higher phase noise suppression due to the shorter delay time difference with $t_{dr} - t_{dCL} < t_{dr} - t_{dLO}$. However, the practical envelope detector has a worse linearity comparing with the passive mixer, which typically results in a limited detection SNR in the actual experiments.

5.4 AM PM Verification Using Low-IF Doppler Radar System

To verify the PM-to-AM conversion theory presented in the previous sections, an experiment using a low-IF Doppler radar system is designed to analyze and compare the motion power spectrum detected by the received RF signal. The measurement system diagram is shown in Fig. 5.5 where the PLL1 and PLL2 generate two RF waveform with frequencies of 2.450001 GHz and 2.45 GHz respectively. Due to the frequency difference, the mixer output results in an IF with a frequency of 1 KHz where it shares the same information of AM and PM from the RF signal. To generate a precisely controlled motion waveform, a linear-stage actuator (LSTG) is placed d meter away from the radar system. The LSTG is programmed to perform 64 sine-wave motion segments with a fixed motion peak-to-peak of 5-mm and a period of 15 seconds each. Similar to the experiment conducted in [68], these motion segments are shifted in space with a 0.625-mm step size in-between the consecutive motion segments, which provides a ϕ_{CL} sweeping range of 235.2^o with a resolution of 3.7^o. Two 2×2 array patch antennas are adopted to the system for reducing the antenna coupling strength.

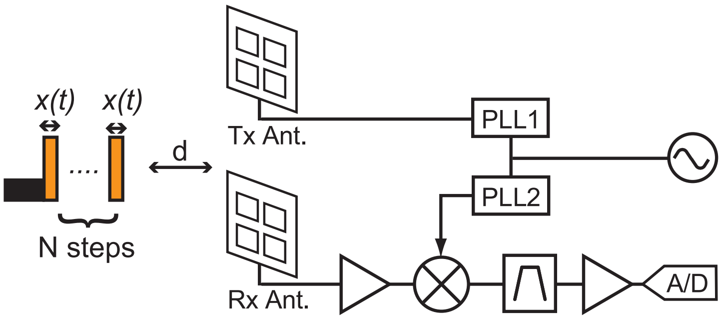

Figure 5.5: System diagram for AM PM effect validation using a dual-PLL low-IF system.

Two experiments are conducted with different distances between the LSTG and the radar system: 0.6 m and 2 m. The close-in detection is expected to mainly receive the target reflection signal with limited coupling, i.e. $A_r > A_{CL}$. On the other hand, with decrease in the reflection signal power by extending the separation distance to 2 m, $A_r < A_{CL}$ is expected. The measurement results obtained from the two scenarios are displayed in Fig. 5.6 where the motion spectrum power due to AM and PM are extracted to be compared throughout the change in ϕ_{CL}. Since there is no null-point issue involved in the IF system, the AM-and-PM-combined motion spectrum detected from IF is measured to be invariant within a 1–dB difference regardless of the ϕ_{CL} value. With increasing the detection distance from 0.6 m to 2 m, the detected AM-and-PM-combined motion power is measured to decrease by 19.1 dB and is also invariant within 0.3 dB no matter the change in ϕ_{CL}.

For the close-in scenario, the magnitude ratio between the coupling and the reflection signal is determined to be $\frac{A_{CL}}{A_r} = 0.13$. This minor coupling effect greatly reduces the AM contribution involved in the signal modulation according to (5.18) where this predicts a 17.7-dB difference from the optimal PM motion power calculated from (5.19). This agrees with the measurement result of 18.2 dB in difference between PM and AM optimum point reported from Fig. 5.6 (a). Another observation from this measurement result is that the AM component contributed from the path loss equation does not resolve the null-point effect for close-in motion detection. The 0.6–m detection distance places the target within the near-field region of the antenna, which makes the prediction from (5.3) invalid. Based on the measurement results, the AM component still results in a 43.2-dB null point when

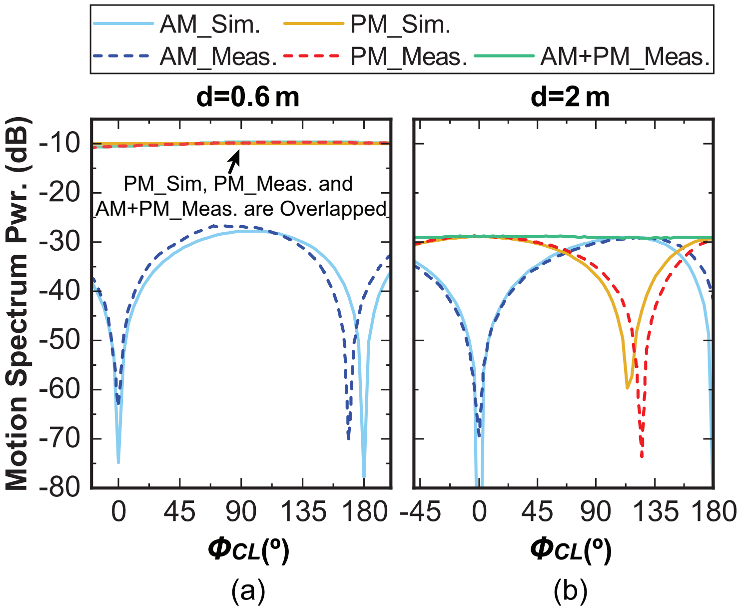

Figure 5.6: Measured motion spectrum power resulted from the AM and PM involved in the signal with a separation distance of (a) d=0.6 m and (b) d=2 m

.

$\phi_{CL} = 169^o$. This directly proves that the phase modulation is still dominant even if the target is placed within the near-field region of the detection system.

On the other hand, the 2-m detection scenario results in a lower reflection power level with $\frac{A_{CL}}{A_r} = 2.1$. According to (5.11), this leads to a PM null point at $\phi_{CL} = 118.6^o$. When comparing with the measurement result reported from Fig. 5.6 (b), the measured PM null point is found when ϕ_{CL} is 125^o, yielding an insignificant error of 6.4^o. As for the comparison between the optimal motion power from AM and PM in this scenario, the measurement only shows a 1-dB difference between the two modulations at their optimum points. This concludes that the initial Doppler effect on the phase modulation of the reflection signal is now embedded into both the AM and PM in the received RF signal after introducing a large coupling effect. Therefore, the motion information from the Doppler effect during the experiment can only be fully acquired if both amplitude and phase information of the RF signal is acquired.

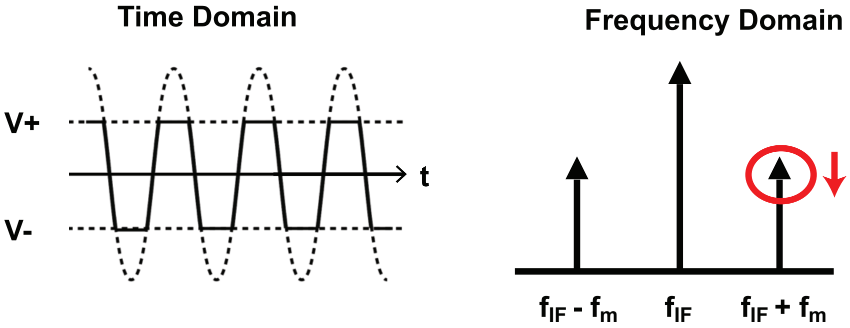

Figure 5.7: Example of a saturated IF signal in time domain and frequency domain.

5.5 Null-point Issue Involved in IF System Architecture under Saturation

The AM-PM complementary relationship provides insight to the null point effect inside the IF system architecture. The reason why this single-channel IF output is immune to the null-point issue at the first place is its detection of both the amplitude and phase information from the received RF signal. Thus, the IF signal preserves all the motion information which are stored in both AM and PM due to the coupling effect.

On the other hand, this interpretation also indicates that that an IF system can also experience the null-point effect if the receiver operates under saturation, which is an common issue experienced by such system due to its high dynamic range requirement. The IF signal is clipped by the voltage supply of the OpAmp at the baseband as demonstrated in Fig. 5.7. Even if a band-pass filter centered at IF frequency is placed at the output of the receiver to avoid the high harmonic content from the saturated IF waveform, the amplitude information is mostly missing from the waveform which leads to the null point issue due to only the PM detection of from the received RF signal. This directly reduces the motion spectrum power labeled in the frequency spectrum of an IF signal indicated in Fig. 5.7.

This effect has been simulated using MATLAB to analyze the relative motion magnitude with respective to the motion signal phase offsets and the relative coupling strength. During the simulation, two IF signals are created to represent the target reflection signal

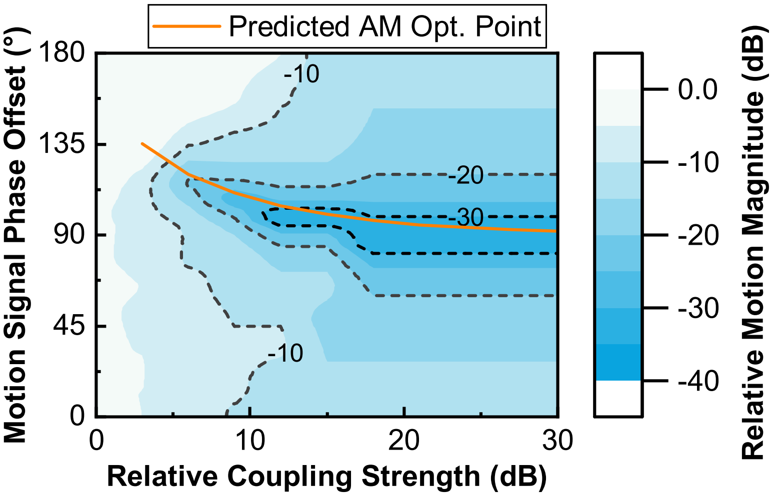

Figure 5.8: MATLAB simulated results on the relative motion magnitude considering different motion signal phase offsets and relative coupling strength under saturation.

and the coupling signal respectively. The two signals first get combined and processed by applying the clipping effect. The threshold level for the clipped voltage (alternatively, the simulated voltage supply of the OpAmp) is set to be the same as the magnitude of the target reflection signal. After that, FFT is applied to the modified waveform to find out the motion spectrum power at the frequency of $f_{IF} \pm f_m$. This step is repeated with sweeping across different motion signal phase offsets and the relative coupling strengths. The results are presented in Fig. 5.8 where the phase offset is swept across 0^o to 180^o with a 1^o resolution and the coupling is swept from 0 dB to 30 dB with a step size of 5 dB.

Instead of a constant motion magnitude expected from the ideal case where the coupling magnitude only increases the IF power without affecting the motion power magnitude, Fig. 5.8 shows that the clipping effect within the saturated IF waveform also reduces the level of the motion power. This is expected due to its reduced sensitivity to the AM detection. We also predict the null point conditions of the saturated IF receiver by adding the AM optimum point conditions due to the coupling effect to Fig. 5.8. The prediction aligns well with the null point conditions identified from the simulation results.

5.6 Summary

Modulation analysis in Doppler radar has been studied in this section where PM is identified as the major modulation scheme when coupling effect is avoided and a combination of AM and PM constitutes the modulation scheme of the received RF waveform when the coupling strength is greater than that of the target reflection signal.

Theoretical calculation and simulation have been carried out to predict the null point and optimum point conditions for the AM and PM within the received waveform. The interpretation of such effect has been verified and interpreted using illustrations of IQ plots. Followed by that, experiments have been conducted to verify the AM and PM relationship with measuring a controlled displacement produced by a linear-stage actuator.

Finally, an analysis of the null point issue in a saturated receiver has been conducted based on the modulation analysis where the saturated receiver has a reduced sensitivity on AM. Therefore, the receiver under saturation can only measure the motion information stored in PM instead of AM, which creates a null point at AM optimum point conditions. A MATLAB simulation has been performed to verify with the proposed analysis where the results demonstrate a degradation in motion spectrum power where the null point condition aligns with the AM optimum point condition predicted by the developed theory.

Chapter 6

Proposed Novel ENVSIL Radar for Remote Displacement Sensing

The SIL system has been developed and gained popular interests from researchers in recent years due to its high detection sensitivity. However, the SIL system suffers from the non-linearity issue reported by Wang in [12] when measuring a large displacement motion. Wang proposed a new architecture that uses an I/Q mixer and a time modulated phase shifter to demodulate the true target displacement with using an SIL VCO source. In this section, ENVSIL with a simpler architecture for displacement sensing is proposed without using any long delay line, phase shifter or mixer in the system. Thus, it can greatly reduce the power requirement for the system operation condition.

6.1 ENVSIL Radar Architecture

The fundamental theory behind the SIL system is its resulted frequency variation due to the signal phase shift happening inside the VCO tank. If the phase alteration of the tank signal, I_T, is small enough, the resulted frequency shift will be linearly proportional to the PM occurred at the VCO tank based on the VCO stability condition. Because I_T at the VCO tank consists of the target reflection signal I_{inj}, the coupling $I_{coupling}$ and the oscillator output I_{osc}, the PM induced by the target motion which is embedded in I_{inj} does not equate to the PM of I_T inside the VCO tank as discussed in the previous sections. Therefore, both AM and PM need to be measured for I_T to achieve the motion

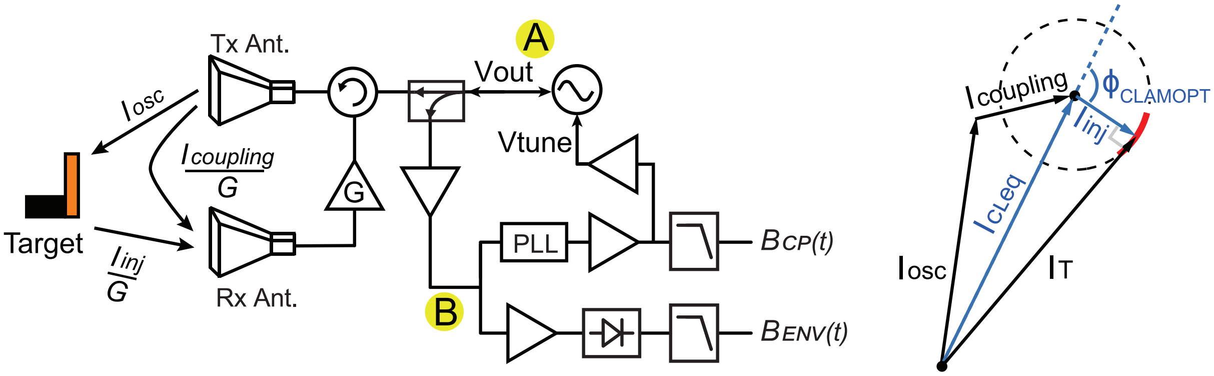

(a) (b)

Figure 6.1: (a) System diagram for the proposed displacement sensing system (b) vector diagram for SIL system at null point

detection without experiencing the null-point issue. Thus, it leads to the proposed system architecture where it detects both AM and PM inside the system.

This new architecture is named as ENVSIL system since it combines both the SIL and the envelope detection system architecture. The system diagram is shown in Fig. 6.1 (a) where part of I_T is split through a 20-dB directional coupler followed by the linear RMS RF detector and the PLL IC. This design intends to detect the AM and PM information which leads to $B_{CP}(t)$ and $B_{ENV}(t)$ at the baseband output respectively. Benefiting from this additional amplitude detection of the tank signal, it is expected that during the null point of the SIL operation shown in Fig. 6.1 (b), the envelope detector will operate at its optimum performance. When these two signals are orthogonal to each, they can be used to demodulate the motion displacement information by constructing an IQ plot.

6.1.1 Design Challenges for ENVSIL Radar

To ensure the proper operation of the displacement sensing system, three factors are considered in this system design:

1) Orthogonality between the AM and PM performance of the VCO. As mentioned in [53] that the mixer used in the conventional Doppler radar system can create I/Q imbalance issue, it results in distortion in the curvature formed by the detected signal. Therefore, instead of the ideal circle shape formed in an IQ plot, the demodulated signal results in an elliptical shape. This leads to higher errors after going through the default

demodulation sequence with doing circle fitting followed by the arctangent demodulation process. The orthogonality requirement also applies to the polar coordinate constructed with the phase and amplitude information of the RF signal. That means, when there is only PM appeared in the system, a constant amplitude should be strictly maintained and vice versa. To improve this situation, a cross-coupled VCO design is adopted to limit the output power difference caused by the phase shift inside the tank signal. Besides that, the VCO is designed with multiple bias adjustments to help achieve an optimum operating point.

2) The requirement of constant ϕ_{CL} between I_T and the input of the envelope detector. To ensure the complementary relationship between the amplitude and phase information detected at the baseband, it is important to understand that B_{CP} measures the frequency variation originated at point "A" marked in Fig. 6.1 (a) whereas B_{ENV} reflects on the amplitude information at point "B". To further ensure the orthogonality between B_{CP} and B_{ENV}, the same ϕ_{CL} needs to be achieved at point "A" and "B". If there is an additional part of the reflection signal directly coupled to point "B" due to the mismatch from the VCO output, the complementary relationship between B_{CP} and B_{ENV} will get interfered. In order to address this effect, the operating frequency needs to be tuned so that the same ϕ_{CL} is maintained between point "A" and "B".

3) Coordinate reconstruction with matching between the AM and PM output signals. Unlike the conventional IQ system where both the channel outputs are in the same domain, B_{CP} and B_{ENV} cannot be directly interpreted to PM and AM of the RF signal. Therefore, before detecting the motion displacement, a calibration needs to be performed to determine the coefficients for data scaling to construct a proper IQ plot. Under the assumptions of linear relationships between the two baseband outputs and the amplitude and phase information of the RF signal, four coefficients need to be found to fully recover the signal information at the VCO tank:

$$A(t) = a \cdot [B_{ENV}(t) + b], \tag{6.1}$$

$$\theta(t) = c \cdot B_{CP}(t) + d. \tag{6.2}$$

The effect to the constructed shape in an IQ plot is displayed in Fig. 6.2 where the simula-

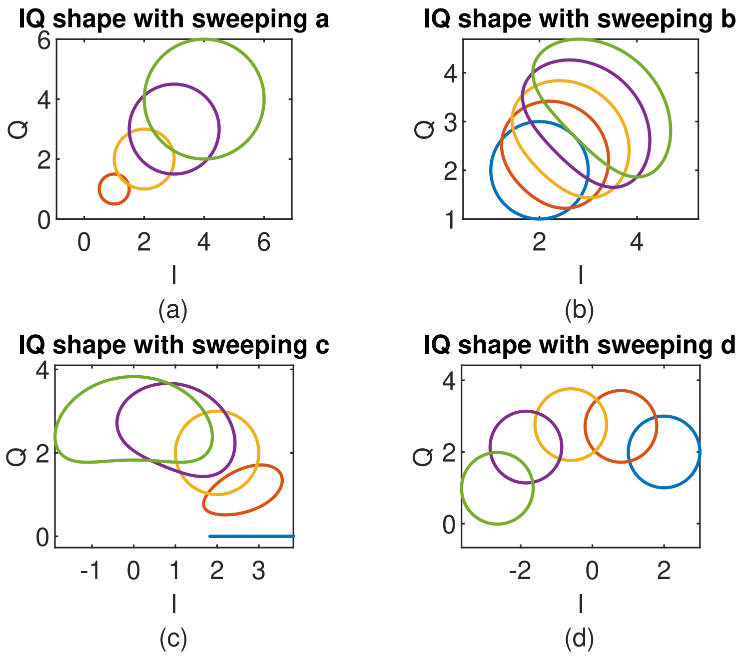

Figure 6.2: Simulated shape on an IQ plot due to the change of (a) coefficient a (b) coefficient b (c) coefficient c (d) coefficient d with sweeping values across: 0, 0.5, 1, 1.5 and 2.

tion is conducted with first assuming B_{ENV} and B_{CP} to represent the true amplitude and phase of the radar waveform. After applying the data scaling mentioned in (6.1) and (6.2), the resulted values are then used for IQ plot construction. The simulation is repeated with only changing one coefficient at a time and each coefficient is swept across the 5 values of 0, 0.5, 1, 1.5 and 2. From Fig. 6.2 (a) and (d), we can see that changes in a and d only decide the size and rotational angle of the constructed shape respectively while maintaining the curvature information of the detected waveform. On the other hand, Fig. 6.2 (b) and (c) demonstrate the curvature distortion when the coefficient values for b and c deviates from its ideal values. As the proper displacement demodulation only requires the curvature information, only b and c need to be carefully determined during the data processing.

6.2 ENVSIL Radar Prototype

Fig. 6.3 shows the complete experimental setup for the the ENVSIL radar. The radar system is constructed using several PCB modules connected through SMA connectors, including the VCO module, the PLL module, the envelope detector module and other peripheral components. All active modules are powered by +6 V power supply through the DC plug connectors. Key components used in the system are listed in Tab. 6.1.

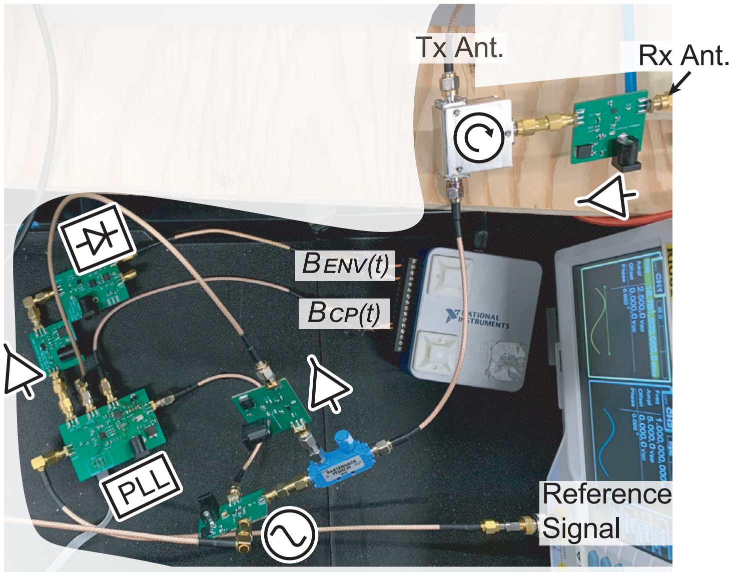

Figure 6.3: Picture of the system setup for the ENVSIL radar

Table 6.1: Key Components Used in the System

Component	Manufacture	Role
ADL5511	Analog Device	RMS Detector
ADL5602	Analog Device	Buffer PA
ADF4159	Analog Device	PLL
BFS481	Infineon	Differential Pair BJT
D3C2327	DITOM Microwave	Circulator
PE2202-20	Pasternack	Directional Coupler
QPL9057	Qorvo	LNA
SMV2201	Skyworks	Varactor Diode
USB6002	National Instrument	ADC

6.2.1 VCO Module Design

Fig. 6.4 shows the font side of the fabricated VCO module where it contains two BFS481 differential pair BJT IC for generating the tail current and the RF oscillation. The PCB layout of the module focuses on symmetry to minimize the difference in loading between two sides of the differential pair. This leads to the placement of varactor diodes on the backside of the board. Due to the high parasitic capacitance from the PCB substrate as well as the balun, the inductor value adopted by the VCO is expected to be small and thus, implemented using a short PCB trace. To further boost the oscillation frequency of the VCO, the decoupling capacitor on the feedback path is reduced. After optimizing the design values, the free-running VCO operates at 2.03 GHz with an output power level of +1 dBm. The VCO output is connected to the TX antenna through a 20-dB directional coupler and a circulator. This connection in-between lowers the output power to −2 dBm before it gets transmitted through the TX antenna.

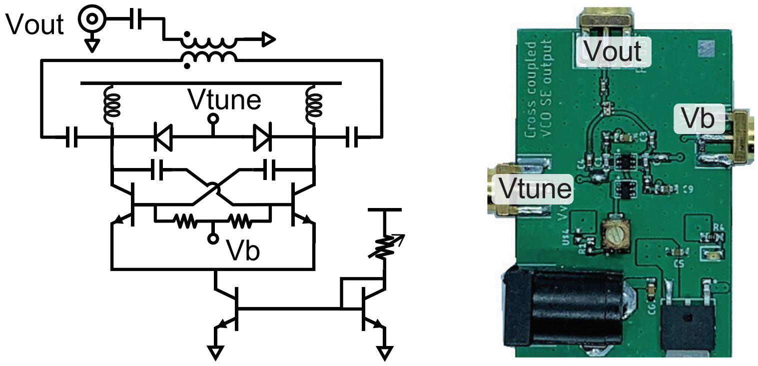

(a) (b)

Figure 6.4: (a) Circuit diagram and (b)Photograph of the designed cross-coupled VCO module.

6.2.2 PLL Module Design

The PLL module consists of the PLL design and the level shifting amplifier design. The PLL module first splits the RF input into two paths by an integrated power splitter with a 7-dB insertion loss. After that, one splitter output connects to the RF input port of the ADF4159 PLL IC input for PM demodulation. The other output connects to the envelope detector through a 10-dB-gain buffer amplifier. With the -10 dBm RF input power requirement for the PLL operation, this greatly reduces the power level requirement in the system.

To improve the sensitivity in frequency adjustment, a DC level shifting amplifier with a gain of 1/6 is adopted in series with the loop filter. This converts the voltage swing from the charge pump output between 0 and 3.3 V to a voltage variation within 0.5 V centered at any DC bias voltage for VCO frequency control. This adjustment helps with both increasing the PM detection sensitivity and compensating the frequency drift caused by the coupling.

6.2.3 Other Module Design

The envelope detector module consists of an ADL5511 RMS detector followed by an AD8628 chopper amplifier for further baseband amplification while minimizing the impact from the baseband flicker noise. The LNA module contributes to an 18-dB gain to compensate the coupling loss at the coupled port of the directional coupler. Another LNA module with the same gain is used to amplify the reflected signal before getting injected into the VCO tank through the circulator. As for the TX and RX antenna, two commercial horn antennas are used with a 12 dBi gain and a 38^o beamwidth specified at the frequency of 2 GHz.

6.3 Coordinate Reconstruction

One unique issue that the ENVSIL radar experiences is the coordinate reconstruction where the two output voltages at the baseband need to be re-scaled to properly construct an IQ plot. As mentioned in Sec.6.1.1, the coefficients, b and c, need to be determined for maintaining the curvature of the original IQ result to be further demodulated for the displacement information. Therefore, a data-based analytical approach and an optimization approach are studied and compared for their effectiveness in finding the right coefficients for the proper coordinate reconstruction.

6.3.1 Data-based Analytical Approach

The distortion effect caused by the coefficients b and c in ENVSIL radar is similar to that caused by the amplitude and phase imbalance issue involved in the conventional IQ radar system. Therefore, the data-based analytical approach (DBAA) developed in [53] has been referred to as the analytical approach for b and c derivation in this paper. The objective for this analytical approach is to solve for the coefficients of the matrix equation such that the data forms into a circular shape by the I and Q data. Thus, the same objective equation is used here and further modified to be:

$$[A(t)\cos\theta(t) - B_I]^2 + [A(t)\sin\theta(t) - B_Q]^2 = R^2, \tag{6.3}$$

where (B_I, B_Q) is the coordinate for the circle center shifted away from the coordinate zero by the coupling effect appeared in the system. After considering the equations from (6.1) and (6.2) as well as the settings of $a = 1, d = 0$, we can further reorganize the equation to:

$$\begin{aligned} B_{ENV}(t)^2 + 2(b - B_I)B_{ENV}(t) + bc^2 B_I B_{CP}^2(t) \\ - 2bcB_Q B_{CP}(t) - c^2 B_I B_{ENV}(t) B_{CP}^2(t) \\ - 2cB_Q B_{ENV}(t) B_{CP}(t) + const = 0, \end{aligned} \tag{6.4}$$

where the sine and cosine functions have been approximated using the first two terms of their Taylor expansions. To fulfill the approximation requirement, $B_{CP}(t)$ needs to be normalized before substituting into the equation. After performing the same matrix calculation steps discussed in Sec. III from [53], the coefficients can be determined using the baseband data $B_{ENV}(t)$ and $B_{CP}(t)$. After that, the second to the sixth coefficients are sufficient to solve for b and c, while *const* can be neglected.

6.3.2 Optimization Approach using Genetic Algorithm

Due to the limited SNR measured from the actual system, the aforementioned analytical method is not robust enough for identifying the coefficients to obtain an accurate displacement information. Therefore, an optimization method using the genetic algorithm (OPTA) is introduced to improve the tolerance to the noise level appearing in the system.

The algorithm is to find b and c values that minimize the total error created by (6.3) instead of directly solving the equation analytically. Therefore, a cost function is derived from (6.3) as follows,

$$C = \sum_{t=0}^{tend} \frac{\sqrt{[A(t)\cos\theta(t) - B_I]^2 + [A(t)\sin\theta(t) - B_Q]^2} - R}{R}. \tag{6.5}$$

To improve the optimization efficiency, the Levenberg-Marquardt (LM) center estimation algorithm is adopted to estimate B_I, B_Q and R during the cost function analysis. This reduces the unknown variables to only b and c. However, extreme cases can happen when the estimated R goes to infinity. Therefore, an infinite penalty is applied to the cost function if the estimated motion is smaller than $\lambda/4$. With the complete cost function defined, the generic algorithm is adopted to find the best-fitted b and c by minimizing the cost function output. Note that the OPTA method only requires a large motion amplitude for an improved accuracy without requiring to know the exact amplitude information for determining the coefficients.

A MATLAB simulation has been conducted to compare the robustness between these two algorithms with different levels of additive white Gaussian noise (AWGN) applied to $B_{ENV}(t)$ and $B_{CP}(t)$ signals. In this analysis, the signal-to-noise ratio (SNR) for the two signals are varied by applying the in-built MATLAB function.

To predict the performance of the algorithm during the actual experiment, a 0.34-λ peak-to-peak sine wave motion is used as the target motion. This contributes to a 68% circle if ideally displayed on an IQ plot. The sampling frequency of 100 Hz is used to simulate for a total time of 2 seconds where the motion frequency is selected to be 1 Hz. A coupling source is also modeled in the simulation where its amplitude is set to be 100 times bigger than that of the reflection signal and its phase offset is set to be 90^o relative to the phase of the reflection signal. With these information, we can first generate the ideal I and Q signal and then convert these results to $B_{ENV}(t)$ and $B_{CP}(t)$ by assuming $a = 10$, $b = -0.8$, $c = 5$ and $d = 10$ for all simulations. After applying AWGN to these two signals, the noisy waveform is then used as an input to test the two algorithm for obtaining the coefficients. In the end, the displacement demodulation is performed with using the predicted coefficients and the error is calculated with comparing between the demodulated motion amplitude and its ideal value. To find out the true relationship

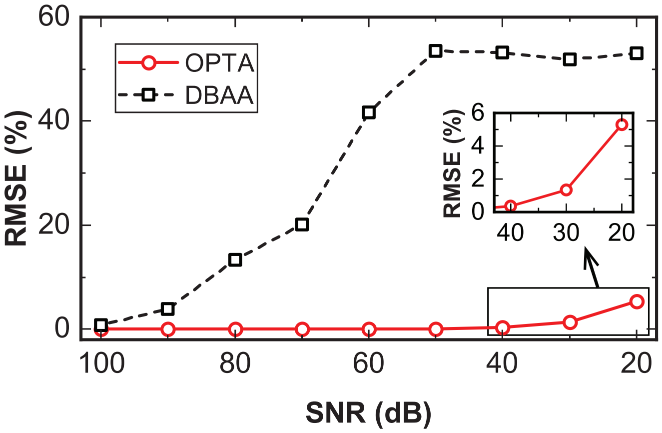

Figure 6.5: Percentage error in demodulated motion amplitude RMSE as a function of the SNR of the input baseband signals.

between the motion prediction accuracy and the SNR settings, each setting is simulated for 100 times with its root mean square error (RMSE) displayed in Fig. 6.5.

The results shown in Fig. 6.5 indicate that the DBAA method is very sensitive to the noise level appeared at the input waveform. The DBAA method results in an RMSE of more than 10% when the SNR level for the input is under 80 dB. In contrast, the OPTA method demonstrates an extremely robust performance against AWGN where the RMSE always remains under 6% even when the SNR is decreased down to 20 dB. This clearly shows the preference of adopting the OPTA method for processing the measurement results presented in the next section.

6.4 Displacement Sensing Using ENVSIL Radar

This section quantifies the displacement sensing performance of the ENVSIL radar prototype by measuring both a large and a small target motion produced by the LSTG. For both experiments, the LSTG is placed at 2.7 m away from the radar system.

6.4.1 Large Motion Linearity Test

During this measurement, the LSTG is first programmed to move in a large linear trajectory with $x_{max} = 5\,\mathrm{cm}$ to test the detection linearity of the radar. The LSTG is configured to move at a speed of 1 mm per second, which results in an output waveform shown in Fig. 6.6. The measurement results of $B_{CP}(t)$ and $B_{ENV}(t)$ clearly show the non-

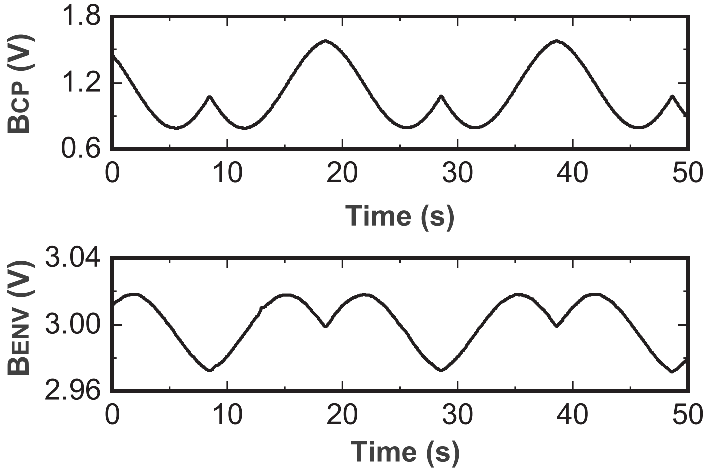

Figure 6.6: Measured time-domain waveform for charge pump output and envelope detection output in response to a 5-cm peak-to-peak motion displacement.

linearity effect that these output signals experience when detecting a large linear target motion. Again, this non-linearity is due to the coupling effect which converts a linear phase information into non-linear AM and PM inside the combined RF waveform.

Without first determining the proper coefficients for coordinate reconstruction, the data directly contributes to an IQ plot as shown in Fig. 6.7 (a). This is equivalent to have coefficient settings of $a = 1$, $b = 0$, $c = 1$ and $d = 0$. The figure displays a distorted waveform, which is not the circular shape expected from the target motion if correctly displayed in an IQ plot. After applying the OPTA method, the coefficients that best fit these data into a circular contour are determined, with $b = \text{-}2.362$ and $c = 0.093$. The updated IQ plot is shown in Fig. 6.7 (b) where the trajectory indeed forms a better circular contour.

After obtaining the coefficients from the OPTA method, its demodulated displacement result is shown in Fig. 6.8. The black curve represents the arctangent demodulated phase information after applying the circle fitting and the removal of the DC offset voltage based on the constructed IQ plot from Fig. 6.7 (b). The processed result identifies the peak-to-peak motion detected by the radar to be 50.6 mm which is 1.2% off from the actual setting. Besides that, a more specific phase error compared with the theoretical phase values throughout the time is plotted using the grey trace shown in Fig. 6.8. This reports a detected RMS phase error of 3.5^o which corresponds to 0.72 mm in displacement

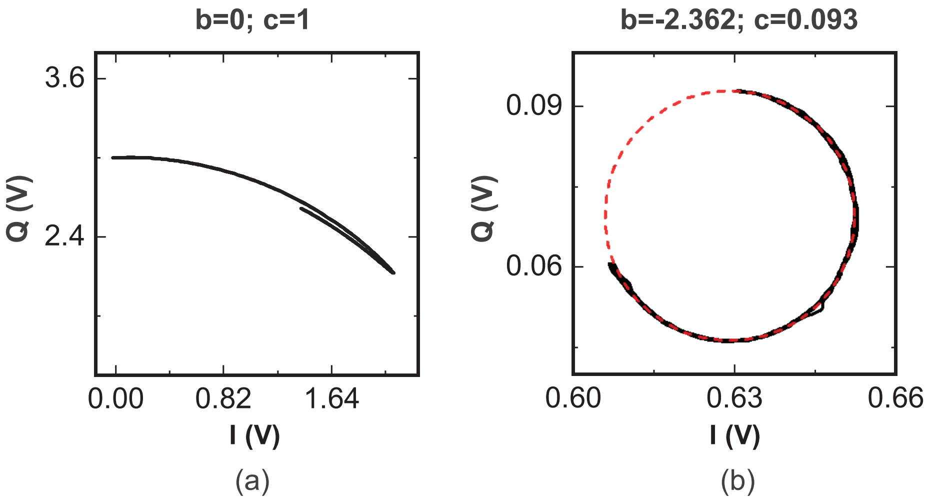

Figure 6.7: (a) Constructed IQ plot using the direct measurement results with $b = 0$ and $c = 1$. (b) Constructed IQ plot using coefficients identified by the OPTA method.

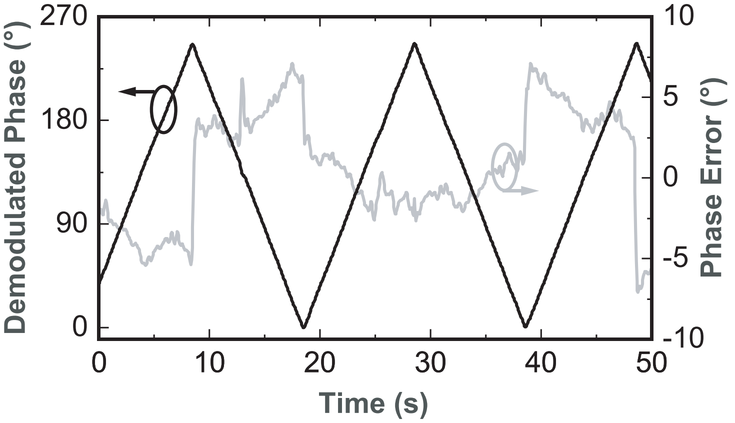

Figure 6.8: Demodulated phase from the target reflection signal and its phase error comparing with the theoretical values.

error, showing an excellent linearity when comparing with the detection result obtained by only the SIL system or the envelope detection reported in Fig. 6.6.

6.4.2 Small Motion Accuracy Test

In this experiment, the LSTG is programmed to move in a set of sinusoidal waveform with setting x_{max} to be 4 mm for testing the radar's detection accuracy with small-motion target displacement while being adjusted to different distance offsets. Each motion segment is designed to move in a frequency of 0.5 Hz for a total time of 30 s. Since the SNR for B_{ENV} and B_{CP} changes with respective to the phase offset of the target motion, 8 measurements

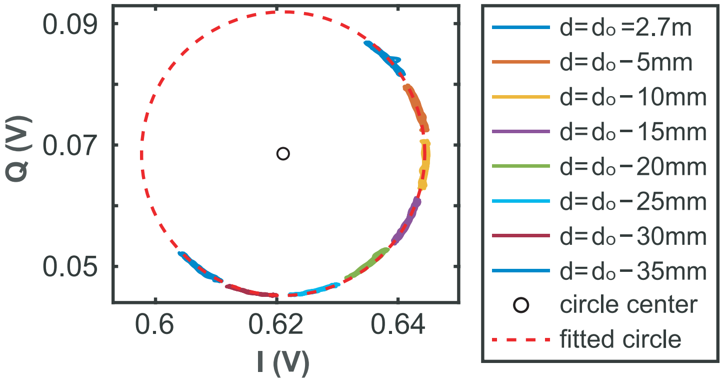

Figure 6.9: IQ plot for 8 motion segments with 4-mm sine wave motion separated by 5–mm spacing in-between.

have been performed with a 5-mm spacing in-between the consecutive motions to adjust the operating point of the detection system. The experiment is repeated four times to obtain an averaged detection error result. The same coefficients for b and c have been adopted in the signal processing, which leads to an IQ plot displayed in Fig. 6.9. In the figure, each motion segment represents a short arc with its phase offset changing respective to the distance offset between the target and the radar system. After adopting the radius correction method proposed in [68], the fitted circle is overlaid on top of the IQ plot. The circle center is also predicted and used for motion signal demodulation.

The processed detection results are displayed in Tab. 6.2 where it includes both the detected peak-to-peak motion amplitude result and the calculated percentage error when comparing to the ideal value. The measurement error ranges from 0.3 % to 5.9 % due to the random noise error as well as the distortion from the interference RF sources. These results are combined to yield an rms detection error of 2.92 % when detecting a 4-mm motion at a distance of 2.7 m.

6.5 Discussion

In literature, the radar-based displacement sensing systems are studied in many aspects including the circle-fitting algorithm development, analysis on the I/Q imbalance effect and the displacement sensitivity improvement. As this chapter aims to improve the radar sensitivity in displacement detection with consideration of the power level, we compare

Table 6.2: Short Displacement Measurement Results of LSTG with RC Technique

Measurement Number	d = 2.7 m	d = 2.7 m −5 mm	d = 2.7 m −10 mm	d = 2.7 m − 15 mm	d = 2.7 m −20 mm	d = 2.7 m −25 mm	d = 2.7 m −30 mm	d = 2.7 m −35 mm
#1	4.21	4.054	4.173	4.173	4.051	4.235	4.069	4.021
	(5.3%)	(1.3%)	(4.2%)	(4.3%)	(1.3%)	(5.9%)	(1.7%)	(0.5%)
#2	3.97	3.98	3.97	4.02	3.99	3.91	3.96	3.92
	(0.6%)	(0.6%)	(0.9%)	(0.5%)	(0.3%)	(2.1%)	(0.9%)	(2.1%)
#3	4.131	4.19	4.11	4.13	4.155	4.108	4.041	4.055
	(3.3%)	(4.8%)	(2.8%)	(3.3%)	(3.9%)	(2.7%)	(1.0%)	(1.4%)
#4	4.084	4.189	4.170	4.112	4.114	4.012	4.065	4.157
	(2.1%)	(4.7%)	(4.2%)	(2.8%)	(2.8%)	(0.3%)	(1.6%)	(3.9%)

*The nominal displacement is 4 mm and the measurement result is in unit of mm.

Table 6.3: Comparison of Radar-Based Displacement Monitoring Systems

Reference	**[68]**	**[12]**	**This work**
System Architecture	Conventional CW Radar	QSIL Radar	ENVSIL Radar
Key Demodulation Component	I/Q mixer	I/Q mixer+ RF switch + 22-ns delay line	PLL + Env. Detect.
Operating Frequency (f)	2.4 GHz	2.4 GHz	2.03 GHz
Transmitted Power (P_T)	+4 dBm[a]	+12 dBm	−2 dBm
Reflector RCS (σ_{eff})	0.028 m^2	0.18 m^2	0.29 m^2
Antenna Gain (G_{ANT})	8 dBi	12 dBi	12 dBi
Detection Distance (d)	1 m	1.5 m	2.7 m
Received Power (P_R)	−13.5 dBm	+3.5 dBm	−17.2 dBm
Target Displacement RMS Error (e_{rms})	1.8% @4-mm x_{max}	1.23% @2.5-mm x_{max}	2.92% @4-mm x_{max}
Maximum Power appeared in system (P_{MAX})	+10 dBm	+18 dBm	0 dBm
FOM1[b]	78.3	67.5	79.3
FOM2[c]	72.3	61.5	77.3

[a] The power splitter is assumed to have an insertion loss of 3 dB for power estimation.

[b] $\mathrm{FOM1} = -10\log_{10}\left[P_T \cdot \frac{G_{ANT}^2 \sigma_{eff} \lambda^2}{d^4}\right] - 20\log_{10}\left(\frac{e_{rms} \cdot x_{max}}{\lambda}\right)$

[c] $\mathrm{FOM2} = -10\log_{10}\left[P_{MAX} \cdot \frac{G_{ANT}^2 \sigma_{eff} \lambda^2}{d^4}\right] - 20\log_{10}\left(\frac{e_{rms} \cdot x_{max}}{\lambda}\right)$

our system measurement results with other state-of-the-art displacement sensing systems developed in [68] and [12]. Only these two systems align with our research interest and contain all the information required for comparison. The system parameters are acquired and listed in Tab. 6.3 where the results are compared quantitatively using the figure of merit introduced in this section that considers both the detection sensitivity and the system required power level.

There are many factors impacting the received power level (P_R) for the system in remote detection. The link budget calculation from [41] is referenced where P_R depends on the operating frequency wavelength (λ), the effective RCS of the reflector target (σ_{eff}), the antenna gain (G_{ANT}), the detection distance between the target and the radar system (d) and the transmitted power (P_T). Such relationship follows:

$$P_R = \frac{P_T G_{ANT}^2 \sigma_{eff} \lambda^2}{(4\pi)^3 d^4}. \tag{6.6}$$

These information from each system is listed in Tab. 6.3 where our work shows a lowest received power for the displacement sensing.

To fairly compare the system performance with all the parameters mentioned above, the figure of merit (FOM) is designed to consider both the power level required for the displacement sensing as well as the measurement accuracy achieved by the system. The FOM1 is defined to be linearly proportional to the product of the received power and the detection accuracy with its full expression shown in the footnote of Tab. 6.3. The FOM1 indicates that our work demonstrate an almost the same performance with the conventions CW radar while it excels by 11.8 dB when comparing with the QSIL radar. Furthermore, our system uses a simpler architecture compared with the QSIL radar that does not require any long delay line or switch for the demodulation.

One key feature that the proposed ENVSIL radar system possesses is its ability to demodulate the motion signal without using mixer. This greatly reduces the LO power requirement that the mixer relies on for proper operation. Therefore, our system can decrease the maximum power appeared in the system (P_{MAX}) by more than 10 dB as compared in Tab. 6.3. This feature helps the ENVSIL system to improve the power efficiency for the displacement sensing radar system. To demonstrate the power efficiency when comparing between systems, FOM2 has been designed that substitutes P_T in FOM1 with P_{MAX}. The full equation can be found in the footnote of Tab. 6.3. Based on this FOM2 metrics, our ENVSIL radar demonstrates the highest power efficiency in detecting the small target motion, with more than 5 dB higher than the other state-of-the-art systems.

6.6 Summary

A novel ENVSIL radar system without using the mixer component has been presented for remote displacement sensing. Due to the complementary relationship between the AM and PM, the ENVSIL system is designed to detect both the envelope and the phase information of the total received signal to recover the original phase information from the reflection signal.

The prototype system implemented by the cross-coupled VCO, a commercial PLL synthesizer and an envelope detector IC has been designed and proven to achieve a RMSE of $2.9\,\%$ with measuring a 4-mm peak-to-peak target motion at a distance of $2.7\,\mathrm{m}$. The system features with a low transmitted power of $-2\,\mathrm{dBm}$ and a high power efficiency with only $0\,\mathrm{dBm}$ required as the maximum power appeared in the system. Benefiting from the mixer-less architecture, the proposed ENVSIL system is considered to have the best power efficiency when comparing with other state-of-the-art systems.

Chapter 7

Conclusion and Future Work

7.1 Conclusion

In this dissertation, coupling effect in Doppler radar system was investigated using the IF system architecture. First, a compact Dual-PLL low-IF Doppler radar system using integrated PLL ICs with sharing the same input reference was developed. Based on the low-IF system architecture, a 6×6 MIMO Doppler radar was developed to improve the spatial resolution for the vital sign detection while maintaining its compactness without using any RF instrumentation. The multi-subject experimental results reported a spatial resolution of 0.6 m with a distance of 1.9 meter between the measured subjects and the system. Both the heart rate and respiration rate for two subjects has been successfully detected by the MIMO radar simultaneously.

After developing the compact IF Doppler radar system, a detailed analysis has been conducted to identify the coupling effect to the detection SNR inside the system. The controlled experiments using LSTG demonstrated a linear relationship between the excessive coupling strength and the increased noise floor level. Followed by that, the automatic RF cancellation has been implemented to successfully enhance the detection SNR under scenarios with high-coupling strength, such as through-wall vital sign detection and low antenna isolation. Multiple experiments have been performed to demonstrate the effectiveness of the automatic coupling cancellation technique in SNR improvement. The results showed an SNR improvement of more than 15 dB with a processing time under 2 seconds.

Finally, the coupling effect to the alteration of the modulation scheme involved in the Doppler radar system has been investigated. The phase modulation was verified to be able to transform into amplitude modulation with coupling effect involved. The PM and AM were tested to be complementary to each other and this relationship was used to develop the novel ENVSIL system where the system detects both the amplitude and phase variation inside the system. Such complementary output signals were then used for remote displacement sensing featuring the low-power design. Benefiting from the mixer-less system architecture, the maximum power level required by the ENVSIL system is only 0 dBm. This helps the system to achieve the best power efficiency and detection sensitivity when comparing with other state-of-the-art displacement sensing systems. This coupling effect theory also assists to improve our understanding on the relationship among the conventional IQ system, the SIL system and the envelope detection system. The two quadrature output signals from the IQ system responds to any variation in the horizontal and vertical direction at the IQ plot whereas the SIL system and the envelope detection system detects any variation in the angular and radial direction at the IQ plot respectively.

7.2 Future Work

For the future work, there are five main topics that are recommended for further exploration:

- Since the coupling cancellation is an effective technique for reducing the noise level, the mathematical model for noise reduction with consideration of the time delay difference between the received signal and the cancellation path waveform needs to be derived. A higher cancellation depth by possibly multiple cancellation techniques can be attempted to find out the limit on SNR improvement due to the coupling cancellation.
- Due to multiple challenges discussed in the previous section about designing an ENVSIL system, a more systematic design procedure should be further explored.

- Due to the amplitude modulation created by the coupling effect, the envelope detector could serve as a low-cost and low-power alternative to the conventional mixer for the motion demodulator. However, the major issue with adopting an envelope detector is its higher baseband noise and its limited linearity compared with the conventional mixer. The higher noise is due to the inherent high bandwidth. Therefore, further research efforts need to be made for better performance in the noise and linearity aspects of the envelope detector.

- Passive sensor has emerged as an attractive research field where the system does not require a dedicated transmitter. Instead, the sensor only consists of a receiver path which only picks up the coupling and the target reflection signal to demodulate the motion information. The coupling effect analyzed in this dissertation could serve as foundations and intuition to further development of a power-efficient and a low-cost passive vital-sign detector.

REFERENCES

[1] L. M. Haddad, P. Annamaraju, and T. J. Toney-Butler, “Nursing shortage,” StatPearls, Treasure Island, FL. Accessed on : May 10, 2022. [Online]. Available: https://www.ncbi.nlm.nih.gov/books/NBK493175/

[2] S. L. Murphy, K. D. Kochanek, J. Xu, and E. Arias, “Mortality in the united states, 2020,” Hyattsville, MD, 22 12, journal Issue. [Online]. Available: https://stacks.cdc.gov/view/cdc/112079

[3] S. S. Virani et al., “Heart disease and stroke statistics—2020 update: A report from the american heart association,” *Circulation*, vol. 141, no. 9, Mar. 2020.

[4] R. S. Velagaleti and R. S. Vasan, “c,” *Cardiology clinics*, vol. 25, no. 4, pp. 487–v, Nov 2007, 18063154[pmid]. [Online]. Available: https://pubmed.ncbi.nlm.nih.gov/18063154

[5] M. Kilgore, H. K. Patel, A. Kielhorn, J. F. Maya, and P. Sharma, “Economic burden of hospitalizations of medicare beneficiaries with heart failure,” *Risk management and healthcare policy*, vol. 10, pp. 63–70, May 2017. [Online]. Available: https://pubmed.ncbi.nlm.nih.gov/28546776

[6] N. J. Conn, K. Q. Schwarz, and D. A. Borkholder, “In-home cardiovascular monitoring system for heart failure: Comparative study,” *JMIR mHealth and uHealth*, vol. 7, no. 1, pp. e12 419–e12 419, Jan. 2019.

[7] G. Wang, C. Gu, T. Inoue, and C. Li, “A hybrid fmcw-interferometry radar for indoor precise positioning and versatile life activity monitoring,” *IEEE Transactions on Microwave Theory and Techniques*, vol. 62, no. 11, pp. 2812–2822, 2014.

[8] J. C. Lin, “Microwave sensing of physiological movement and volume change: a review,” *Bioelectromagnetics*, vol. 13, no. 6, pp. 557–565, 1992.

[9] F. Wang, C. Li, C. Hsiao, T. Horng, J. Lin, K. Peng, J. Jau, J. Li, and C. Chen, “A novel vital-sign sensor based on a self-injection-locked oscillator,” *IEEE Transactions on Microwave Theory and Techniques*, vol. 58, no. 12, pp. 4112–4120, 2010.

[10] P. Wu, J. Jau, C. Li, T. Horng, and P. Hsu, “Phase- and self-injection-locked radar for detecting vital signs with efficient elimination of dc offsets and null points,” *IEEE Transactions on Microwave Theory and Techniques*, vol. 61, no. 1, pp. 685–695, 2013.

[11] P. H. Juan, K. H. Chen, and F. K. Wang, “Frequency-offset self-injection-locked radar with digital frequency demodulation for snr improvement, elimination of emi issue, and dc offset calibration,” *IEEE Transactions on Microwave Theory and Techniques*, vol. 69, no. 1, pp. 1149–1160, 2021.

[12] F.-K. Wang, P.-H. Juan, S.-C. Su, M.-C. Tang, and T.-S. Horng, "Monitoring displacement by a quadrature self-injection-locked radar with measurement- and differential-based offset calibration methods," *IEEE Sensors Journal*, vol. 19, no. 5, pp. 1905–1916, 2019.

[13] G. Vinci, S. Lindner, F. Barbon, S. Mann, M. Hofmann, A. Duda, R. Weigel, and A. Koelpin, "Six-port radar sensor for remote respiration rate and heartbeat vital-sign monitoring," *IEEE Transactions on Microwave Theory and Techniques*, vol. 61, no. 5, pp. 2093–2100, 2013.

[14] C. Li, Y. Xiao, and J. Lin, "Experiment and spectral analysis of a low-power ka-band heartbeat detector measuring from four sides of a human body," *IEEE Transactions on Microwave Theory and Techniques*, vol. 54, no. 12, pp. 4464–4471, 2006.

[15] Y. Xiao, C. Li, and J. Lin, "A portable noncontact heartbeat and respiration monitoring system using 5-ghz radar," *IEEE Sensors Journal*, vol. 7, no. 7, pp. 1042–1043, 2007.

[16] C. Li, Y. Xiao, and J. Lin, "A 5ghz double-sideband radar sensor chip in 0.18 μm cmos for non-contact vital sign detection," *IEEE Microwave and Wireless Components Letters*, vol. 18, no. 7, pp. 494–496, 2008.

[17] X. Ma, L. Li, S. Ming, X. You, and J. Lin, "Envelope detection for an adc-relaxed double-sideband low-if cw doppler radar," *IEEE Transactions on Microwave Theory and Techniques*, vol. 66, no. 12, pp. 5833–5841, 2018.

[18] A. D. Droitcour, O. Boric-Lubecke, V. M. Lubecke, J. Lin, and G. T. A. Kovacs, "Range correlation and i/q performance benefits in single-chip silicon doppler radars for noncontact cardiopulmonary monitoring," *IEEE Transactions on Microwave Theory and Techniques*, vol. 52, no. 3, pp. 838–848, 2004.

[19] T. Chin, K. Lin, S. Chang, and C. Chang, "A fast clutter cancellation method in quadrature doppler radar for noncontact vital signal detection," in *2010 IEEE MTT-S International Microwave Symposium*, 2010, pp. 764–767.

[20] C. Gu, Z. Peng, and C. Li, "High-precision motion detection using low-complexity doppler radar with digital post-distortion technique," *IEEE Transactions on Microwave Theory and Techniques*, vol. 64, no. 3, pp. 961–971, 2016.

[21] C. Gu, C. Li, J. Lin, J. Long, J. Huangfu, and L. Ran, "Instrument-based noncontact doppler radar vital sign detection system using heterodyne digital quadrature demodulation architecture," *IEEE Transactions on Instrumentation and Measurement*, vol. 59, no. 6, pp. 1580–1588, 2010.

[22] I. Mostafanezhad and O. Boric-Lubecke, "Benefits of coherent low-if for vital signs monitoring using doppler radar," *IEEE Transactions on Microwave Theory and Techniques*, vol. 62, no. 10, pp. 2481–2487, 2014.

[23] H. Zhao, H. Hong, L. Sun, Y. Li, C. Li, and X. Zhu, "Noncontact physiological dynamics detection using low-power digital-if doppler radar," *IEEE Transactions on Instrumentation and Measurement*, vol. 66, no. 7, pp. 1780–1788, 2017.

[24] X. Jiang, X. Gao, H. Zhao, H. Hong, and X. Liu, "A compact digital low-if dual-pll doppler radar for remote vital sign detection," in *2021 IEEE 21st Annual Wireless and Microwave Technology Conference (WAMICON)*, 2021, pp. 1–4.

[25] K.-M. Chen, D. Misra, H. Wang, H.-R. Chuang, and E. Postow, "An x-band microwave life-detection system," *IEEE Transactions on Biomedical Engineering*, vol. BME-33, no. 7, pp. 697–701, 1986.

[26] H.-R. Chuang, Y. Chen, and K.-M. Chen, "Automatic clutter-canceler for microwave life-detection systems," *IEEE Transactions on Instrumentation and Measurement*, vol. 40, no. 4, pp. 747–750, 1991.

[27] J. Lin, "Noncontact measurement of cardiopulmonary movements: A review of system architectures and the path to micro-radars," in *2013 IEEE MTT-S International Microwave Workshop Series on RF and Wireless Technologies for Biomedical and Healthcare Applications (IMWS-BIO)*, 2013, pp. 1–3.

[28] A. D. Droitcour, O. Boric-Lubecke, and G. T. A. Kovacs, "Signal-to-noise ratio in doppler radar system for heart and respiratory rate measurements," *IEEE Transactions on Microwave Theory and Techniques*, vol. 57, no. 10, pp. 2498–2507, 2009.

[29] S.-S. Myoung, J.-H. Park, J. Yook, and B.-J. Jang, "2.4 ghz bio-radar system with improved performance by using phase-locked loop," *Microwave and Optical Technology Letters*, vol. 52, 2010.

[30] S. Bakhtiari, T. W. Elmer, N. M. Cox, N. Gopalsami, A. C. Raptis, S. Liao, I. Mikhelson, and A. V. Sahakian, "Compact millimeter-wave sensor for remote monitoring of vital signs," *IEEE Transactions on Instrumentation and Measurement*, vol. 61, no. 3, pp. 830–841, 2012.

[31] C.-C. Chou, W.-C. Lai, Y.-K. Hsiao, and H.-R. Chuang, "60-ghz cmos doppler radar sensor with integrated v-band power detector for clutter monitoring and automatic clutter-cancellation in noncontact vital-signs sensing," *IEEE Transactions on Microwave Theory and Techniques*, vol. 66, no. 3, pp. 1635–1643, 2018.

[32] B. Park, O. Boric-Lubecke, and V. M. Lubecke, "Arctangent demodulation with dc offset compensation in quadrature doppler radar receiver systems," *IEEE Transactions on Microwave Theory and Techniques*, vol. 55, no. 5, pp. 1073–1079, May 2007.

[33] X. Gao, J. Xu, A. Rahman, V. Lubecke, and O. Boric-Lubecke, "Arc shifting method for small displacement measurement with quadrature cw doppler radar," in *2017 IEEE MTT-S International Microwave Symposium (IMS)*, June 2017, pp. 1003–1006.

[34] C. Li and J. Lin, “Complex signal demodulation and random body movement cancellation techniques for non-contact vital sign detection,” in *2008 IEEE MTT-S International Microwave Symposium Digest*, 2008, pp. 567–570.

[35] Y. Xiao, J. Lin, O. Boric-Lubecke, and V. Lubecke, “A ka-band low power doppler radar system for remote detection of cardiopulmonary motion,” in *2005 IEEE Engineering in Medicine and Biology 27th Annual Conference*, 2005, pp. 7151–7154.

[36] X. Ma, Y. Wang, L. Lu, X. Zhang, Q. Chen, X. You, J. Lin, and L. Li, “Design of a 100-ghz double-sideband low-if cw doppler radar transceiver for micrometer mechanical vibration and vital sign detection,” *IEEE Transactions on Microwave Theory and Techniques*, vol. 68, no. 7, pp. 2876–2890, 2020.

[37] Shuhei Yamada, O. Boric-Lubecke, and V. M. Lubecke, “Cancellation techniques for lo leakage and dc offset in direct conversion systems,” in *2008 IEEE MTT-S International Microwave Symposium Digest*, 2008, pp. 1191–1194.

[38] A. D. Droitcour, O. Boric-Lubecke, and S. Yamada, *Sources of Noise and Signal-to-Noise Ratio.* John Wiley Sons, Ltd, 2016, ch. 6, pp. 137–170. [Online]. Available: https://onlinelibrary.wiley.com/doi/abs/10.1002/9781119078418.ch6

[39] C.-H. Tseng, L.-T. Yu, J.-K. Huang, and C.-L. Chang, “A wearable self-injection-locked sensor with active integrated antenna and differentiator-based envelope detector for vital-sign detection from chest wall and wrist,” *IEEE Transactions on Microwave Theory and Techniques*, vol. 66, no. 5, pp. 2511–2521, 2018.

[40] G. Engen, “The six-port reflectometer: An alternative network analyzer,” *IEEE Transactions on Microwave Theory and Techniques*, vol. 25, no. 12, pp. 1075–1080, 1977.

[41] J. E. Kiriazi, O. Boric-Lubecke, and V. M. Lubecke, “Radar cross section of human cardiopulmonary activity for recumbent subject,” in *2009 Annual International Conference of the IEEE Engineering in Medicine and Biology Society*, 2009, pp. 4808–4811.

[42] E. Piuzzi, P. D’Atanasio, S. Pisa, E. Pittella, and A. Zambotti, “Complex radar cross section measurements of the human body for breath-activity monitoring applications,” *IEEE Transactions on Instrumentation and Measurement*, vol. 64, no. 8, pp. 2247–2258, 2015.

[43] S.-S. Myoung, J.-H. Park, J.-G. Yook, and B.-J. Jang, “2.4 ghz bio-radar system with improved performance by using phase-locked loop,” *Microwave and Optical Technology Letters*, vol. 52, no. 9, pp. 2074–2076, 2010. [Online]. Available: https://onlinelibrary.wiley.com/doi/abs/10.1002/mop.25366

[44] S. Bakhtiari, T. W. Elmer, N. M. Cox, N. Gopalsami, A. C. Raptis, S. Liao, I. Mikhelson, and A. V. Sahakian, “Compact millimeter-wave sensor for remote monitoring of

vital signs," *IEEE Transactions on Instrumentation and Measurement*, vol. 61, no. 3, pp. 830–841, 2012.

[45] K.-C. Peng, M.-C. Sung, F.-K. Wang, and T.-S. Horng, "Noncontact vital sign sensing under nonperiodic body movement using a novel frequency-locked-loop radar," *IEEE Transactions on Microwave Theory and Techniques*, vol. 69, no. 11, pp. 4762–4773, 2021.

[46] C. Li and J. Lin, "Optimal carrier frequency of non-contact vital sign detectors," in *2007 IEEE Radio and Wireless Symposium*, 2007, pp. 281–284.

[47] T. Sakamoto and T. Koda, "Respiratory motion imaging using 2.4-ghz nine-element-array continuous-wave radar," *IEEE Microwave and Wireless Components Letters*, vol. 30, no. 7, pp. 717–720, 2020.

[48] C. Hsu, C. Chuang, F. Wang, T. Horng, and L. Hwang, "Detection of vital signs for multiple subjects by using self-injection-locked radar and mutually injection-locked beam scanning array," in *2017 IEEE MTT-S International Microwave Symposium (IMS)*, 2017, pp. 991–994.

[49] M. Nosrati, S. Shahsavari, S. Lee, H. Wang, and N. Tavassolian, "A concurrent dual-beam phased-array doppler radar using mimo beamforming techniques for short-range vital-signs monitoring," *IEEE Transactions on Antennas and Propagation*, vol. 67, no. 4, pp. 2390–2404, 2019.

[50] A. Ahmad, J. C. Roh, D. Wang, and A. Dubey, "Vital signs monitoring of multiple people using a fmcw millimeter-wave sensor," in *2018 IEEE Radar Conference (RadarConf18)*, 2018, pp. 1450–1455.

[51] M. Zakrzewski, H. Raittinen, and J. Vanhala, "Comparison of center estimation algorithms for heart and respiration monitoring with microwave doppler radar," *IEEE Sensors Journal*, vol. 12, no. 3, pp. 627–634, 2012.

[52] S. Guan, J. A. Rice, C. Li, and C. Gu, "Automated dc offset calibration strategy for structural health monitoring based on portable cw radar sensor," *IEEE Transactions on Instrumentation and Measurement*, vol. 63, no. 12, pp. 3111–3118, 2014.

[53] M. Zakrzewski, A. Singh, E. Yavari, X. Gao, O. Boric-Lubecke, J. Vanhala, and K. Palovuori, "Quadrature imbalance compensation with ellipse-fitting methods for microwave radar physiological sensing," *IEEE Transactions on Microwave Theory and Techniques*, vol. 62, no. 6, pp. 1400–1408, 2014.

[54] X. Gao, J. Xu, A. Rahman, V. Lubecke, and O. Boric-Lubecke, "Arc shifting method for small displacement measurement with quadrature cw doppler radar," in *2017 IEEE MTT-S International Microwave Symposium (IMS)*, 2017, pp. 1003–1006.

[55] K. Iizuka, A. Freundorfer, and T. Iwasaki, “A method of surface clutter cancellation for an underground cw radar,” *IEEE Transactions on Electromagnetic Compatibility*, vol. 31, no. 3, pp. 330–332, 1989.

[56] H.-R. Chuang, Y. Chen, and K.-M. Chen, “Automatic clutter-canceler for microwave life-detection systems,” *IEEE Transactions on Instrumentation and Measurement*, vol. 40, no. 4, pp. 747–750, 1991.

[57] K.-M. Chen, Y. Huang, J. Zhang, and A. Norman, “Microwave life-detection systems for searching human subjects under earthquake rubble or behind barrier,” *IEEE Transactions on Biomedical Engineering*, vol. 47, no. 1, pp. 105–114, 2000.

[58] C. Gu, R. Li, H. Zhang, A. Y. C. Fung, C. Torres, S. B. Jiang, and C. Li, “Accurate respiration measurement using dc-coupled continuous-wave radar sensor for motion-adaptive cancer radiotherapy,” *IEEE Transactions on Biomedical Engineering*, vol. 59, no. 11, pp. 3117–3123, 2012.

[59] H.-C. Kuo, C.-C. Lin, C.-H. Yu, P.-H. Lo, J.-Y. Lyu, C.-C. Chou, and H.-R. Chuang, “A fully integrated 60-ghz cmos direct-conversion doppler radar rf sensor with clutter canceller for single-antenna noncontact human vital-signs detection,” *IEEE Transactions on Microwave Theory and Techniques*, vol. 64, no. 4, pp. 1018–1028, 2016.

[60] C.-C. Chou, W.-C. Lai, Y.-K. Hsiao, and H.-R. Chuang, “60-ghz cmos doppler radar sensor with integrated v-band power detector for clutter monitoring and automatic clutter-cancellation in noncontact vital-signs sensing,” *IEEE Transactions on Microwave Theory and Techniques*, vol. 66, no. 3, pp. 1635–1643, 2018.

[61] S. Bi, X. Jiang, X. Gao, and X. Liu, “Coupling-cancellation-antenna for improving doppler radar motion measurement accuracy,” in *2019 IEEE 20th Wireless and Microwave Technology Conference (WAMICON)*, 2019, pp. 1–4.

[62] M. I. Skolnik, Ed., *Radar Handbook*, 2nd ed. New York: McGraw-Hill Education, 1990, pp. 2.4.

[63] C. Wei and J. Lin, “Digitally assisted low if architecture for noncontact vital sign detection,” in *2015 IEEE MTT-S International Microwave Symposium*, 2015, pp. 1–4.

[64] I. Beavers, “Noise spectral density: A new adc metric?” Analog Devices, Norwood, MA. Accessed on : Mar. 21, 2022. [Online]. Available: https://www.analog.com/en/technical-articles/noise-spectral-density.html

[65] D. Banerjee, *PLL Performance, Simulation, and Design, 5th ed.* New York, NY, USA: Dog Ear Publishing, LLC, May 2017.

[66] C. Li, V. M. Lubecke, O. Boric-Lubecke, and J. Lin, “A review on recent advances in doppler radar sensors for noncontact healthcare monitoring,” *IEEE Transactions on Microwave Theory and Techniques*, vol. 61, no. 5, pp. 2046–2060, 2013.

[67] K.-C. Peng, M.-C. Sung, F.-K. Wang, and T.-S. Horng, “Non-contact vital sign detection using gain detection technique,” in *2021 IEEE International Symposium on Radio-Frequency Integration Technology (RFIT)*, 2021, pp. 1–2.

[68] X. Gao and O. Boric-Lubecke, “Radius correction technique for doppler radar non-contact periodic displacement measurement,” *IEEE Transactions on Microwave Theory and Techniques*, vol. 65, no. 2, pp. 621–631, 2017.

[69] M. Budge and M. Burt, “Range correlation effects in radars,” in *The Record of the 1993 IEEE National Radar Conference*, 1993, pp. 212–216.